ชั้นยึดหยุ่นไร้ขอบเขตภายใต้แรงกระทำสมมาตรรอบแกนและอิทธิพลของหน่วยแรงที่ผิว

นางสาวพอจันทร์ ตุฏฐิพงษ์สวัสดิ์

วิทยานิพนธ์นี้เป็นส่วนหนึ่งของการศึกษาตามหลักสูตรปริญญาวิศวกรรมศาสตรมหาบัณฑิต
สาขาวิชาวิศวกรรมโยธา ภาควิชาวิศวกรรมโยธา
คณะวิศวกรรมศาสตร์ จุฬาลงกรณ์มหาวิทยาลัย
ปีการศึกษา 2555

INFINITE ELASTIC LAYER UNDER AXISYMMETRIC SURFACE LOADS AND INFLUENCE OF SURFACE STRESSES

Miss Porjan Tuttipongsawat

A Thesis Submitted in Partial Fulfillment of the Requirements
for the Degree of Master of Engineering Program in Civil Engineering
Department of Civil Engineering
Faculty of Engineering
Chulalongkorn University
Academic Year 2012

Thesis Title	INFINITE ELASTIC LAYER UNDER AXISYMMETRIC SURFACE LOADS AND INFLUENCE OF SURFACE STRESSES
By	Miss Porjan Tuttipongsawat
Field of Study	Civil Engineering
Thesis Advisor	Assistant Professor Jaroon Rungamornrat, Ph.D.
Thesis Co-advisor	Professor Teerapong Senjuntichai, Ph.D.

Accepted by the Faculty of Engineering, Chulalongkorn University in Partial Fulfillment of the Requirements for the Master's Degree

…… Dean of the Faculty of Engineering

(Associate Professor Boonsom Lerdhirunwong, Dr.Ing.)

THESIS COMMITTEE

……. Chairman

(Assistant Professor Watanachai Smittakorn, Ph.D.)

……. Thesis Advisor

(Assistant Professor Jaroon Rungamornrat, Ph.D.)

……. Thesis Co-advisor

(Professor Teerapong Senjuntichai, Ph.D.)

……. External Examiner

(Punchet Thammarak, Ph.D.)

พอจันทร์ ตุฏฐิพงษ์สวัสดิ์ : ชั้นยืดหยุ่นไร้ขอบเขตภายใต้แรงกระทำสมมาตรรอบแกนและอิทธิพลของหน่วยแรงที่ผิว. (INFINITE ELASTIC LAYER UNDER AXISYMMETRIC SURFACE LOADS AND INFLUENCE OF SURFACE STRESSES) อ. ที่ปรึกษาวิทยานิพนธ์หลัก: ผศ.ดร. จรูญ รุ่งอมรรัตน์, อ. ที่ปรึกษาวิทยานิพนธ์ร่วม: ศ.ดร. ธีรพงศ์ เสนจันทร์ฒิไชย, 75 หน้า.

วิทยานิพนธ์ฉบับนี้นำเสนอผลเฉลยสมบูรณ์ของชั้นยืดหยุ่นพื้นแข็งไร้ขอบเขตภายใต้แรงกระทำสมมาตรรอบแกนโดยพิจารณาหน่วยแรงที่ผิว ปัญหาค่าขอบเขตที่สอดคล้องถูกสร้างขึ้นโดยอาศัยทฤษฎีทั่วไปของความยืดหยุ่นเชิงเส้นสำหรับชั้นวัสดุและสมการของเกอร์ตินและเมอร์ดอครูปแบบสมบูรณ์ในการจำลองพฤติกรรมของหน่วยแรงที่ผิว หลักการตัวแทนความเครียดศักดิ์ของเลิฟและการแปลงแฮนเคลถูกนำมาใช้เพื่อให้ได้ผลเฉลยของการเคลื่อนที่และหน่วยแรงในรูปปริพันธ์ซึ่งสามารถหาค่าได้จากการเลือกให้ระเบียบวิธีเชิงตัวเลขที่เหมาะสม จากการศึกษาอิทธิพลของหน่วยแรงที่ผิวและพฤติกรรมที่ขึ้นอยู่กับขนาดพบว่า หน่วยแรงที่ผิวมีอิทธิพลมากในบริเวณใกล้ผิวและเมื่อขนาดปัญหาใกล้เคียงกับความยาวอินทรินซิค อิทธิพลดังกล่าวเห็นได้ชัดเจนยิ่งขึ้นเมื่อนำผลของแรงตึงผิวคงค้างมาร่วมพิจารณาด้วย นอกจากนี้ได้มีการสร้างผลเฉลยพื้นฐานด้วยการเปลี่ยนแรงกระทำที่ผิวเป็นแรงกระทำตั้งฉากแบบจุดขนาดหนึ่งหน่วย แรงกระทำตั้งฉากแบบวงแหวนขนาดหนึ่งหน่วย และแรงกระทำสัมผัสขนาดหนึ่งหน่วย ผลเฉลยดังกล่าวเป็นพื้นฐานสำคัญในการพัฒนาสมการค่าขอบเขตของปัญหาอื่นๆที่เกี่ยวข้อง เช่น ปัญหาการกดในระดับนาโน

ภาควิชา .....วิศวกรรมโยธา..... ลายมือชื่อนิสิต .....

สาขาวิชา .....วิศวกรรมโยธา..... ลายมือชื่อ อ.ที่ปรึกษาวิทยานิพนธ์หลัก .....

ปีการศึกษา .....2555..... ลายมือชื่อ อ.ที่ปรึกษาวิทยานิพนธ์ร่วม .....

5470298021 : MAJOR CIVIL ENGINEERING
KEYWORDS : SURFACE FREE ENERGY / GURTIN-MURDOCH MODEL / HANKEL INTEGRAL TRANSFORM / NANOSCALE INFLUENCE / FINITE THICKNESS LAYER

PORJAN TUTTIPONGSAWAT: INFINITE ELASTIC LAYER UNDER AXISYMMETRIC SURFACE LOADS AND INFLUENCE OF SURFACE STRESSES. ADVISOR: ASST. PROF. JAROON RUNGAMORNRAT, Ph.D., CO-ADVISOR: PROF. TEERAPONG SENJUNTICHAI, Ph.D., 75 pp.

This thesis presents a complete solution of an infinite, rigid based elastic layer under the action of axisymmetric surface loads by taking the surface energy effects into account. The corresponding boundary value problem is formulated based on a classical theory of linear elasticity for the bulk layer and a complete Gurtin-Murdoch constitutive relation for modeling the surface energy effects. In the solution procedure, an analytical technique based on Love's representation and Hankel integral transform is adopted to derive an explicit integral-form solution for both the displacement and stress fields. A selected numerical quadrature is subsequently applied to efficiently evaluate all involved integrals. To demonstrate the influence of surface free energy and size-dependency, an extensive parametric study is carried out. The surface energy effects show strong influence on responses at the region closed to the surface and also when a length scale of the problem is comparable to the intrinsic length of the surface. Such influences are more evident when the contribution of the residual surface tension is taken into account. Moreover, three fundamental solutions are constructed by specializing the axisymmetric surface loads to a unit normal concentrated load, a unit normal ring load and a unit tangential ring load. Such basic results constitute the essential basis for the development of boundary integral equations governing other related problems, e.g., nano-indentations.

Department: ……Civil Engineering…… Student 's Signature ……..
Field of Study: …Civil Engineering…… Advisor 's Signature ……..……...
Academic Year: ……2012……..... Co-advisor 's Signature …….……...

ACKNOWLEDGEMENTS

It is a great pleasure to thank everyone who advised and supported me to conduct my thesis successfully. First, I would like to express my greatest gratitude to my thesis advisor, Assistant Professor Dr. Jaroon Rungamornrat, and my thesis co-advisor, Professor Dr. Teerapong Senjuntichai, who gave me valuable guidance, continuous support, encouragement, and patience. Without them, it would have been impossible for me to complete this thesis. I would like to show my gratitude to my thesis committees for their invaluable comments and suggestions. Also, I would like to express my sincere thanks to all instructors who gave me valuable knowledge and the Department of Civil Engineering, Faculty of Engineering, Chulalongkorn University, who gave me the support and opportunity to study. Moreover, I wish to thank my friend, Miss Yutiwadee Pinyochotiwong, for her kind assistance and for sharing experiences. Moreover, special thanks of mine go to everyone who helped me both directly and indirectly. Last but not least, I would like to express my heartfelt gratitude to my parent for their continuous encouragement and their great care.

CONTENTS

Pages

LIST OF TABLES

LIST OF FIGURES

CHAPTER I

INTRODUCTION

1.1 GENERAL

Nowadays, nanotechnology plays an important role in various disciplines including biology, chemistry, physics, medicines and engineering (Booker and Boysen, 2005). For instance, nano-crystals are employed in household lightings to convert electricity into light instead of wasting away into heat. A newly invented device called nano-shell is used in the medical applications to destroy a tumor after activated by a laser beam without any harm to contiguous cells. Nano-crystalline silicon carbide is found in the hard protective coatings for cutting tools and computer hard disks. According to those various applications in nanotechnology, advanced researches on material properties of nano-scale or nano-structured materials are essential in order to profoundly understand their behaviors.

Investigation of nano-mechanical properties can be achieved by either conducting experiments or performing mathematical simulations. Several experimental researches have been found in the literature; for instance, Wong et al. (1997) utilized an atomic-force microscopy to determine the mechanical properties of isolated silicon carbide (SiC) nano-rods (NRs) and multi-wall carbon nano-tubes (MWNTs), Mao et al. (2003) employed the atomic-force microscope to investigate the hardness of both ZnO and SnO_2 nano-belts, and Poncharal et al. (1999) statically and dynamically measured the bending modulus of carbon nano-tubes in a transmission electron microscope. It is generally acknowledged that experimental methods yield results reflecting real behavior. However, it is still found highly dependent on experimental environments and, more importantly, expensive due to the requirement of sophisticated equipments and high-precision testing procedures. As a result, the latter approach using mathematical simulations has become an attractive alternative and been widely used to develop fundamental understanding and further predict complex phenomena. In addition, once integrating essential features and properly calibrated with data from basic experiments, mathematical models are found

capable of simulating responses under various conditions. Within the context of modeling nano-scale influence of solids, two predominant mathematical models, one known as the molecular or atomistic models and the other corresponding to the modified or enhanced continuum-based models, have been commonly employed in the literature. The molecular-based models, while providing more precise response prediction, are highly complex and generally consume tremendous computational resources because billions of atom at a nano-scale need to be modeled whereas the continuum-based models are less complicated and much more computationally efficient.

Resulting from atomistic simulations, it was discovered that behaviors of atoms near the surface differ from those of the bulk. Hence, the solid cannot be treated as a homogeneous body but needs to be divided into two parts, i.e. the bulk and the surface. To utilize a continuum-based model instead of the molecular model, it must be modified properly by incorporating the influence of the surface free energy. There have been various studies carried out by using modified continuum-based techniques; for instance, He et al. (2004) studied the size-dependent mechanical responses of ultra-thin elastic films of nano-scale thickness and Wang et al. (2010) used a finite element method together with the Gurtin-Murdoch surface elasticity model to analyze the size-dependent deformation of two-dimensional nano-sized structures with surface effects. All of those researches verified that mathematical models properly enhanced to account for the surface energy effects and size-dependency were able to simulate nano-scale influence and correctly predict responses of soft solids.

Due to the rapid growth of interests and applications of nano-technology, the investigation of mechanical behaviors and responses at a nano-scale level has gained significant attention from many researchers and various sophisticated models have been proposed to study those phenomena. Problems of surface loadings and contacts are considered fundamental in nano-mechanics and have a wide range of applications including the investigation of mechanical properties such as hardness and elastic modulus. Work towards the modeling of near-surface fields under different surface loading conditions by using modified continuum-based models to characterize the

surface energy effects has started gaining attention from several researchers in the past two decades since it offers computationally efficient techniques capable of reasonably predicting the behavior of materials at a nano-scale level.

1.2 BACKGROUND AND REVIEW

The concepts of surface energy and surface stress were originally introduced by Gibbs (1906). The quantity γ is defined to represent the excess free surface energy per unit area owing to the presence of the surface. Gibbs also remarked that to elastically stretch a pre-existing surface for solid, there is another type of fundamental parameter called the surface stress that are involved in the behavior of the surface. In order to deform such a solid, excessive work is needed to stretch the surface before straining the bulk. For better understanding, Gibbsian thermodynamics, one of the most useful tools for studying various surface phenomena, can be found in several studies of surface stresses such as Camarata (1994, 1997) and Fischer et al (2008). Camarata (1994, 1997) derived the relationship between the surface stress and surface free energy as

$$\sigma_{\alpha\beta} = \gamma\delta_{\alpha\beta} + \frac{\partial\gamma}{\partial\varepsilon_{\alpha\beta}} \tag{1.1}$$

where $\sigma_{\alpha\beta}$ and $\varepsilon_{\alpha\beta}$ denote the surface stress and surface strain, respectively, and $\delta_{\alpha\beta}$ is the two-dimensional Kronecker delta symbol. It should be noted that γ is a scalar quantity, while the surface stress is a second order tensor in the tangent plane of the surface and the strain normal to the surface is excluded in Eq. (1.1) and the Greek indices range from 1 to 2.

Fischer et al (2008) interpreted a surface as a layer attached by the excess energy where some of them are usually termed as the surface energy γ. Due to the difference between the numbers of nearest neighbors of surface atoms and those of bulk atoms, it induces a corresponding redistribution of electronic charge resulting in lesser spacing of the surface layer which differs from the bulk value (Sander, 2003). Additionally, the energy at the free surface is generally different from that of the

atoms in the bulk (Dingreville et al., 2005). The ratio of the surface free energy γ (J/m^2) and the Young's modulus E (J/m^3), denoted by γ / E (m), is an inevitable material parameter (Yakobson, 2003). This intrinsic length scale γ / E is usually small, less than one Angstrom, for metallic materials. Conversely, for soft solids such as polymer gels and biological materials, the intrinsic length scale is much larger in spite of having a little lesser surface energy γ. This is because the elastic modulus of the soft solid is nearly 7-8 orders smaller than that of conventional solids. It is obvious that the surface energy plays an important role on the properties of materials in a nano-scale level. Thus, for this particular type of problems, the material properties become size-dependent (He and Lim, 2006). Overall, in order to obtain the correct behavior of soft-solid materials or nano-scale materials, the effect of surface stresses should be integrated into the classical continuum models.

Gurtin-Murdoch model, one of the models that include the surface energy effects into the continuum models, proposed by Gurtin and Murdoch (1975, 1978) and Gurtin et al. (1998) has been extensively employed. The surface which has its own properties is assumed to be very thin and modeled as a mathematical layer of zero thickness perfectly bonded to the bulk. For an isotropic elastic surface, a linearized surface constitutive relation is given by

$$\sigma^s_{\beta\alpha} = \tau^s \delta_{\beta\alpha} + 2(\mu^s - \tau^s)\varepsilon^s_{\beta\alpha} + (\lambda^s + \tau^s)\varepsilon^s_{\gamma\gamma}\delta_{\beta\alpha} + \tau^s u_{\beta,\alpha} \tag{1.2}$$

where the superscript 's' denotes quantities corresponding to the surface, μ^s and λ^s are surface Lamé constants, and τ^s is the residual surface tension under unstrained conditions.

The validity of Gurtin-Murdoch model has been examined and verified in various investigations. For instance, Miller and Shenoy (2000) used the Gurtin-Murdoch constitutive relation to investigate the behavior of bars, beams and plates under uniaxial tension and bending. Results from their study were compared with those from atomistic simulations and good agreement among those results was deduced. Shenoy (2002) further studied the work of Miller and Shenoy (2000) by

adding the torsional rigidities of nano-sized structural elements and applied to the case of nano-scale bars in torsion. The obtained results were compared with solutions from atomistic simulations for the torsion of various metal squared bar and found in good agreement by the assumption that the surface energy depends only on the surface strain. Dingreville et al. (2005) demonstrated size-dependency of elastic properties of nano-sized particles, wires and films by deriving analytical expressions. The effective Young's modulus of thin films of various thicknesses in their analytical formulation was found in excellent agreement with their results by using molecular static (MS) simulations. Moreover, they also pointed out that their proposed formulation were much more computationally efficient than ones from MS simulations. This ensures the advantages of using continuum-based models. Consequently, Gurtin-Murdoch continuum-based model has been widely used in the study of nano-scale problems. For instance, He et al. (2004) and Huang (2008) utilized Gurtin-Murdoch constitutive relation to study the size dependence of the mechanical responses of ultra-thin elastic films. Sharma and Weeler (2007) and Sharma et al. (2003) employed the Gurtin-Murdoch model in the study of size-dependent elastic fields of spherical and ellipsoidal nano-inclusion and Tian and Rajapakse (2007a, 2007b) used the same model to investigate the size-dependent elastic field of a nano-scale circular and elliptical inhomogeneities. Furthermore, for nano-indentation problems, Zhao (2009) used the Gurtin-Murdoch model to study the mechanical responses of a classical indentation problem on a half-space with the presence of the surface energy effects for various profiles of indenters. However, his formulation was based on an incomplete Gurtin-Murdoch model since the out-of-plane contribution of the surface tension was ignored. However, their results still indicated the size-dependent behavior. Later, Pinyochotiwong et al. (2010) investigated mechanical responses of frictionless, rigid indentations acting on an elastic half-space with consideration of surface energy effects by using a complete Gurtin-Murduch model. Their numerical results also showed the size-dependency and the presence of the out-of-plane term emphasized the significance of the surface energy effects.

For surface-loading problems, Wang and Feng (2007) studied the responses of a half-plane subjected to surface pressure by considering only the influence of a

constant surface tension and ignoring the surface elastic constants. Huang and Yu (2007) extended the work of Wang and Feng (2007) by incorporating the surface elastic constants. Recently, Zhao and Rajapakse (2009) studied the near-surface responses and size dependency of a two-dimensional and an axisymmetric three-dimensional infinite elastic layers under surface loading by using Fourier and Hankel integral transform techniques. It is remarked that the Gurtin-Murdoch model used in their study was still not completed since the out-of-plane terms were ignored in their formulation. Intarit et al. (2010) studied the effect of surface stresses on the near-surface responses of semi-infinite dislocations and buried loads in a half-plane. Again, the contribution of out-of-plane terms was still not considered. Most recently, Intarit et al. (2011) generalized the work of Intarit et al. (2010) by considering the out-of-plane terms in the Gurtin-Murdoch model in the investigation of a two-dimensional elastic layer under buried loading.

On the basis of an extensive literature survey, the study of near-surface responses of a three-dimensional elastic layer using a complete Gurtin-Murdoch model has not been recognized. An analytical solution of a three-dimensional elastic layer subjected to arbitrary axisymmetric surface loads by using a complete Gurtin-Murdoch model is still not available in the literature and is the main focus of the current research. Results from this fundamental problem should be not only essential to gain insight into the nano-scale influence but also potentially useful in the investigation of more complex boundary value problems such as nano-indentations.

1.3 RESEARCH OBJECTIVES

The key objectives of this research are (i) to construct a complete analytical solution for elastic fields of an infinite, rigid-based elastic layer under the action of axisymmetric surface loadings and the surface energy effects, (ii) to investigate the influence of the surface energy effects on the elastic fields and the size-dependency, and (iii) obtain certain surface Green's functions of the corresponding layer.

1.4 RESEARCH SCOPES

The proposed investigation is to be carried out within the following context and assumptions:

1) a layer is three-dimensional with its bottom surface rigidly fixed;
2) both normal and tangential surface loads are axisymmetric;
3) a bulk material is homogeneous, isotropic and linearly elastic; and
4) surface energy effects are modeled by complete Gurtin-Murdoch surface elasticity

1.5 RESEARCH METHODOLOGY

An analytical procedure is proposed to solve a corresponding boundary value problem and the involved methodology can be briefly summarized as follows

1) Governing equations are formulated as follows. The governing equation for a bulk is expressed in terms of Love's strain potential whereas the governing equation of a surface is derived directly from the Gurtin-Murdoch surface elasticity model.
2) A general solution for the bulk is derived by using Hankel integral transform and its inversions and its final form is given in terms of arbitrary functions.
3) The boundary conditions at the top and bottom surfaces of the bulk are enforced along with applying Hankel integral transform to determine all arbitrary functions. The elastic fields (i.e. displacement and stress fields) are left in terms of the Hankel integral inversion.
4) A selected numerical integration is adopted to evaluate all involved integrals.
5) Results of elastic fields for general axisymmetric loading conditions are then specialized to construct fundamental solutions of a layer under special surface loadings.

1.6 RESEARCH SIGNIFICANCE

This research proposes a complete analytical solution of a three-dimensional, infinite elastic layer under the action of axisymmetric normal and tangential surface loading by taking surface energy effects into account. The integration of surface elasticity in the mathematical model provides an alternative, computationally cheap, continuum-based approach for investigating the influence of nano-scale on various responses of interest. As a result of using a *complete* Gurtin Murdoch constitutive relation for modeling the surface energy effects, proposed formulation can demonstrate the influence of the out-of-plane term resulting from residual surface tension on material stiffness.

Furthermore, the solution of elastic fields are also specialized to construct fundamental solutions of a layer under a unit normal concentrated force, a unit normal ring force and a unit tangential ring force. Such basic results constitute the essential basis for the development of boundary integral equations governing other related problems, e.g., nano-indentations.

CHAPTER II

THEORETICAL CONSIDERATIONS

In this chapter, an axisymmetric problem for an infinite, rigid-based elastic layer under the action of surface loads and the surface energy effects is presented. The corresponding boundary value problem is formulated based on a classical theory of linear elasticity for the bulk and a complete Gurtin-Murdoch constitutive relation for modeling the surface energy effects. Love's strain potential technique and Hankel integral transform are adopted to obtain the general solution for the bulk whereas the surface equations and conditions at the rigid based supply sufficient boundary conditions to determine all arbitrary constants.

2.1 PROBLEM DESCRIPTION

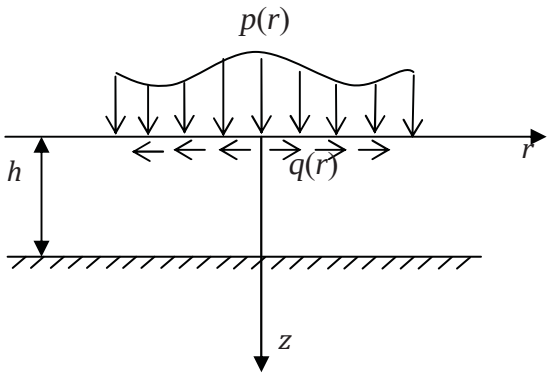

Figure 2.1 A three-dimensional, infinite, rigid-based, elastic layer subjected to axisymmetric surface loading

Consider a three-dimensional, infinite, rigid-based elastic layer of thickness h under the action of arbitrary axisymmetric surface loads as shown schematically in Figure 2.1. The reference cylindrical coordinate system is chosen such that the origin is located at the free surface and the positive z-axis directs downward whereas other axes follow the right-hand rule. The normal surface load and the tangential surface load are denoted by $p = p(r)$ and $q = q(r)$, respectively. In the modeling, the entire domain is treated as a body consisting of two different parts, the bulk which is homogeneous and isotropic and occupies a region defined by $0 < z \leq h$ and the zero-

thickness layer which occupying the plane z = 0 and is perfectly bonded to the bulk. In the present study, the medium is assumed to be free of the body force and remote loadings.

The primary objective is to determine the complete responses (e.g. the displacement and stress fields) within the bulk due to the arbitrary (axisymmetric) applied surface loads and the presence of the surface energy effects.

2.2 BASIC FIELD EQUATIONS

For the bulk, the governing field equations follow directly the classical theory of linear isotropic elasticity (e.g. Barber, 1992; Timoshenko et al., 1951). In the absence of body forces and under axisymmetric deformation, the equilibrium equations, constitutive laws and strain-displacement relations expressed in terms of cylindrical coordinates are given by

$$\frac{\partial \sigma_{rr}}{\partial r} + \frac{\partial \sigma_{rz}}{\partial z} + \frac{\sigma_{rr} - \sigma_{\theta\theta}}{r} = 0 \tag{2.1a}$$

$$\frac{\partial \sigma_{rz}}{\partial r} + \frac{\partial \sigma_{zz}}{\partial z} + \frac{\sigma_{rz}}{r} = 0 \tag{2.1b}$$

$$\sigma_{rr} = (\lambda + 2\mu)\varepsilon_{rr} + \lambda\varepsilon_{\theta\theta} + \lambda\varepsilon_{zz} \tag{2.2a}$$

$$\sigma_{\theta\theta} = \lambda\varepsilon_{rr} + (\lambda + 2\mu)\varepsilon_{\theta\theta} + \lambda\varepsilon_{zz} \tag{2.2b}$$

$$\sigma_{zz} = \lambda\varepsilon_{rr} + \lambda\varepsilon_{\theta\theta} + (\lambda + 2\mu)\varepsilon_{zz} \tag{2.2c}$$

$$\sigma_{rz} = 2\mu\varepsilon_{rz} \tag{2.2d}$$

$$\varepsilon_{rr} = \frac{\partial u_r}{\partial r} \tag{2.3a}$$

$$\varepsilon_{\theta\theta} = \frac{u_r}{r} \tag{2.3b}$$

$$\varepsilon_{zz} = \frac{\partial u_z}{\partial z} \tag{2.3c}$$

$$\varepsilon_{rz} = \frac{1}{2}\left(\frac{\partial u_r}{\partial z} + \frac{\partial u_z}{\partial r}\right) \tag{2.3d}$$

where $\{\sigma_{rr}, \sigma_{\theta\theta}, \sigma_{zz}, \sigma_{rz}\}$ are non-zero stress components; $\{\varepsilon_{rr}, \varepsilon_{\theta\theta}, \varepsilon_{zz}, \varepsilon_{rz}\}$ are non-zero strain components; $\{u_r, u_z\}$ are non-zero displacement components; and μ and λ are Lamé constants of the bulk material.

For the surface, the equilibrium conditions on the surface in terms of the generalized Young-Laplace equation (Povestenko, 1993), a complete Gurtin-Murdoch constitutive relation (e.g. put some references) and strain displacement relation are given, for the case of axisymmetry and flat surface, by

$$\frac{d\sigma_{rr}^s}{dr} + \frac{\sigma_{rr}^s - \sigma_{\theta\theta}^s}{r} + \sigma_{rz}\Big|_{z=0} + q(r) = 0 \tag{2.4a}$$

$$\frac{d\sigma_{rz}^s}{dr} + \frac{\sigma_{rz}^s}{r} + \sigma_{zz}\Big|_{z=0} + p(r) = 0 \tag{2.4b}$$

$$\sigma_{rr}^s = \tau^s + (2\mu^s + \lambda^s)\varepsilon_{rr}^s + (\lambda^s + \tau^s)\varepsilon_{\theta\theta}^s \tag{2.5a}$$

$$\sigma_{\theta\theta}^s = \tau^s + (2\mu^s + \lambda^s)\varepsilon_{\theta\theta}^s + (\lambda^s + \tau^s)\varepsilon_{rr}^s \tag{2.5b}$$

$$\sigma_{rz}^s = \tau^s \frac{du_z^s}{dr} \tag{2.5c}$$

$$\varepsilon_{rr}^s = \frac{du_r^s}{dr} \tag{2.6}$$

$$\varepsilon_{\theta\theta}^s = \frac{u_r^s}{r} \tag{2.7}$$

where the superscript ‘s’ is used to denote the quantities corresponding to the surface; μ^S and λ^S are surface Lamé constants; τ^S is the residual surface tension under unstrained conditions. By combining equations (2.4)-(2.7), it leads to two governing field equations for the surface in terms of the surface displacement:

$$\frac{d\bar{\tau}^s}{d\bar{r}}\left(1+\frac{\bar{u}_r^s}{\bar{r}}\right)+\frac{2(\bar{\lambda}+1)}{\bar{\lambda}+2}\alpha\left(\frac{d^2\bar{u}_r^s}{d\bar{r}^2}+\frac{1}{\bar{r}}\frac{d\bar{u}_r^s}{d\bar{r}}-\frac{\bar{u}_r^s}{\bar{r}^2}\right)+2(\bar{\lambda}+1)\bar{\sigma}_{rz}\Big|_{\bar{z}=0}+\bar{q}(\bar{r})=0 \tag{2.8}$$

$$\frac{d}{d\bar{r}}\left(\bar{\tau}^s\frac{d\bar{u}_z^s}{d\bar{r}}\right)+\frac{\bar{\tau}^s}{\bar{r}}\frac{d\bar{u}_z^s}{d\bar{r}}+2(\bar{\lambda}+1)\bar{\sigma}_{zz}\Big|_{z=0}+\bar{p}(\bar{r})=0 \tag{2.9}$$

where various normalized quantities appearing in (2.8) and (2.9) are defined by $\bar{\tau}^s=\tau^s/\mu\Lambda$, $\bar{u}_r^s=u_r^s/\Lambda$, $\bar{u}_z^s=u_z^s/\Lambda$, $\bar{\sigma}_{rz}=\sigma_{rz}/2(\lambda+\mu)$, $\bar{\sigma}_{zz}=\sigma_{zz}/2(\lambda+\mu)$, $\bar{\lambda}=\lambda/\mu$, $\bar{r}=r/\Lambda$, $\bar{z}=z/\Lambda$, $p=p/\mu$, $q=q/\mu$, $\Lambda=\kappa^s(\lambda+2\mu)/2\mu(\lambda+\mu)$ and $\kappa^s=2\mu_s+\lambda_s$.

2.3 GENERAL SOLUTION FOR BULK

A general solution for the normalized displacement and normalized stress of a set of governing equations (2.1)-(2.3) can readily be obtained in terms of Love’s strain potential Φ as follows (e.g. Sneddon, 1951; Selvadurai, 2000):

$$\bar{u}_r=-(\bar{\lambda}+1)\frac{\partial^2\Phi}{\partial\bar{r}\partial\bar{z}} \tag{2.10a}$$

$$\bar{u}_z=(\bar{\lambda}+2)\nabla^2\Phi-(\bar{\lambda}+1)\frac{\partial^2\Phi}{\partial\bar{z}^2} \tag{2.10b}$$

$$\bar{\sigma}_{rr}=\frac{\bar{\lambda}}{2(\bar{\lambda}+1)}\nabla^2\left(\frac{\partial\Phi}{\partial\bar{z}}\right)-\frac{\partial^3\Phi}{\partial\bar{r}^2\partial\bar{z}} \tag{2.10c}$$

$$\bar{\sigma}_{\theta\theta}=\frac{\bar{\lambda}}{2\left(\bar{\lambda}+1\right)}\nabla^2\left(\frac{\partial\Phi}{\partial\bar{z}}\right)-\frac{1}{\bar{r}}\frac{\partial^2\Phi}{\partial\bar{r}\partial\bar{z}} \tag{2.10d}$$

$$\bar{\sigma}_{zz} = \frac{(3\bar{\lambda}+4)}{2(\bar{\lambda}+1)}\nabla^2\left(\frac{\partial\Phi}{\partial\bar{z}}\right) - \frac{\partial^3\Phi}{\partial^3\bar{z}} \tag{2.10e}$$

$$\bar{\sigma}_{rz} = \frac{(\bar{\lambda}+2)}{2(\bar{\lambda}+1)}\frac{\partial}{\partial\bar{r}}(\nabla^2\Phi) - \frac{\partial^3\Phi}{\partial^2\bar{z}\partial\bar{r}} \tag{2.10f}$$

where $\nabla^2 = \frac{\partial^2}{\partial\bar{r}^2} + \frac{1}{\bar{r}}\frac{\partial}{\partial\bar{r}} + \frac{\partial^2}{\partial\bar{z}^2}$ is the axisymmetric Laplace's operator, $\bar{u}_r = u_r / \Lambda$, $\bar{u}_z = u_z / \Lambda$, $\bar{\sigma}_{rr} = \sigma_{rr} / 2(\lambda+\mu)$, and $\bar{\sigma}_{\theta\theta} = \sigma_{\theta\theta} / 2(\lambda+\mu)$. For the above field to be an elastic state, the Love's strain potential Φ must be bi-harmonic or, equivalently, satisfy the following equation

$$\nabla^4\Phi = 0 \tag{2.11}$$

Applying Hankel integral transform to the bi-harmonic equation (2.11) leads to

$$\left(\frac{d^2}{d\bar{z}^2} - \bar{\xi}^2\right)^2 G(\bar{\xi},\bar{z}) = 0 \tag{2.12}$$

where

$$G(\bar{\xi},\bar{z}) = \int_0^\infty \Phi(\bar{r},\bar{z}) J_0(\bar{\xi}\bar{r})\bar{r}d\bar{r} \tag{2.13}$$

with $J_n(\bar{\xi})$ denoting the Bessel function of the first kind of order *n*. A general solution of the homogeneous ordinary differential equation (2.12) is given by

$$G(\bar{\xi},\bar{z}) = (A + B\bar{z})e^{-\bar{\xi}\bar{z}} + (C + D\bar{z})e^{\bar{\xi}\bar{z}} \tag{2.14}$$

where *A*, *B*, *C*, and *D* are arbitrary functions of $\bar{\xi}$ and can be determined from boundary conditions.

By employing Hankel integral transform inversion, equations (2.10a)-(2.10f) can be written as

$$\bar{u}_r = (\bar{\lambda}+1)\int_0^\infty \bar{\xi}^2 \frac{dG}{d\bar{z}} J_1(\bar{\xi}\bar{r})d\bar{\xi} \tag{2.15a}$$

$$\bar{u}_z = \int_0^\infty \bar{\xi}\left[\frac{d^2G}{d\bar{z}^2} - (\bar{\lambda}+2)\bar{\xi}^2 G\right] J_0(\bar{\xi}\bar{r})d\bar{\xi} \tag{2.15b}$$

$$\bar{\sigma}_{rr} = \left(\int_0^\infty \bar{\xi}\left[\frac{\bar{\lambda}+2}{2(\bar{\lambda}+1)}\bar{\xi}^2\frac{dG}{\partial\bar{z}} + \frac{\bar{\lambda}}{2(\bar{\lambda}+1)}\frac{d^3G}{d\bar{z}^3}\right] J_0(\bar{\xi}\bar{r})d\bar{\xi}\right) - \frac{1}{\bar{r}}\int_0^\infty \bar{\xi}^2\frac{dG}{d\bar{z}} J_1(\bar{\xi}\bar{r})d\bar{\xi} \tag{2.15c}$$

$$\bar{\sigma}_{\theta\theta} = \frac{\bar{\lambda}}{2(\bar{\lambda}+1)}\int_0^\infty \bar{\xi}\left[\frac{d^3G}{d\bar{z}^3} - \bar{\xi}^2\frac{dG}{d\bar{z}}\right] J_0(\bar{\xi}\bar{r})d\bar{\xi} + \frac{1}{\bar{r}}\int_0^\infty \bar{\xi}^2\frac{dG}{d\bar{z}} J_1(\bar{\xi}\bar{r})d\bar{\xi} \tag{2.15d}$$

$$\bar{\sigma}_{zz} = \int_0^\infty \bar{\xi}\left[\frac{(\bar{\lambda}+2)}{2(\bar{\lambda}+1)}\frac{d^3G}{d\bar{z}^3} - \frac{(3\bar{\lambda}+4)}{2(\bar{\lambda}+1)}\bar{\xi}^2\frac{dG}{d\bar{z}}\right] J_0(\bar{\xi}\bar{r})d\bar{\xi} \tag{2.15e}$$

$$\bar{\sigma}_{rz} = \int_0^\infty \bar{\xi}^2\left[\frac{\bar{\lambda}}{2(\bar{\lambda}+1)}\frac{d^2G}{d\bar{z}^2} + \frac{(\bar{\lambda}+2)}{2(\bar{\lambda}+1)}\bar{\xi}^2 G(\bar{\xi},\bar{z})\right] J_1(\bar{\xi}\bar{r})d\bar{\xi} \tag{2.15f}$$

Finally, by inserting the general solution for the function G given by (2.14), the displacement and stress fields can finally be expressed in terms of the four arbitrary functions A, B, C, and D as

$$\bar{u}_r = (\bar{\lambda}+1)\int_0^\infty \bar{\xi}^2\left\{\left[-A\bar{\xi} + B(1-\bar{\xi}\bar{z})\right]e^{-\bar{\xi}\bar{z}} + \left[C\bar{\xi} + D(1+\bar{\xi}\bar{z})\right]e^{\bar{\xi}\bar{z}}\right\} J_1(\bar{\xi}\bar{r})d\bar{\xi} \tag{2.16a}$$

$$\bar{u}_z = -(\bar{\lambda}+1)\int_0^\infty \bar{\xi}^2\left\{\left[A\bar{\xi} + B(\frac{2}{(\bar{\lambda}+1)} + \bar{\xi}\bar{z})\right]e^{-\bar{\xi}\bar{z}} + \left[C\bar{\xi} - D(\frac{2}{(\bar{\lambda}+1)} - \bar{\xi}\bar{z})\right]e^{\bar{\xi}\bar{z}}\right\} J_0(\bar{\xi}\bar{r})d\bar{\xi} \tag{2.16b}$$

$$\bar{\sigma}_{rr} = \int_0^\infty \bar{\xi}^3 \left\{ \left[-A\bar{\xi} + B\left(\frac{2\bar{\lambda}+1}{\bar{\lambda}+1} - \bar{\xi}\bar{z} \right) \right] e^{-\bar{\xi}\bar{z}} + \left[C\bar{\xi} + D\left(\frac{2\bar{\lambda}+1}{\bar{\lambda}+1} + \bar{\xi}\bar{z} \right) \right] e^{\bar{\xi}\bar{z}} \right\} J_0(\bar{\xi}\bar{r}) d\bar{\xi}$$

$$-\frac{1}{\bar{r}} \int_0^\infty \bar{\xi}^2 \left(\left[-A\bar{\xi} + B(1-\bar{\xi}\bar{z}) \right] e^{-\bar{\xi}\bar{z}} + \left[C\bar{\xi} + D(1+\bar{\xi}\bar{z}) \right] e^{\bar{\xi}\bar{z}} \right) J_1(\bar{\xi}\bar{r}) d\bar{\xi} \qquad (2.16c)$$

$$\bar{\sigma}_{\theta\theta} = \frac{\bar{\lambda}}{\bar{\lambda}+1} \int_0^\infty \bar{\xi}^3 \left\{ Be^{-\bar{\xi}\bar{z}} + De^{\bar{\xi}\bar{z}} \right\} J_0(\bar{\xi}\bar{r}) d\bar{\xi}$$

$$+\frac{1}{\bar{r}} \int_0^\infty \bar{\xi}^2 \left(\left[-A\bar{\xi} + B(1-\bar{\xi}\bar{z}) \right] e^{-\bar{\xi}\bar{z}} + \left[C\bar{\xi} + D(1+\bar{\xi}\bar{z}) \right] e^{\bar{\xi}\bar{z}} \right) J_1(\bar{\xi}\bar{r}) d\bar{\xi} \qquad (2.16d)$$

$$\bar{\sigma}_{zz} = \int_0^\infty \bar{\xi}^3 \left\{ \left[A\bar{\xi} + B\left(\frac{1}{\bar{\lambda}+1} + \bar{\xi}\bar{z} \right) \right] e^{-\bar{\xi}\bar{z}} + \left[-C\bar{\xi} + D\left(\frac{1}{\bar{\lambda}+1} - \bar{\xi}\bar{z} \right) \right] e^{\bar{\xi}\bar{z}} \right\} J_0(\bar{\xi}\bar{r}) d\bar{\xi} \qquad (2.16e)$$

$$\bar{\sigma}_{rz} = \int_0^\infty \bar{\xi}^3 \left\{ \left[A\bar{\xi} - B\left(\frac{\bar{\lambda}}{\bar{\lambda}+1} - \bar{\xi}\bar{z} \right) \right] e^{-\bar{\xi}\bar{z}} + \left[C\bar{\xi} + D\left(\frac{\bar{\lambda}}{\bar{\lambda}+1} + \bar{\xi}\bar{z} \right) \right] e^{\bar{\xi}\bar{z}} \right\} J_1(\bar{\xi}\bar{r}) d\bar{\xi} \qquad (2.16f)$$

2.4 SOLUTION OF PARTICULAR BOUNDARY VALUE PROBLEM

To obtain the complete solution of a particular boundary value problem, the four arbitrary functions *A*, *B*, *C* and *D* must be determined. This can be achieved by enforcing the boundary conditions at the top and bottom surfaces of the bulk (i.e. at $z = 0$ and $z = h$). By utilizing the surface equations (2.8) and (2.9) along with assuming that the residual surface tension τ^s is constant throughout, the normal and shear stress components $\bar{\sigma}_{zz}$ and $\bar{\sigma}_{rz}$ on the top surface of the bulk must satisfy the following relations:

$$\bar{\sigma}_{zz}\big|_{\bar{z}=0} = -\frac{\beta\bar{\tau}^s}{2(\bar{\lambda}+1)}\left(\frac{d^2\bar{u}_z}{d\bar{r}^2}+\frac{1}{\bar{r}}\frac{d\bar{u}_z}{d\bar{r}}\right)-\frac{\bar{p}(\bar{r})}{2(\bar{\lambda}+1)} \tag{2.17}$$

$$\bar{\sigma}_{rz}\big|_{z=0} = -\frac{\alpha}{(\bar{\lambda}+2)}\left(\frac{d^2\bar{u}_r}{d\bar{r}^2}+\frac{1}{\bar{r}}\frac{d\bar{u}_r}{d\bar{r}}-\frac{\bar{u}_r}{\bar{r}^2}\right)-\frac{\bar{q}(\bar{r})}{2(\bar{\lambda}+1)} \tag{2.18}$$

where α is equal to 1 if the surface effect is not considered, otherwise it is zero and β is equal to 1 if the out-of-plane term is taken into account in the mathematical model, otherwise it is zero. The continuity of the displacement across the interface of the bulk and surface has also been employed, i.e. $\bar{u}_r = \bar{u}_r^s$ and $\bar{u}_z = \bar{u}_z^s$. Due to the fully fixed rigid-based condition, all components of the displacement vanish at $\bar{z} = \bar{h}$ where $\bar{h} = h/\Lambda$, i.e.

$$\bar{u}_r\big|_{\bar{z}=\bar{h}} = 0 \tag{2.19}$$

$$\bar{u}_z\big|_{\bar{z}=\bar{h}} = 0 \tag{2.20}$$

By taking Hankel integral transform of all four boundary conditions (2.17)-(2.20) along with exploiting the relations (2.16a)-(2.16f), it leads to a system of four linear algebraic equations for *A*, *B*, *C* and *D*

$$A\left(\bar{\xi}(\bar{\lambda}+1)+\beta\frac{\bar{\tau}^s}{2}\bar{\xi}^2(\bar{\lambda}+1)\right)+B\left(1+\beta\bar{\tau}^s\bar{\xi}\right)$$

$$+C\left(-\bar{\xi}(\bar{\lambda}+1)+\beta\frac{\bar{\tau}^s}{2}\bar{\xi}^2(\bar{\lambda}+1)\right)+D\left(1-\beta\bar{\tau}^s\bar{\xi}\right)=\frac{Z(\bar{\xi})}{2\bar{\xi}^2} \tag{2.21}$$

$$A\left((\bar{\lambda}+1)\bar{\xi}+\alpha\frac{(\bar{\lambda}+1)^2}{\bar{\lambda}+2}\bar{\xi}^2\right)+B\left(-\bar{\lambda}-\alpha\frac{(\bar{\lambda}+1)^2}{\bar{\lambda}+2}\bar{\xi}\right)$$

$$+C\left((\bar{\lambda}+1)\bar{\xi}-\alpha\frac{(\bar{\lambda}+1)^2}{\bar{\lambda}+2}\bar{\xi}^2\right)+D\left(\bar{\lambda}-\alpha\frac{(\bar{\lambda}+1)^2}{\bar{\lambda}+2}\bar{\xi}\right)=\frac{R(\bar{\xi})}{2\bar{\xi}^2} \tag{2.22}$$

$$\left[-A\bar{\xi}+B(1-\bar{\xi}\bar{h})\right]e^{-\bar{\xi}\bar{h}}+\left[C\bar{\xi}+D(1+\bar{\xi}\bar{h})\right]e^{\bar{\xi}\bar{h}}=0 \tag{2.23}$$

$$\left[A\bar{\xi}+B\left(\frac{2}{\bar{\lambda}+1}+\bar{\xi}\bar{h}\right)\right]e^{-\bar{\xi}\bar{h}}+\left[C\bar{\xi}+D\left(-\frac{2}{\bar{\lambda}+1}+\bar{\xi}\bar{h}\right)\right]e^{\bar{\xi}\bar{h}}=0 \tag{2.24}$$

where the functions $Z(\bar{\xi})$ and $R(\bar{\xi})$ are given in terms of the surface loads $\bar{p}(\bar{r})$ and $\bar{q}(\bar{r})$ by

$$Z\left(\bar{\xi}\right)=-\int_0^\infty \bar{p}(\bar{r})J_0(\bar{\xi}\bar{r})\bar{r}d\bar{r} \tag{2.25}$$

$$R\left(\bar{\xi}\right)=-\int_0^\infty \bar{q}(\bar{r})J_1(\bar{\xi}\bar{r})\bar{r}d\bar{r} \tag{2.26}$$

Equations (2.21)-(2.24) are sufficient for uniquely determining *A*, *B*, *C*, and *D* as functions of the transform parameter $\bar{\xi}$ and the applied surface loads $Z(\bar{\xi})$ and $R(\bar{\xi})$ and the final explicit solution is given by

$$A=\frac{1}{4}\left[\frac{A_{Z0}+\alpha A_{Z1}}{F}\right]\frac{Z(\bar{\xi})}{\bar{\xi}^3}+\frac{1}{4}\left[\frac{A_{R0}+\beta A_{R1}}{F}\right]\frac{R(\bar{\xi})}{\bar{\xi}^3} \tag{2.27a}$$

$$B=\frac{1}{4}\left[\frac{B_{Z0}+\alpha B_{Z1}}{F}\right]\frac{Z(\bar{\xi})}{\bar{\xi}^2}+\frac{1}{4}\left[\frac{B_{R0}+\beta B_{R1}}{F}\right]\frac{R(\bar{\xi})}{\bar{\xi}^2} \tag{2.27b}$$

$$C=\frac{1}{4}\left[\frac{C_{Z0}+\alpha C_{Z1}}{F}\right]\frac{Z(\bar{\xi})}{\bar{\xi}^3}+\frac{1}{4}\left[\frac{C_{R0}+\beta C_{R1}}{F}\right]\frac{R(\bar{\xi})}{\bar{\xi}^3} \tag{2.27c}$$

$$D=\frac{1}{4}\left[\frac{D_{Z0}+\alpha D_{Z1}}{F}\right]\frac{Z(\bar{\xi})}{\bar{\xi}^2}+\frac{1}{4}\left[\frac{D_{R0}+\beta D_{R1}}{F}\right]\frac{R(\bar{\xi})}{\bar{\xi}^2} \tag{2.27d}$$

where

$$
\begin{aligned}
A_{Z0} &= \frac{\bar{\lambda}(\bar{\lambda}+3)}{(\bar{\lambda}+1)^2}e^{2\bar{\xi}\bar{h}} + 2\bar{\xi}^2\bar{h}^2 - \frac{2\bar{\xi}\bar{h}\bar{\lambda}}{\bar{\lambda}+1} + \frac{\bar{\lambda}^2+3\bar{\lambda}+4}{(\bar{\lambda}+1)^2} \\
A_{Z1} &= \frac{\bar{\xi}}{\bar{\lambda}+2}\Big((\bar{\lambda}+3)(e^{2\bar{\xi}\bar{h}}-1) - 2\bar{\xi}\bar{h}(\bar{\xi}\bar{h}-1)(\bar{\lambda}+1)\Big) \\
A_{R0} &= \frac{\bar{\lambda}+3}{(\bar{\lambda}+1)^2}e^{2\bar{\xi}\bar{h}} + \frac{3\bar{\lambda}+5}{(\bar{\lambda}+1)^2} + \frac{2\bar{\xi}\bar{h}}{\bar{\lambda}+1} + 2\bar{\xi}^2\bar{h}^2 \\
A_{R1} &= \frac{\bar{\tau}^s\bar{\xi}}{2}\left[\frac{2(\bar{\lambda}+3)}{(\bar{\lambda}+1)^2}(e^{2\bar{\xi}\bar{h}}-1) - \frac{4\bar{\xi}\bar{h}}{\bar{\lambda}+1} - 2\bar{\xi}^2\bar{h}^2\right]
\end{aligned}
\tag{2.28a}
$$

$$
\begin{aligned}
B_{Z0} &= (1-2\bar{\xi}\bar{h}) + \frac{\bar{\lambda}+3}{\bar{\lambda}+1}e^{2\bar{\xi}\bar{h}} \\
B_{Z1} &= \frac{\bar{\xi}}{\bar{\lambda}+2}\Big((e^{2\bar{\xi}\bar{h}}-1)(\bar{\lambda}+3) + 2\bar{\xi}\bar{h}(\bar{\lambda}+1)\Big) \\
B_{R0} &= -(1+2\bar{\xi}\bar{h}) - \frac{\bar{\lambda}+3}{\bar{\lambda}+1}e^{2\bar{\xi}\bar{h}} \\
B_{R1} &= \frac{\bar{\tau}^s\bar{\xi}}{2}\left[\frac{\bar{\lambda}+3}{\bar{\lambda}+1}(1-e^{2\bar{\xi}\bar{h}}) + 2\bar{\xi}\bar{h}\right]
\end{aligned}
\tag{2.28b}
$$

$$
\begin{aligned}
C_{Z0} &= -\frac{\bar{\lambda}(\bar{\lambda}+3)}{(\bar{\lambda}+1)^2}e^{-2\bar{\xi}\bar{h}} - 2\bar{\xi}^2\bar{h}^2 - \frac{2\bar{\xi}\bar{h}\bar{\lambda}}{\bar{\lambda}+1} - \frac{\bar{\lambda}^2+3\bar{\lambda}+4}{(\bar{\lambda}+1)^2} \\
C_{Z1} &= \frac{\bar{\xi}}{\bar{\lambda}+2}\Big((\bar{\lambda}+3)(e^{-2\bar{\xi}\bar{h}}-1) - 2\bar{\xi}\bar{h}(1+\bar{\xi}\bar{h})(\bar{\lambda}+1)\Big) \\
C_{R0} &= \frac{\bar{\lambda}+3}{(\bar{\lambda}+1)^2}e^{-2\bar{\xi}\bar{h}} + \frac{3\bar{\lambda}+5}{(\bar{\lambda}+1)^2} - \frac{2\bar{\xi}\bar{h}}{\bar{\lambda}+1} + 2\bar{\xi}^2\bar{h}^2 \\
C_{R1} &= \frac{\bar{\tau}^s\bar{\xi}}{2}\left[-\frac{2(\bar{\lambda}+3)}{(\bar{\lambda}+1)^2}(e^{-2\bar{\xi}\bar{h}}-1) - \frac{4\bar{\xi}\bar{h}}{\bar{\lambda}+1} + 2\bar{\xi}^2\bar{h}^2\right]
\end{aligned}
\tag{2.28c}
$$

$$
\begin{aligned}
D_{Z0} &= (1+2\bar{\xi}\bar{h}) + \frac{\bar{\lambda}+3}{\bar{\lambda}+1}e^{-2\bar{\xi}\bar{h}} \\
D_{Z1} &= \frac{\bar{\xi}}{\bar{\lambda}+2}\Big((1-e^{-2\bar{\xi}\bar{h}})(\bar{\lambda}+3) + 2\bar{\xi}\bar{h}(\bar{\lambda}+1)\Big) \\
D_{R0} &= (1-2\bar{\xi}\bar{h}) + \frac{\bar{\lambda}+3}{\bar{\lambda}+1}e^{-2\bar{\xi}\bar{h}} \\
D_{R1} &= \frac{\bar{\tau}^s\bar{\xi}}{2}\left[\frac{\bar{\lambda}+3}{\bar{\lambda}+1}(1-e^{-2\bar{\xi}\bar{h}}) - 2\bar{\xi}\bar{h}\right]
\end{aligned}
\tag{2.28d}
$$

$$F=\left[\frac{\bar{\lambda}^2+4\bar{\lambda}+5}{\bar{\lambda}+1}+2\bar{h}\bar{\xi}^2(\bar{h}+\alpha)(\bar{\lambda}+1)+(\bar{\lambda}+3)\left(\cosh(2\bar{\xi}\bar{h})+\alpha\bar{\xi}\sinh(2\bar{\xi}\bar{h})\right)\right]$$
$$+\beta\frac{\bar{\tau}^s\bar{\xi}}{2}\left[(\bar{\lambda}+3)\frac{\bar{\lambda}+2}{\bar{\lambda}+1}\sinh(2\bar{\xi}\bar{h})-2\bar{\xi}\bar{h}(\bar{\lambda}+2)+\frac{\bar{\xi}\alpha}{\bar{\lambda}+2}\left((\bar{\lambda}+3)^2\cosh(2\bar{\xi}\bar{h})-(\bar{\lambda}+3)^2-2\bar{\xi}^2\bar{h}^2(\bar{\lambda}+1)\right)\right] \tag{2.28e}$$

Once the functions *A*, *B*, *C*, and *D* are obtained from (2.27)-(2.28), both the displacement and stress at any point within the bulk can be computed from (2.16a)-(2.16f). Numerical evaluation of all involved integral is briefly discussed in the next chapter.

It is evident that by setting the parameters α and β to zero, the solution obtained is identical to that of a classical problem of a three-dimensional, infinite elastic layer under surface loadings (Sneddon, 1951; Selvadurai, 2000). Furthermore, by setting β to zero, the above results reduce to those presented by Zhao and Rajapakse (2009) and Zhao (2009). These two special benchmark solutions can be employed in the verification procedure. In addition, results for the special case of a half space can also be obtained by simply taking sufficiently large layer thickness *h*.

CHAPTER III

NUMERICAL IMPREMENTATION

Although all functions *A*, *B*, *C*, and *D* are obtained in a closed form in terms of the transform parameter $\bar{\xi}$, determination of the displacement and stress fields still requires the evaluation of integrals corresponding to Hankel transform inversion. It is apparent that all involved integrals contain relatively complex integrands and they cannot be directly integrated to obtain a closed form elastic field. In this chapter, a selected numerical technique for efficiently and accurately integrating those integrals is outlined below.

3.1 TRUNCATION

It is evident that all integrals appearing in (2.16a)-(2.16f) are improper integrals with their lower and upper limits equal to zero and infinity, respectively. To evaluate such integrals numerically, it is common to truncate the domain of integration from $[0,\infty)$ to $[0,\bar{\xi}_R]$ where $\bar{\xi}_R$ is a finite real number. The approximate displacement and stress fields in terms of the truncated integrals are given by

$$\bar{u}_r = (\bar{\lambda}+1)\int_0^{\bar{\xi}_R} \bar{\xi}^2 \left\{ \left[-A\bar{\xi} + B(1-\bar{\xi}\bar{z}) \right] e^{-\bar{\xi}\bar{z}} + \left[C\bar{\xi} + D(1+\bar{\xi}\bar{z}) \right] e^{\bar{\xi}\bar{z}} \right\} J_1(\bar{\xi}\bar{r}) d\bar{\xi} \qquad (3.1a)$$

$$\bar{u}_z = -(\bar{\lambda}+1)\int_0^{\bar{\xi}_R} \bar{\xi}^2 \left\{ \left[A\bar{\xi} + B\left(\frac{2}{(\bar{\lambda}+1)} + \bar{\xi}\bar{z}\right) \right] e^{-\bar{\xi}\bar{z}} + \left[C\bar{\xi} - D\left(\frac{2}{(\bar{\lambda}+1)} - \bar{\xi}\bar{z}\right) \right] e^{\bar{\xi}\bar{z}} \right\} J_0(\bar{\xi}\bar{r}) d\bar{\xi} \qquad (3.1b)$$

$$\bar{\sigma}_{rr} = \int_0^{\bar{\xi}_R} \bar{\xi}^3 \left\{ \left[-A\bar{\xi} + B\left(\frac{2\bar{\lambda}+1}{\bar{\lambda}+1} - \bar{\xi}\bar{z} \right) \right] e^{-\bar{\xi}\bar{z}} + \left[C\bar{\xi} + D\left(\frac{2\bar{\lambda}+1}{\bar{\lambda}+1} + \bar{\xi}\bar{z} \right) \right] e^{\bar{\xi}\bar{z}} \right\} J_0(\bar{\xi}\bar{r}) d\bar{\xi}$$

$$-\frac{1}{\bar{r}}\int_0^{\bar{\xi}_R} \bar{\xi}^2 \left(\left[-A\bar{\xi} + B(1-\bar{\xi}\bar{z}) \right] e^{-\bar{\xi}\bar{z}} + \left[C\bar{\xi} + D(1+\bar{\xi}\bar{z}) \right] e^{\bar{\xi}\bar{z}} \right) J_1(\bar{\xi}\bar{r}) d\bar{\xi} \qquad (3.1c)$$

$$\bar{\sigma}_{\theta\theta} = \frac{\bar{\lambda}}{\bar{\lambda}+1}\int_0^{\bar{\xi}_R} \bar{\xi}^3 \left\{ Be^{-\bar{\xi}\bar{z}} + De^{\bar{\xi}\bar{z}} \right\} J_0(\bar{\xi}\bar{r}) d\bar{\xi}$$

$$+\frac{1}{\bar{r}}\int_0^{\bar{\xi}_R} \bar{\xi}^2 \left(\left[-A\bar{\xi} + B(1-\bar{\xi}\bar{z}) \right] e^{-\bar{\xi}\bar{z}} + \left[C\bar{\xi} + D(1+\bar{\xi}\bar{z}) \right] e^{\bar{\xi}\bar{z}} \right) J_1(\bar{\xi}\bar{r}) d\bar{\xi} \qquad (3.1d)$$

$$\bar{\sigma}_{zz} = \int_0^{\bar{\xi}_R} \bar{\xi}^3 \left\{ \left[A\bar{\xi} + B\left(\frac{1}{\bar{\lambda}+1} + \bar{\xi}\bar{z} \right) \right] e^{-\bar{\xi}\bar{z}} + \left[-C\bar{\xi} + D\left(\frac{1}{\bar{\lambda}+1} - \bar{\xi}\bar{z} \right) \right] e^{\bar{\xi}\bar{z}} \right\} J_0(\bar{\xi}\bar{r}) d\bar{\xi} \quad (3.1e)$$

$$\bar{\sigma}_{rz} = \int_0^{\bar{\xi}_R} \bar{\xi}^3 \left\{ \left[A\bar{\xi} - B\left(\frac{\bar{\lambda}}{\bar{\lambda}+1} - \bar{\xi}\bar{z} \right) \right] e^{-\bar{\xi}\bar{z}} + \left[C\bar{\xi} + D\left(\frac{\bar{\lambda}}{\bar{\lambda}+1} + \bar{\xi}\bar{z} \right) \right] e^{\bar{\xi}\bar{z}} \right\} J_1(\bar{\xi}\bar{r}) d\bar{\xi} \quad (3.1f)$$

While the convergence of the above approximate solution to an analytical solution is ensured as $\bar{\xi}_R$ approaches infinity, it is standard, in the numerical calculation, to choose a sufficiently large number $\bar{\xi}_R$ such that the error from the approximation is less than a specified tolerance.

3.2 INTERVAL SUBDIVISION

Due to the oscillating nature of their integrands, the numerical integration of involved integrals in (2.16a)-(2.16f) by using Gaussian quadrature over a single interval requires a large number of integrations points. To enhance the accuracy and computational efficiency, the interval $[0, \bar{\xi}_R]$ is first partitioned into *N* sub-intervals denoted by $[\bar{\xi}_0 = 0, \bar{\xi}_1]$, $[\bar{\xi}_1, \bar{\xi}_2]$, $[\bar{\xi}_2, \bar{\xi}_3]$, …, $[\bar{\xi}_{N-1}, \bar{\xi}_N = \bar{\xi}_R]$ and the integral over the interval $[0, \bar{\xi}_R]$ is obtained from the sum of all sub-integrals over each sub-interval as follows:

$$\int_0^{\bar{\xi}_R} f(\bar{\xi}) d\bar{\xi} = \int_{\bar{\xi}_{0=0}}^{\bar{\xi}_1} f(\bar{\xi}) d\bar{\xi} + \int_{\bar{\xi}_1}^{\bar{\xi}_2} f(\bar{\xi}) d\bar{\xi} + \ldots + \int_{\bar{\xi}_{N-2}}^{\bar{\xi}_{N-1}} f(\bar{\xi}) d\bar{\xi} + \int_{\bar{\xi}_{N-1}}^{\bar{\xi}_N = \bar{\xi}_R} f(\bar{\xi}) d\bar{\xi} \quad (3.2)$$

where $f = f(\bar{\xi})$ denotes any integrand. As the number of sub-intervals increases, the oscillating behavior of the integrand in each sub-interval should disappear and they can accurately be integrated by using low-order Gaussian quadrature.

3.3 NUMERICAL QUADRATURE

By using the change of variable, the Gaussian quadrature formula for each sub-interval in (3.2) is given by

$$\int_{\bar{\xi}_{i-1}}^{\bar{\xi}_i} f(\bar{\xi})d\bar{\xi} = \int_{-1}^{1} f(\bar{\xi}(\xi^*))Jd\xi^* = \sum_{i=1}^{n} f(\bar{\xi}(\xi_i^*))Jw_i \tag{3.3}$$

where $\bar{\xi} = (1-\xi^*)\bar{\xi}_{i-1}/2 + (1+\xi^*)\bar{\xi}_i/2$, $(\bar{\xi}_i - \bar{\xi}_{i-1})/2$ denotes the jacobian of transformation, ξ_i^* is the location of an integration point, w_i is the corresponding weight, and n is the number of integration points.

3.4 CONVERGENCE STUDY

In the present study, extensive numerical experiments are to be performed to investigate the influence of the truncation parameter $\bar{\xi}_R$, the number of sub-intervals N, and the number of integration points n on the accuracy of the numerical integration. Such three parameters must be chosen properly to ensure the accuracy of the numerical results while consuming reasonable computational time.

Both the number of integration points and the number of sub-intervals have a direct impact on the accuracy of the numerical integration for a fixed truncation parameter $\bar{\xi}_R$. In general, by increasing the number of sub-intervals, each sub-integral over each sub-interval requires less number of integration points since the oscillating behavior of the integrand gradually disappear. In the present study, for a fixed truncation parameter $\bar{\xi}_R$, the number of sub-intervals N is increased until the integral can be integrated correctly (for a specified tolerance) by using a low order Gaussian quadrature over each sub-interval. The ratio $\bar{\xi}_R / N$ is then computed and used to indicate the size of the sub-interval over which the integrand is sufficiently well-

behaved to be integrated using low order Gaussian quadrature. Finally, a proper choice of the truncation parameter $\bar{\xi}_R$ is obtained by increasing such upper limit until the value of the integral converges or remain unchanged (for a specified tolerance). It is important to remark that in such process, the number of sub-intervals must be increased accordingly in order to maintain the size of the sub-intervals ($\bar{\xi}_R / N$) to be sufficiently small to allow the integration by low-order Gaussian quadrature.

CHAPTER IV

NUMERICAL RESULTS

In order to determine all elastic fields by the selected numerical technique mentioned in chapter 3, a computer code must be implemented and then verified by comparing with available benchmark solutions to assure its accuracy. After that, extensive studies for both cases of axisymmetric normal and axisymmetric tangential surface loads are investigated to understand the nano-scale influence through the surface stress effects (with/without the contribution of residual surface tension) and size dependent behaviors. Moreover, numerical results of a layer under a unit normal point load, a unit normal ring load and a unit tangential ring load which are benefit for solving nano-indentations problem are also demonstrated and fully discussed.

4.1 VERIFICATIONS

Numerical results obtained from the developed computer program are verified with various benchmark solutions. For examples, numerical solutions without surface energy effects of an elastic layer under normal concentrated load are compared with analytical solutions presented by Bumister (1943, 1945) and those of a half-space subjected to uniformly distributed vertical load are verified with solutions of Ahlvin and Ulery (1962). Furthermore, numerical results with no surface energy effects and numerical results accounted for surface energy effects without the contribution of the out-of-plane term of an elastic layer under uniformly normal distributed load are compared with those proposed by Zhao (2009). As evident from results presented further below, numerical solutions obtained from the present study exhibit excellent agreement with the benchmark solutions.

4.1.1 Infinite Rigid-based Elastic Layer Under Normal Point Force

Consider a normal point load $\overline{P}_{pt} = P_{pt} / \mu\Lambda^2$ acting to the surface of a rigid-based layer with the normalized thickness $\overline{h} = 1.0$ and the Poisson's ratio $\upsilon = 0.2$ as

shown in figure 4.1. Without consideration of surface energy effects, the analytical solution derived by Bumister (1943, 1945) and tabulated by Poulos (1967b) are employed to verify the accuracy of the present study. Numerical solutions for this classical case can readily be obtained in the present study by setting $\alpha = 0$ and $\beta = 0$. The radial and vertical displacements at the surface and non-zero stress components at $\bar{z} = 0.1$ along the radial direction are reported in Tables 4.1-4.3. It is obvious that numerical results from the present study show good agreement with the analytical solution of Bumister (1943, 1945).

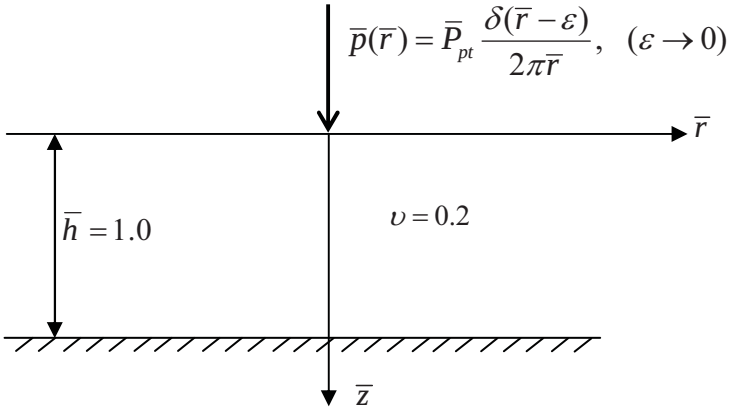

Figure 4.1 Three-dimensional, infinite, rigid-based, elastic layer subjected to a normal point load

Table 4.1 Normalized vertical and radial displacements of a three-dimensional, infinite, rigid-based, elastic layer subjected to a normal point load

$\bar{r}$	$2\pi\bar{h}\bar{E}\bar{u}_r / \bar{P}_{pt}$		$2\pi\bar{h}\bar{E}\bar{u}_z / \bar{P}_{pt}$	
	Bumister (1943, 1945)	**Current study**	**Bumister (1943, 1945)**	**Current study**
0.05	-14.362	-14.344	35.921	35.310
0.1	-7.124	-7.172	16.728	16.554
0.2	-3.455	-3.477	7.162	7.195
0.3	-2.184	-2.178	4.016	4.050
0.4	-1.523	-1.512	2.478	2.473
0.5	-1.064	-1.109	1.599	1.579
0.6	-0.824	-0.830	1.048	1.048
0.7	-0.62	-0.620	0.69	0.704
0.8	-0.465	-0.461	0.45	0.458

Table 4.2 Normalized vertical and radial stress components of a three-dimensional, infinite, rigid-based, elastic layer subjected to a normal point load

$\bar{r}$	$4\pi\bar{h}^2(\bar{\lambda}+1)\bar{\sigma}_{zz}/\bar{P}_{pt}$		$4\pi\bar{h}^2(\bar{\lambda}+1)\bar{\sigma}_{rr}/\bar{P}_{pt}$	
	Bumister (1943, 1945)	**Current study**	**Bumister (1943, 1945)**	**Current study**
0	300	300	-30.71	-30.72
0.1	53.08	53.06	34.75	34.75
0.2	5.415	5.395	12.5	12.49
0.3	0.994	0.974	3.347	3.344
0.4	0.293	0.273	0.614	0.611
0.5	0.124	0.103	-0.259	-0.262
0.6	0.067	0.048	-0.528	-0.530
0.7	0.041	0.025	-0.578	-0.579
0.8	0.026	0.013	-0.544	-0.544
0.9	0.016	0.006	-0.479	-0.478

Table 4.3 Normalized shear and hoop stress components of a three-dimensional, infinite, rigid-based, elastic layer subjected to a normal point load

$\bar{r}$	$4\pi\bar{h}^2(\bar{\lambda}+1)\bar{\sigma}_{rz}/\bar{P}_{pt}$		$4\pi\bar{h}^2(\bar{\lambda}+1)\bar{\sigma}_{\theta\theta}/\bar{P}_{pt}$	
	Bumister (1943, 1945)	**Current study**	**Bumister (1943, 1945)**	**Current study**
0	0	0.000	-30.71	-30.720
0.1	53	53.003	-4.342	-4.355
0.2	10.68	10.676	2.237	2.224
0.3	2.765	2.765	1.996	1.983
0.4	0.909	0.908	1.349	1.337
0.5	0.326	0.324	0.877	0.865
0.6	0.102	0.099	0.566	0.554
0.7	0.005	0.002	0.363	0.352
0.8	-0.038	-0.043	0.231	0.221
0.9	-0.056	-0.061	0.144	0.135

4.1.2 Elastic Half-space Under Uniformly Distributed Normal Traction

A three-dimensional, elastic half-space with Poisson's ratio $\upsilon = 0.2$ under the action of a uniformly distributed normal traction p_0 over a circular area of normalized radius $\bar{a} = a / \Lambda$ shown in Figure 4.2 is considered (excluding the surface energy effects). In this case, the exact solution tabulated by Ahlvin and Ulery (1962) has been employed as a benchmark solution. Again, in the analysis, α and β are set to be zero in order to specialize the problem into the classical case and the normalized thickness $\bar{h}$ must be chosen to be sufficiently large to represent the elastic half-space. Results for non-zero displacement and stress components are reported in Table 4.4 along with those of Ahlvin and Ulery (1962). It is evident that solutions obtained from the current study are almost indistinguishable from the reference results.

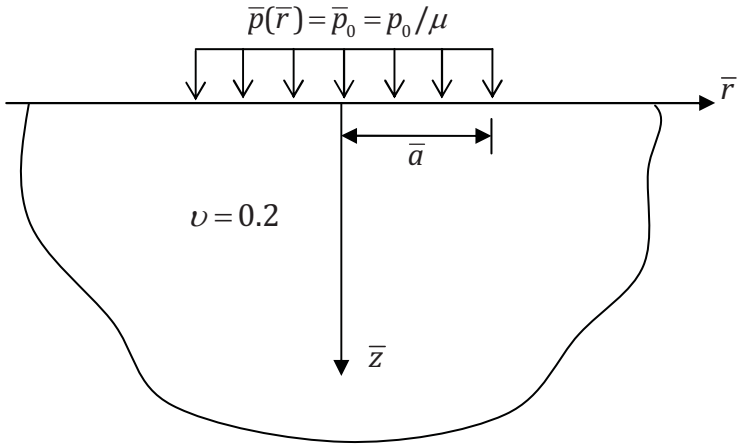

Figure 4.2 Three-dimensional, infinite, elastic half-space subjected to a uniformly distributed normal traction

Table 4.4 Normalized displacement and stress components of a three-dimensional, infinite, elastic half-space subjected to a uniformly distributed normal traction

$\bar{z}/\bar{a}$	$2(\bar{\lambda}+1)\bar{\sigma}_{zz}/\bar{p}_0$		$2(\bar{\lambda}+1)\bar{\sigma}_{rr}/\bar{p}_0$		$2(\bar{\lambda}+1)\bar{\sigma}_{\theta\theta}/\bar{p}_0$		$\bar{u}_z/\bar{p}_0$	
	Ahlvin and Ulery (1962)	**Current study**	**Ahlvin and Ulery (1962)**	**Current study**	**Ahlvin and Ulery (1962)**	**Current study**	**Ahlvin and Ulery (1962)**	**Current study**
0	1.000	0.993	0.700	0.695	0.700	0.695	0.800	0.800
0.1	0.999	0.999	0.581	0.581	0.581	0.581	0.769	0.769
0.2	0.992	0.992	0.468	0.468	0.468	0.468	0.736	0.736
0.3	0.976	0.976	0.367	0.367	0.367	0.367	0.702	0.702
0.4	0.949	0.949	0.280	0.280	0.280	0.280	0.667	0.667
0.5	0.911	0.911	0.208	0.208	0.208	0.208	0.633	0.633
0.6	0.864	0.864	0.151	0.151	0.151	0.151	0.599	0.599
0.7	0.811	0.811	0.106	0.106	0.106	0.106	0.566	0.566
0.8	0.756	0.756	0.072	0.072	0.072	0.072	0.535	0.535
0.9	0.701	0.701	0.047	0.047	0.047	0.047	0.505	0.505
1	0.646	0.646	0.028	0.028	0.028	0.028	0.478	0.478
1.2	0.547	0.547	0.005	0.005	0.005	0.005	0.429	0.429
1.5	0.424	0.424	-0.010	-0.010	-0.010	-0.010	0.368	0.368
2	0.284	0.284	-0.016	-0.016	-0.016	-0.016	0.294	0.294
2.5	0.200	0.200	-0.014	-0.014	-0.014	-0.014	0.243	0.243
3	0.146	0.146	-0.012	-0.012	-0.012	-0.012	0.207	0.207
4	0.087	0.087	-0.008	-0.008	-0.008	-0.008	0.158	0.158
5	0.057	0.057	-0.005	-0.005	-0.005	-0.005	0.128	0.128
6	0.040	0.040	-0.004	-0.004	-0.004	-0.004	0.107	0.107
7	0.030	0.030	-0.003	-0.003	-0.003	-0.003	0.092	0.092
8	0.023	0.023	-0.002	-0.002	-0.002	-0.002	0.081	0.081
9	0.018	0.018	-0.002	-0.002	-0.002	-0.002	0.072	0.072

Table 4.5 Material properties used in numerical study

Model Parameter	**Value (unit)**
λ	58.17×10^9 (N/m^2)
μ	26.13×10^9 (N/m^2)
λ^s	6.8511 (N/m)
μ^s	-0.376 (N/m)
τ^s	1 (N/m)

4.1.3 Infinite Rigid-based Elastic Layer Under Uniformly Distributed Normal Traction

Consider an infinite rigid-based elastic layer under a uniformly distributed normal traction p_0 acting over a circular area of normalized radius $\bar{a}=10.0$ and with the normalized layer thickness $\bar{h}=30$ as shown in Figure 4.3. To allow a direct comparison of available results proposed by Zhao (2009), the same set of material constants obtained from atomistic simulation (Miller and Shenoy, 2000; Shenoy, 2005) is utilized and they are summarized in Table 4.5. Results for the classical case and the case accounting for the surface energy effects but ignoring the out-of-plane term can be obtained by simply setting $\alpha=0,\beta=0$ and $\alpha=1,\beta=0$, respectively. By comparing results for the surface displacement and stresses at $\bar{z}=0.1$ along the radial direction with those presented by Zhao (2009) for $\bar{h}/\bar{a}=3$, it is found that solutions obtained from the present study are in excellent agreement with the benchmark solutions as shown in Figures 4.4-4.6.

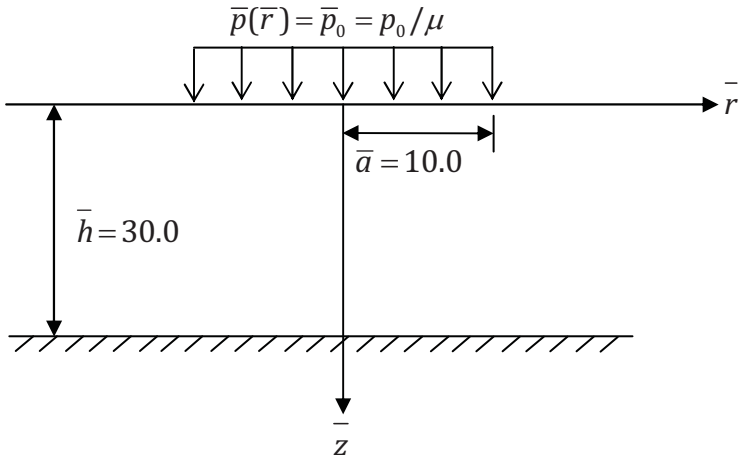

Figure 4.3 Three-dimensional, infinite, rigid-based, elastic layer subjected to a uniformly distributed normal traction

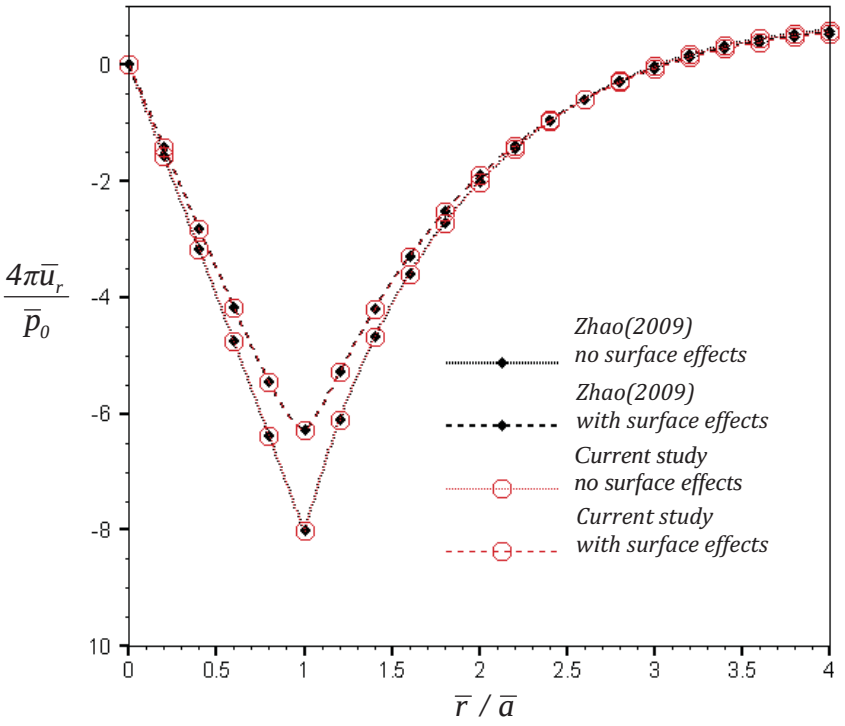

(a)

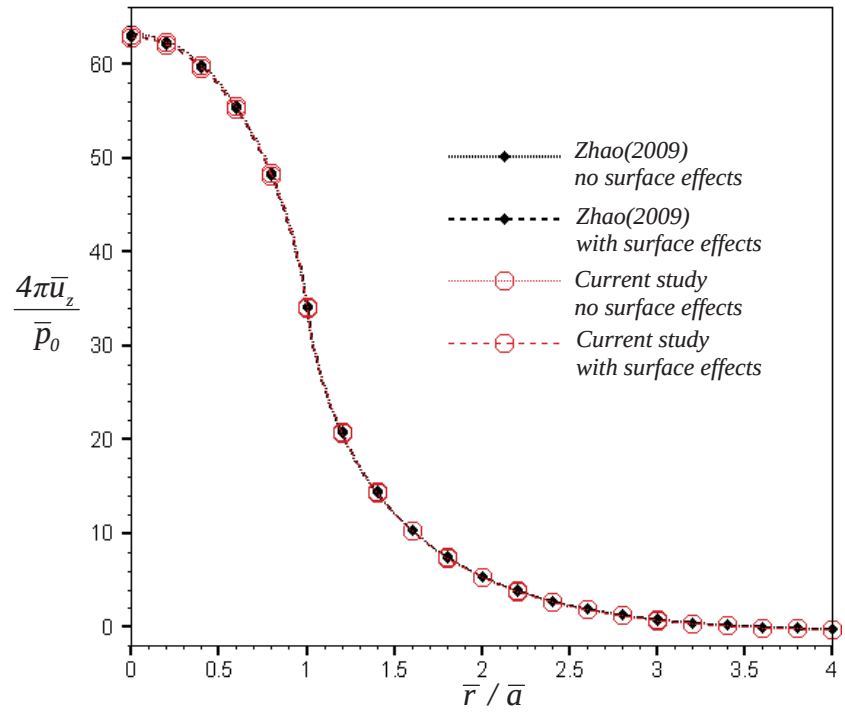

(b)

Figure 4.4 Normalized displacement profiles of an elastic layer under a uniformly distrubuted normal traction: (a) radial displacement and (b) vertical displacement

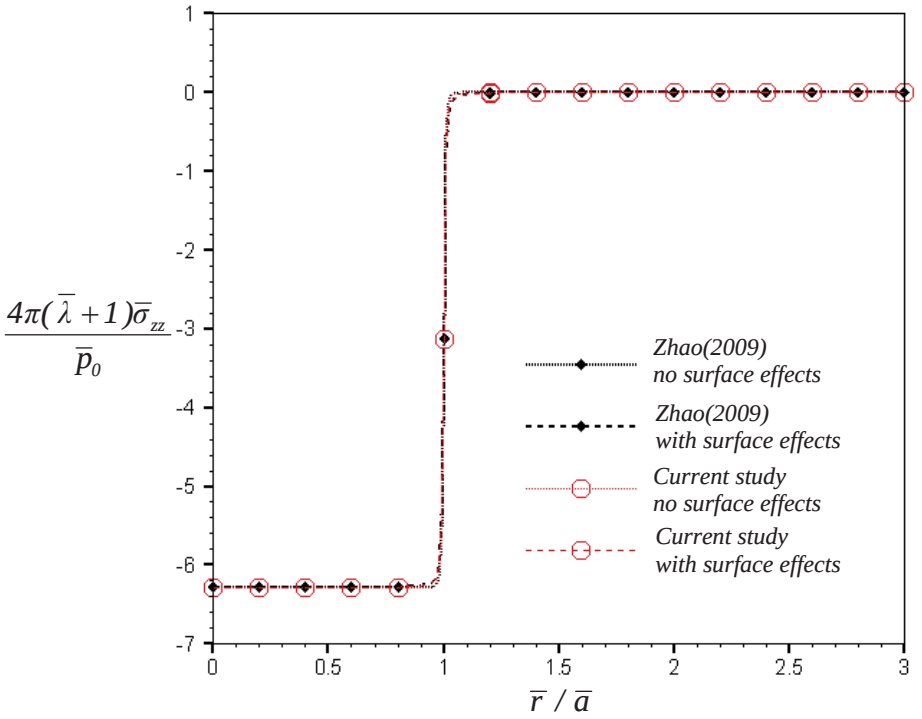

(a)

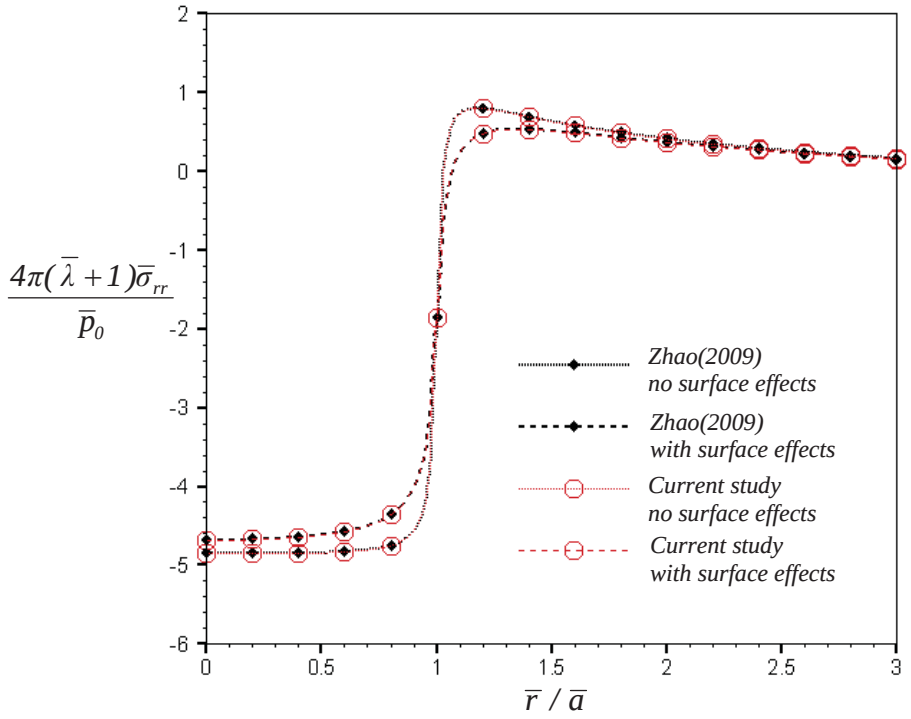

(b)

Figure 4.5 Normalized stress profiles of an elastic layer under a uniformly distrubuted normal traction: (a) vertical stress and (b) radial stress

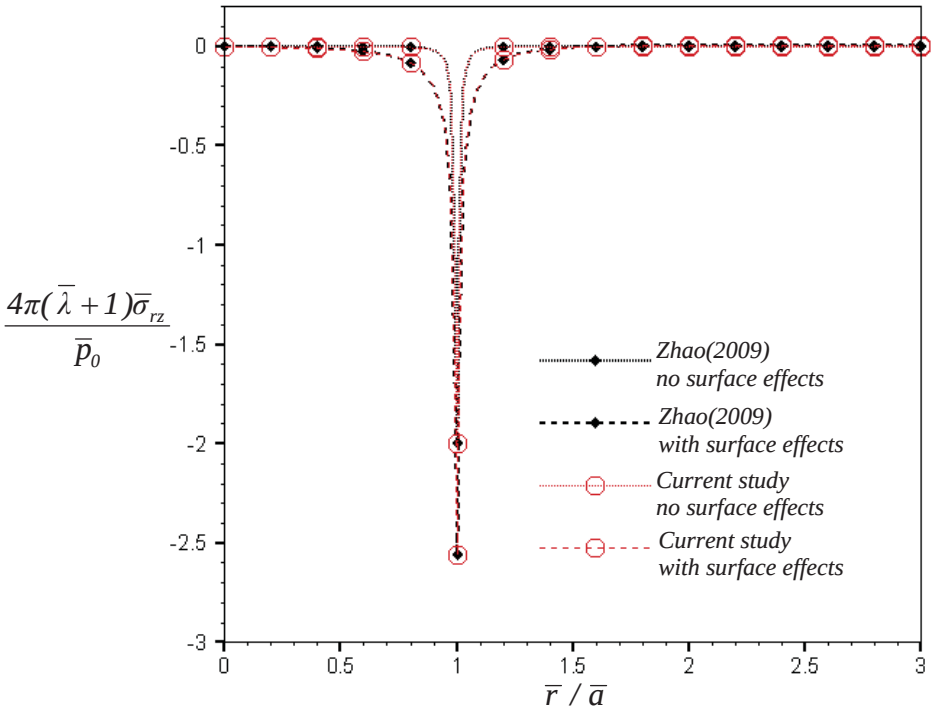

(a)

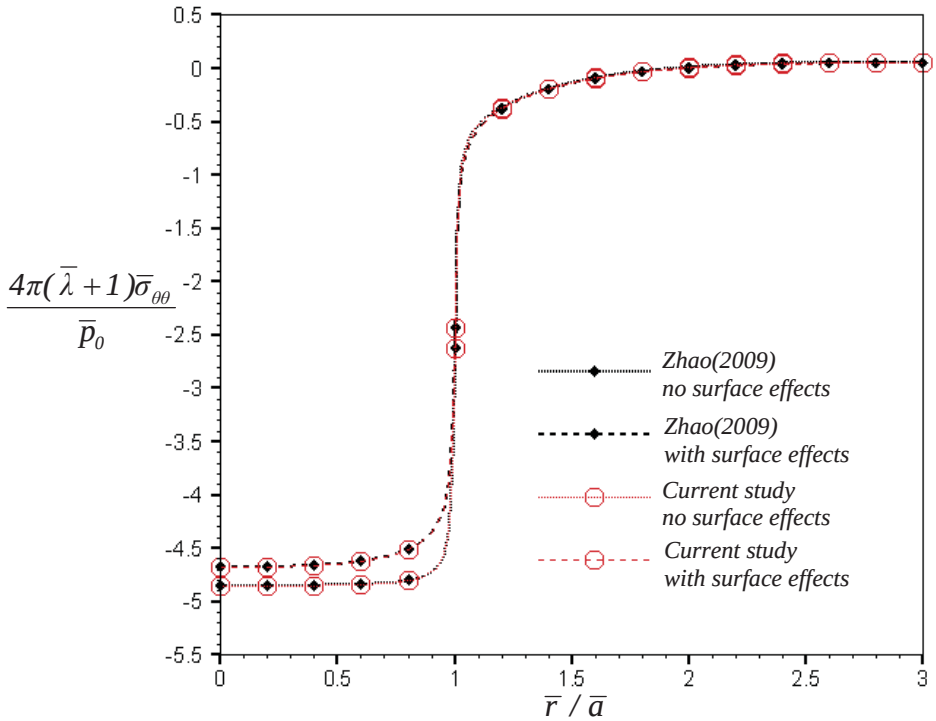

(b)

Figure 4.6 Normalized stress profiles of an elastic layer under a uniformly distrubuted normal traction: (a) shear stress and (b) hoop stress

4.2 NUMERICAL RESULTS AND DISCUSSION

After the formulation and numerical implementation are verified for both the classical case and the case accounting for the surface stress effects but ignoring the out-of-plane term, the proposed model (including the out-of-plane term) is then utilized to investigate the influence of the surface stress effects on elastic fields and demonstrate the significant role of the out-of-plane term in Gurtin-Murdoch surface elasticity model. By using material properties summarized in Table 4.5, numerical results and size-dependent behaviors for both normal and tangential directions of axisymmetric surface loads are illustrated and discussed.

4.2.1 Uniformly Distributed Normal Traction

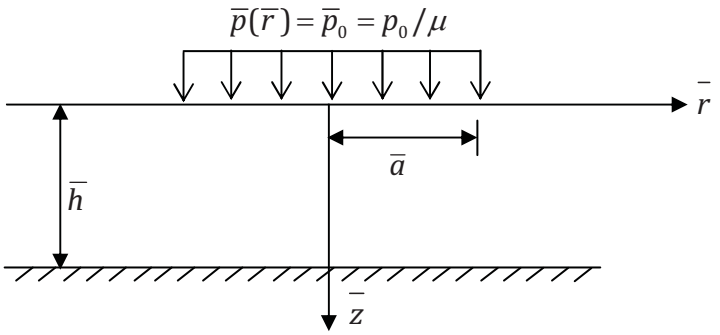

Figure 4.7 Three-dimensional, infinite, rigid-based, elastic layer subjected to a uniformly distributed normal traction

Consider an infinite, rigid-based elastic layer under a uniformly distributed normal traction p_0 (with $\bar{p}_0 = p_0/\mu$) acting on a circular region of radius a (with $\bar{a} = a/\Lambda$) as shown in Figure 4.7. Results for both radial and vertical displacements on the surface along the radial direction for $\bar{a} = 10.0$ and various normalized thicknesses ($\bar{h} = h/\Lambda$) are shown in Figure 4.8(a)-(b), respectively. It is apparent from this set of results that a model incorporating the out-of-plane term predicts much lower surface displacement or, equivalently, renders materials stiffer while the solution obtained from a model excluding the out-of-plane term exhibits significant influence of the surface energy effects only in the case of the radial displacement. Hence, the influence of the out-of-plane term is significant and, in general, cannot be neglected. In addition, results for all cases show similar trend for various $\bar{h}$. In particular, magnitude of the displacement is higher as the layer thickness increases.

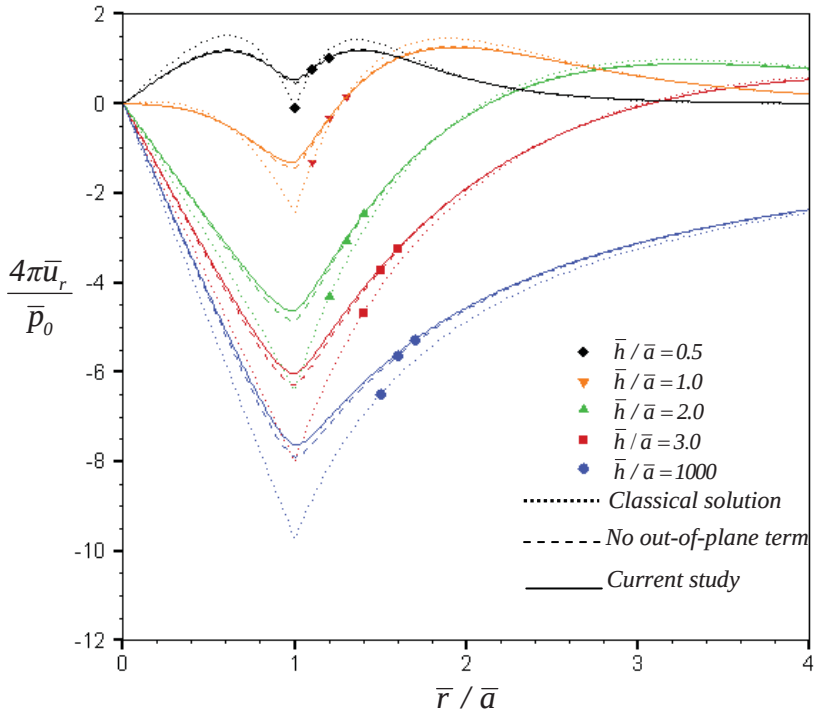

(a)

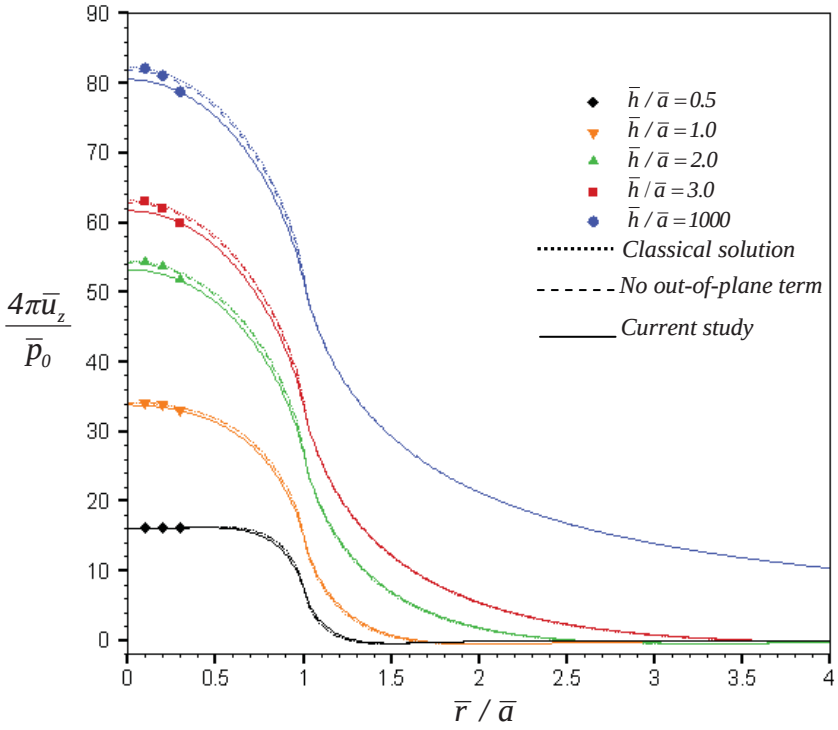

(b)

Figure 4.8 Normalized displacement profiles of an elastic layer under a uniformly distrubuted normal traction: (a) radial displacement and (b) vertical displacement

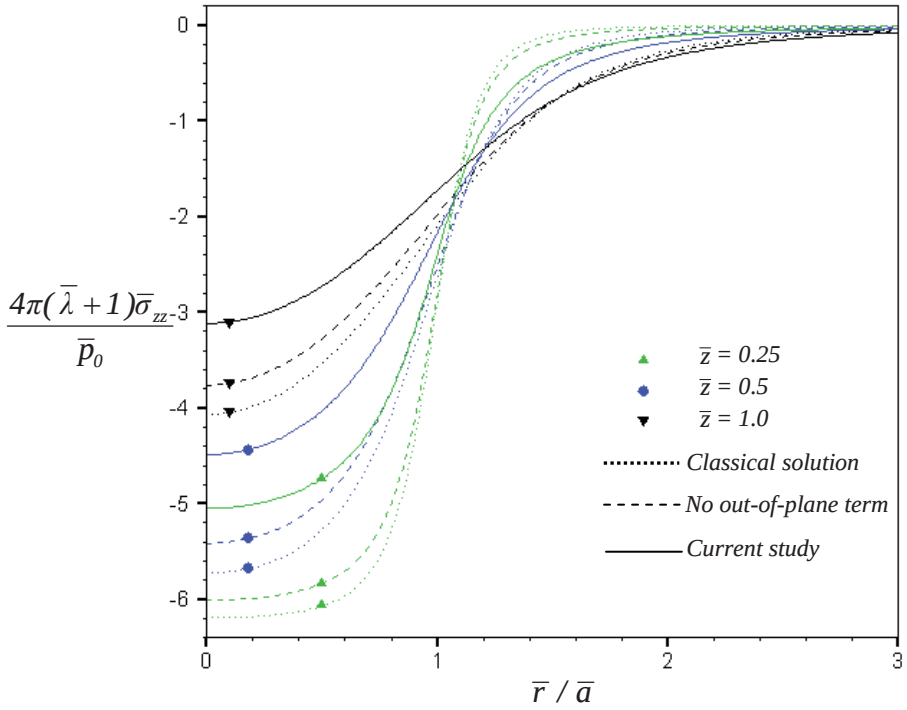

(a)

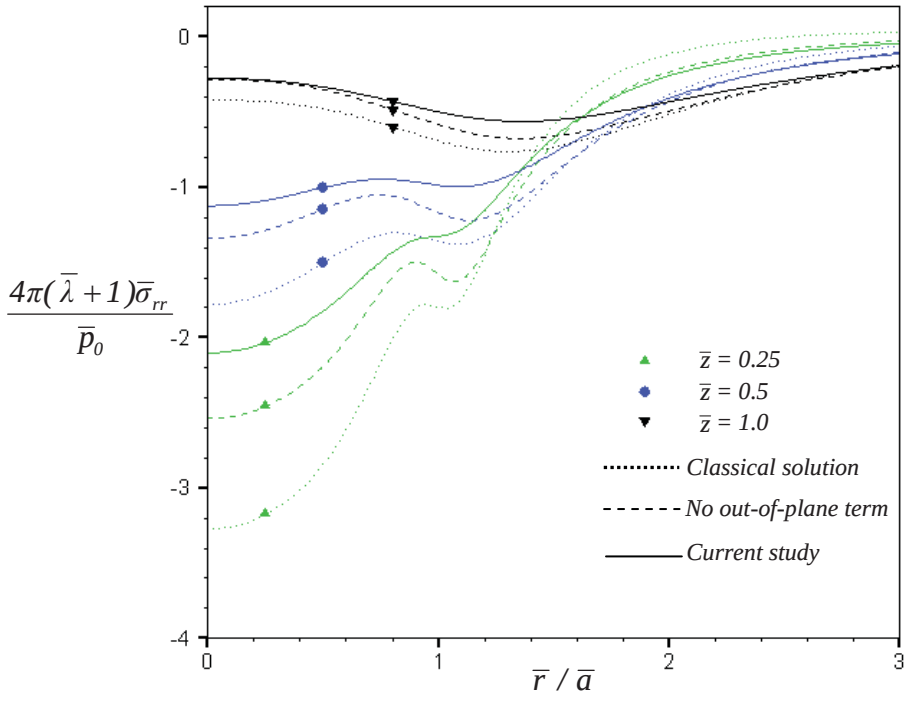

(b)

Figure 4.9 Normalized stress profiles of an elastic layer under a uniformly distrubuted normal traction: (a) vertical stress and (b) radial stress

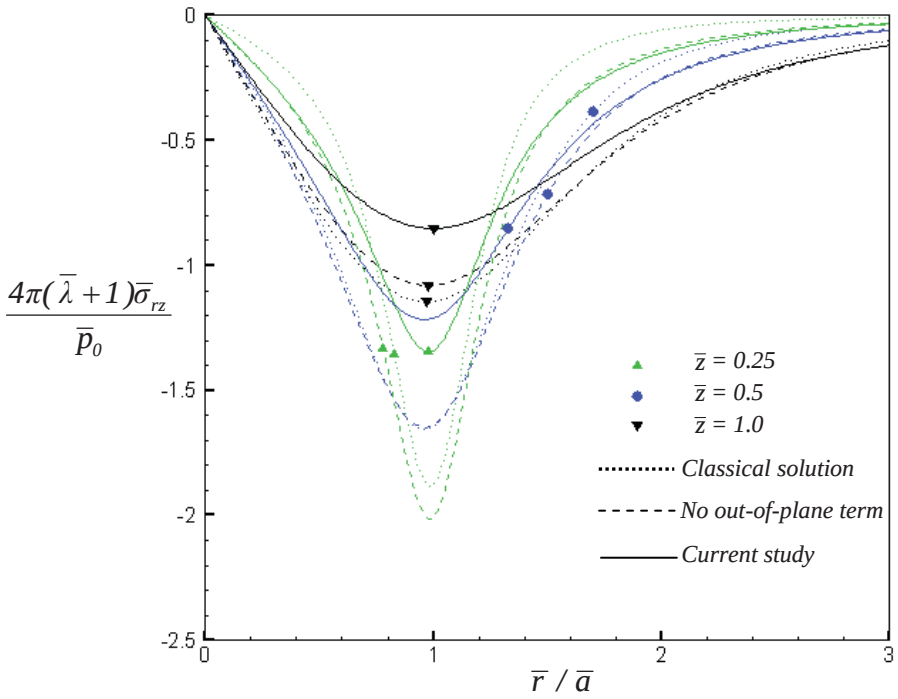

(a)

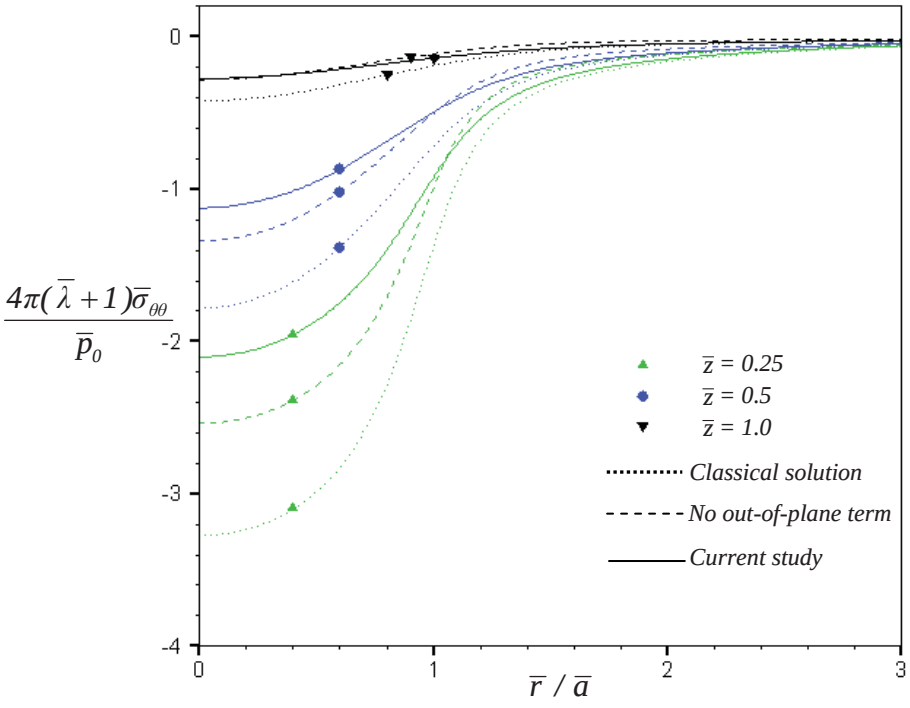

(b)

Figure 4.10 Normalized stress profiles of an elastic layer under a uniformly distrubuted normal traction: (a) shear stress and (b) hoop stress

For non-zero stress components, results are reported for $\bar{h} = 10$ and $\bar{a} = 1$ at three different normalized depths ($\bar{z} = 0.25, \bar{z} = 0.5, \bar{z} = 1.0$). The variation of the normalized vertical stress $4\pi(\bar{\lambda}+1)\bar{\sigma}_{zz} / \bar{p}_0$ in the radial direction is shown in Figure 4.9(a). Clearly, the vertical stresses for all cases reach their maximum at $\bar{r} = 0$ and rapidly decrease to zero when $\bar{r}$ is near the edge of the surface loading, i.e. $\bar{r} / \bar{a} = 1$. Regarding to the presence of surface energy effects, values of the vertical stress are lesser within the surface loading region $\bar{r} / \bar{a} \le 1.0$ and insignificantly higher in for $\bar{r} / \bar{a} > 1.0$. Moreover, the influence of surface energy effects exhibits significant role in the region relatively close to the surface. It is interesting to point out that all such behaviors are more apparent in the current model which integrates the out-of-plane contribution of the residual surface tension into the analysis.

Results for the normalized shear stress $4\pi(\bar{\lambda}+1)\bar{\sigma}_{rz} / \bar{p}_0$ are reported in Figure 4.10(a) for various depths. Behavior of the shear stress for all three models along the radial direction exhibit the similar trend. In particular, the shear stress vanishes at $\bar{r} = 0$ due to the symmetry, rapidly increases to reach its peak at the edge of the surface loading (i.e., $\bar{r} / \bar{a} = 1$), and promptly decreases after the peak. It is worth noting that, in the region very near the edge of surface loading, the surface energy effects especially in a model including the out-of-plane contribution of the residual surface tension significantly lower magnitude of the shear stress. As anticipated, the influence of surface stresses is quite large in a region near the surface and insignificant in a region far away from the surface.

In addition, variation along the radial direction of the normalized radial stress $4\pi(\bar{\lambda}+1)\bar{\sigma}_{rr} / \bar{p}_0$ and normalized hoop stress $4\pi(\bar{\lambda}+1)\bar{\sigma}_{\theta\theta} / \bar{p}_0$ are also presented for various depths in Figure 4.9(b) and 4.10(b), respectively. Again, results obtained from all three models possess the similar trend, i.e., starting with their maximum value and gradually decreasing as $\bar{r}$ increases. This observed behavior excludes the case of the radial stress at $\bar{z} = 1.0$ since such stress starts at a certain value, gradually reaches its peak, and gradually decays. However, the surface energy effects on these two stress components are similar to those on the vertical stress; i.e., lower stress within a region

under the surface loading and slightly higher stress in the region outside. In addition, strong influence of the surface stresses is observed in the region near the surface.

Through the proper normalization, solutions obtained by a model without the surface energy effects exhibit no size-dependency. However, this is not true for results predicted by models integrating the surface energy effects. The size-dependent behavior can be observed due to the presence of an intrinsic length scale associated with the presence of the surface stresses. In this study, the size-dependency of all normalized stresses is investigated by varying the radius of surface loading while maintaining the ratio $\bar{h}/\bar{a}$. Results are reported in Figures 4.11-4.14 for $\bar{h}/\bar{a}=3$. In particular, Figures 4.11(a), 4.12(a), 4.13(a) and 4.14(a) show the variation along the radial direction of non-zero stress components at $\bar{z}/\bar{a}=0.1$ for three different radius whereas Figures 4.11(b), 4.12(b), 4.13(b) and 4.14(b) present the relationship between normalized stress components and the radius of surface loading for three various depths and $\bar{r}/\bar{a}=0.5$.

Unlike the classical solutions, results obtained from the two models accounting for surface energy effects depend strongly on the normalized radius $\bar{a}$ for small $\bar{a}$ and such dependence gradually decreases as $\bar{a}$ increases. In particular, results predicted by the model taking the out-of-plane contribution of the residual surface tension exhibit much stronger size dependency than that excluding the out-of-plane term. In addition, this set of results confirms the necessity to include the surface energy effects when responses in a region very near the surface are of interest.

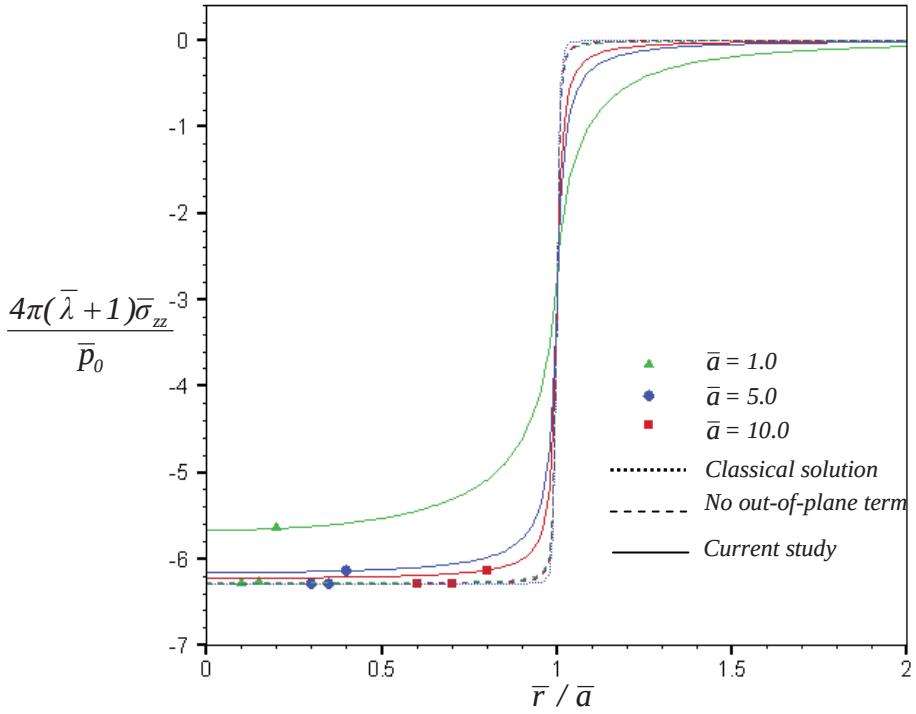

(a)

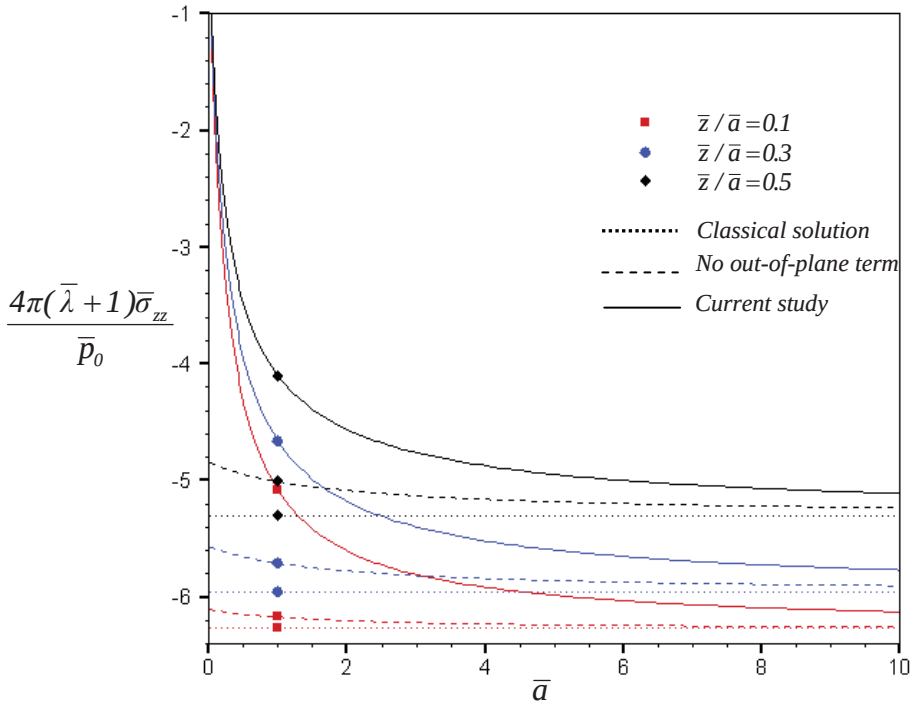

(b)

Figure 4.11 Normalized vertical stress of elastic layer under a uniformly distrubuted normal traction for $\bar{h}/\bar{a}=3$: (a) profile along radial direction and (b) at $\bar{r}/\bar{a}=0.5$

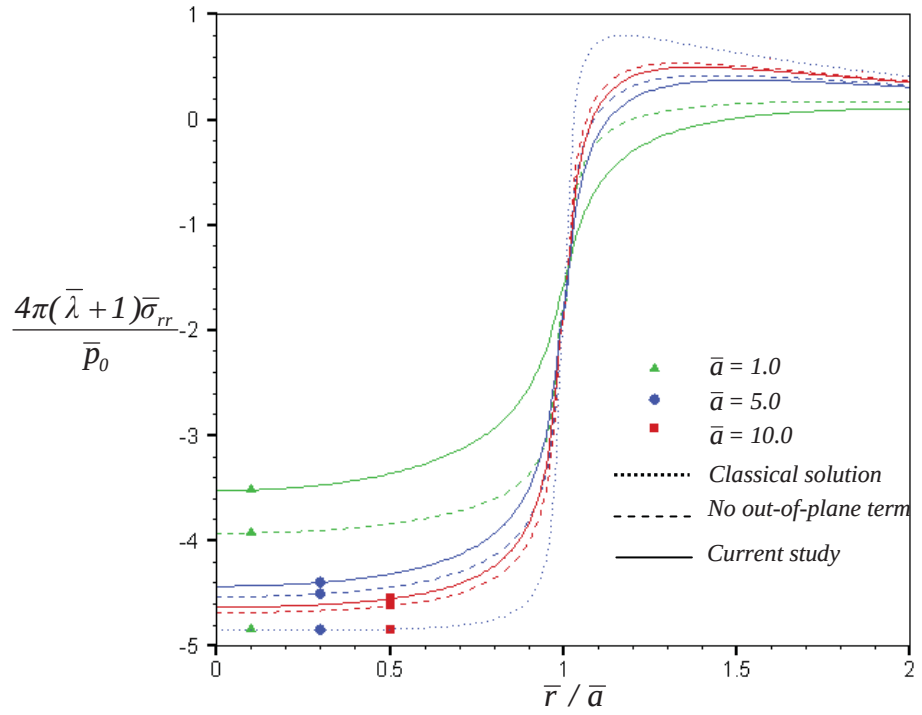

(a)

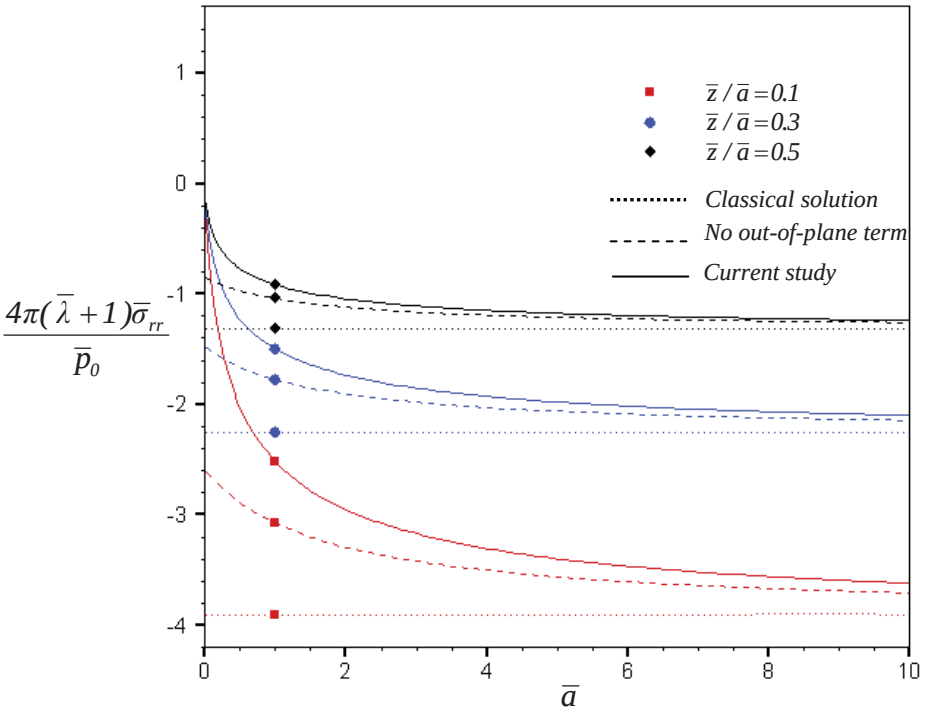

(b)

Figure 4.12 Normalized radial stress of an elastic layer under a uniformly distrubuted normal traction for $\bar{h}/\bar{a}=3$: (a) profile along radial direction and (b) at $\bar{r}/\bar{a}=0.5$

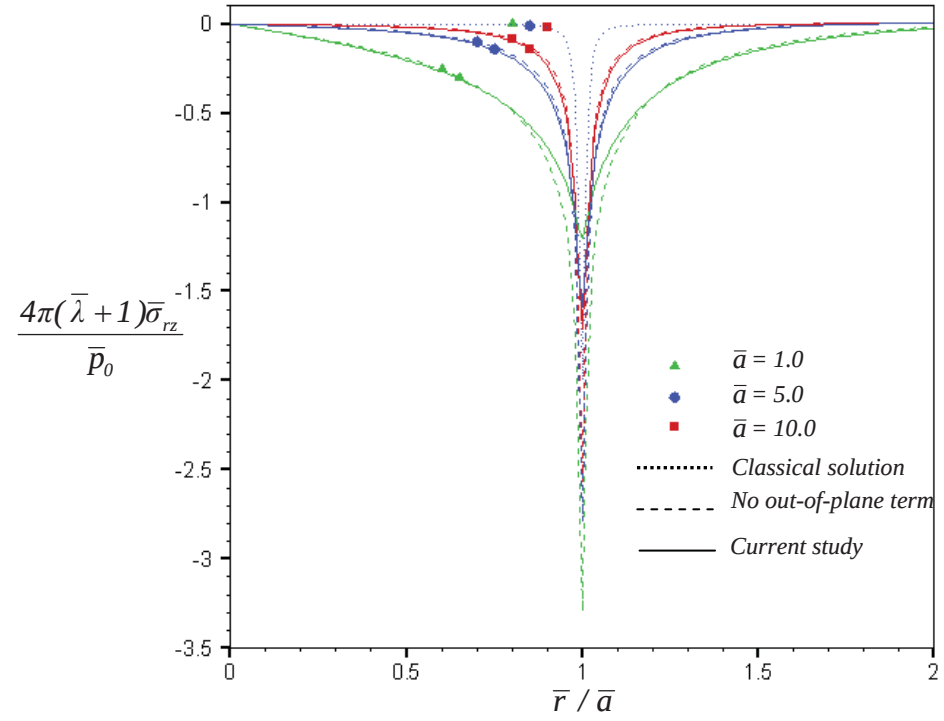

(a)

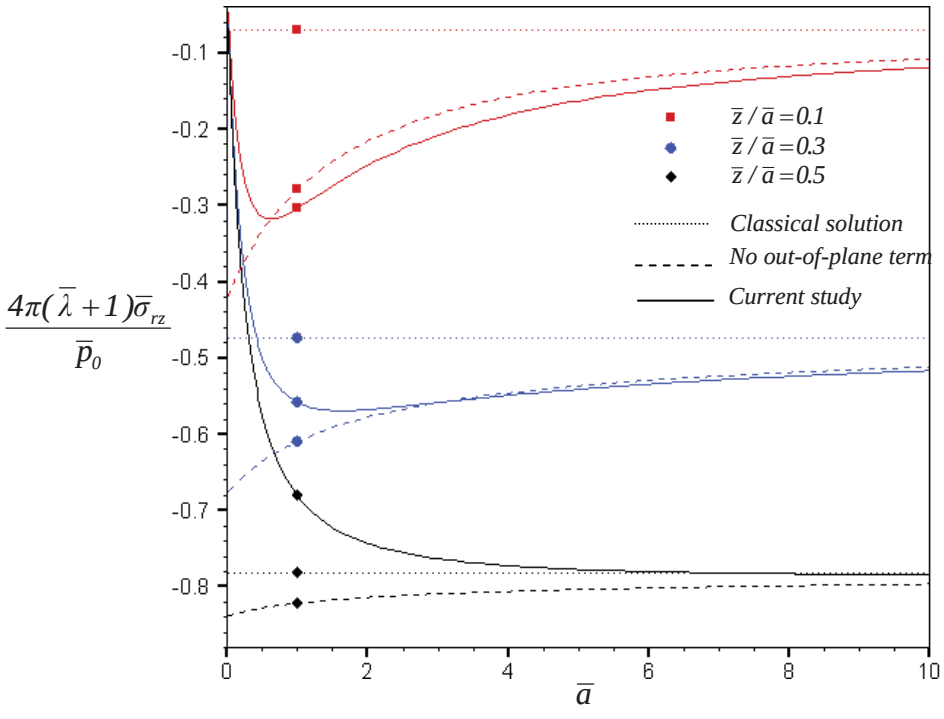

(b)

Figure 4.13 Normalized shear stress of an elastic layer under a uniformly distrubuted normal traction for $\bar{h}/\bar{a}=3$: (a) profile along radial direction and (b) at $\bar{r}/\bar{a}=0.5$

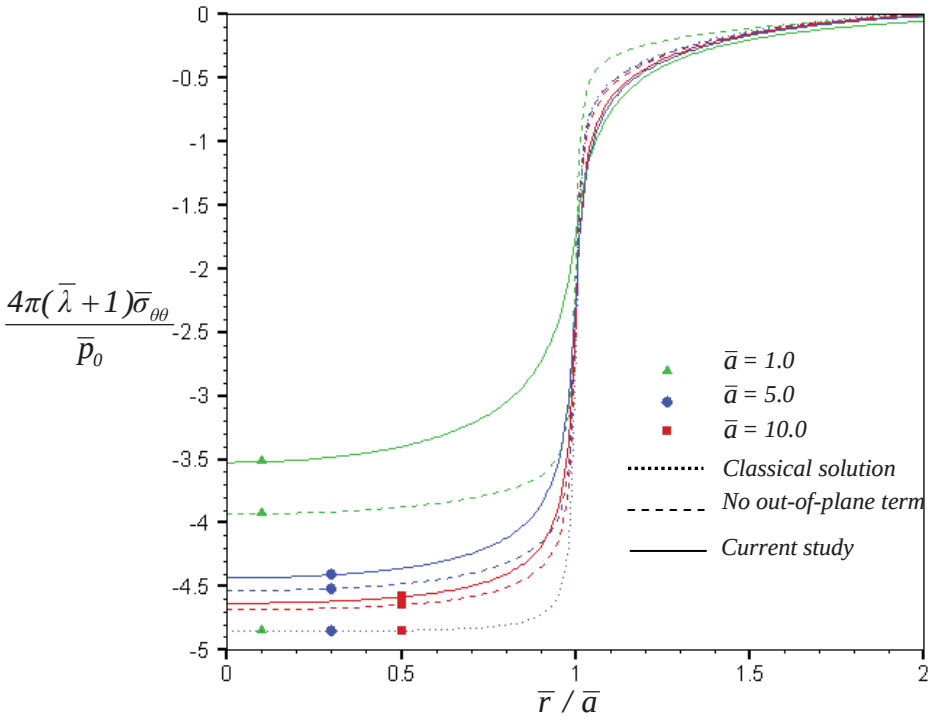

(a)

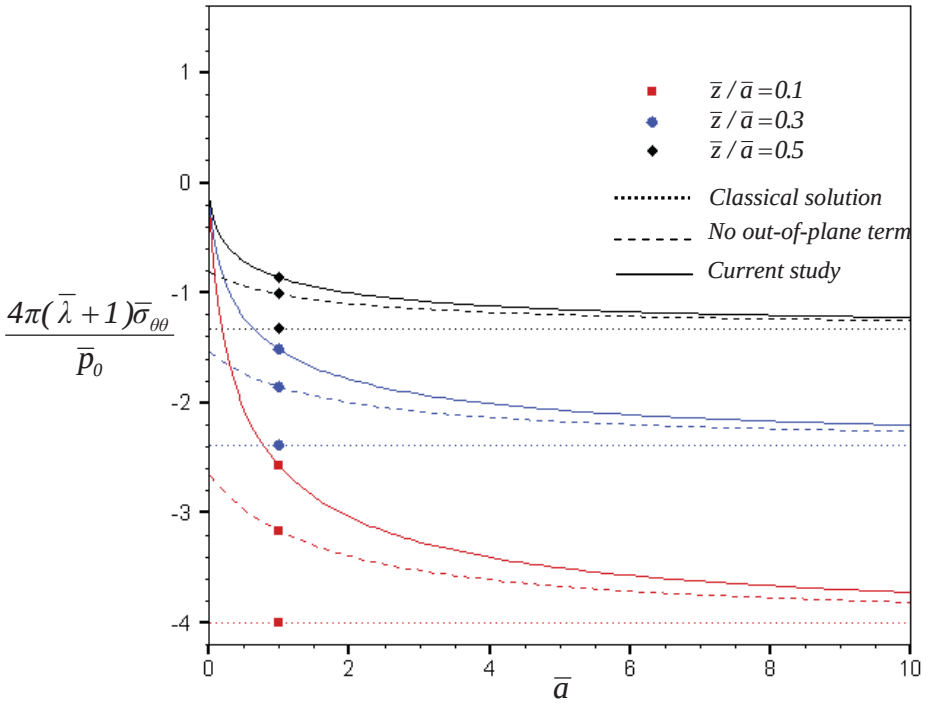

(b)

Figure 4.14 Normalized hoop stress of an elastic layer under a uniformly distrubuted normal traction for $\bar{h}/\bar{a}=3$: (a) profile along radial direction and (b) at $\bar{r}/\bar{a}=0.5$

4.2.2 Linearly Distributed Tangential Traction

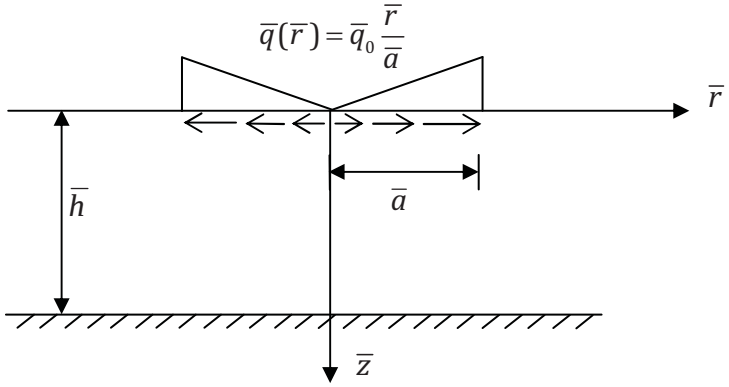

Figure 4.15 Three-dimensional, infinite, rigid-based, elastic layer subjected to a linearly distributed tangential traction

Consider an infinite, rigid-based elastic layer subjected to a linearly distributed tangential traction in a circular region of radius a as shown in Figure 4.15. This traction is normalized such that $\bar{q}(\bar{r}) = \bar{q}_0 \bar{r} / \bar{a}$ where $\bar{q}_0 = q_0 / \mu$, $\bar{a} = a / \Lambda$, and q_0 is the maximum traction at the edge of surface loading. Results for radial and vertical displacements for different layer thicknesses are shown in Figures 4.16(a) and 4.16(b), respectively. It is obvious from these results that presence of the surface energy effects significantly lowers the magnitude of the displacement. However, the out-of-plane contribution of residual surface tension has a strong influence only on the vertical displacement and becomes negligible for the radial displacement. Moreover, when varying the layer thickness, both radial and vertical displacements are higher as the layer thickness increases.

For stress components, results are obtained for $\bar{h} = 10$, $\bar{a} = 1$, and three different normalized depths (i.e., $\bar{z} = 0.25$, $\bar{z} = 0.5$, $\bar{z} = 1.0$). Profiles of the normalized vertical stresses $4\pi(\bar{\lambda} + 1)\bar{\sigma}_{zz} / \bar{q}_0$ and the normalized radial stresses $4\pi(\bar{\lambda} + 1)\bar{\sigma}_{rr} / \bar{q}_0$ along the radial direction are reported in Figure 4.17. At a small depth, the tensile stress is observed within a region of surface loading and it gradually changes to the compressive stress when passing the edge of a loading region. The vertical stress and radial stress profiles also show the strong influence of the surface energy effects for the region relatively near the surface. Moreover, the discrepancy of results predicted

by the two models with and without the out-of-plane contribution of the residual surface tension is more apparent for the vertical stress but insignificant for the radial stress.

Results for the normalized shear stress $4\pi(\bar{\lambda}+1)\bar{\sigma}_{rz}/\bar{q}_0$ are shown in Figure 4.18(a) for various depths. For this particular loading condition, the shear stress increases to reach its peak near the edge of loading region and then abruptly decreases to zero after passing the edge of loading region. Again, the influence of surface stresses on this shear stress component is more apparent for the region close to the surface.

From the profile of normalized hoop stress $4\pi(\bar{\lambda}+1)\bar{\sigma}_{\theta\theta}/\bar{q}_0$ shown in Figure 4.18(b), results obtained from the two models incorporating the surface energy effects are significantly different from the classical solution and such discrepancy increases when the depth decreases. It is worth noting that the contribution of the out-of-plane term is insignificant since the two models yield almost identical hoop stress.

To demonstrate the size-dependent behavior of a layer subjected to a linearly distributed tangential load, a scheme similar to that used to study a layer subjected to uniformly distributed normal traction is employed. The layer thickness and the radius of loading region are varied while their ratios are fixed (i.e., $\bar{h}/\bar{a}=3$). The variation along the radial direction of non-zero stress components at $\bar{z}/\bar{a}=0.1$ for three different radius are reported in Figures 4.19(a), 4.20(a), 4.21(a) and 4.22(a) whereas the relationship between normalized stress components and the radius of loading region for three various depths and $\bar{r}/\bar{a}=0.5$ are shown in Figures 4.19(b), 4.20(b), 4.21(b) and 4.22(b). Unlike the case of uniformly distributed normal load, the out-of-plane contribution of the residual surface tension has significant influences only on the vertical stress. However, solutions obtained from the two models accounting for the surface energy effects still show the size-dependency. As the radius $\bar{a}$ and the depth where the responses are determined decrease, the surface energy effects become more significant.

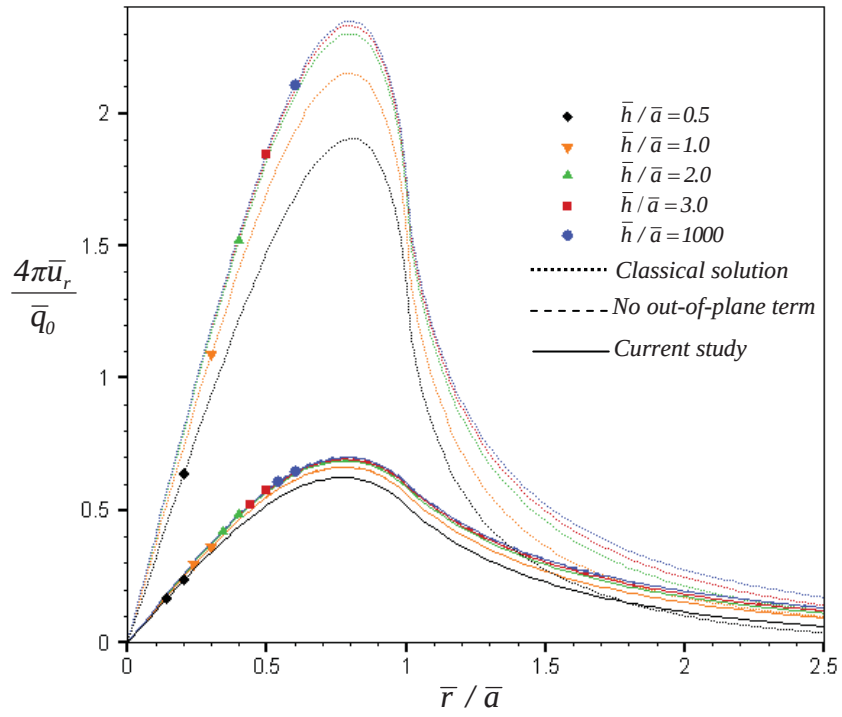

(a)

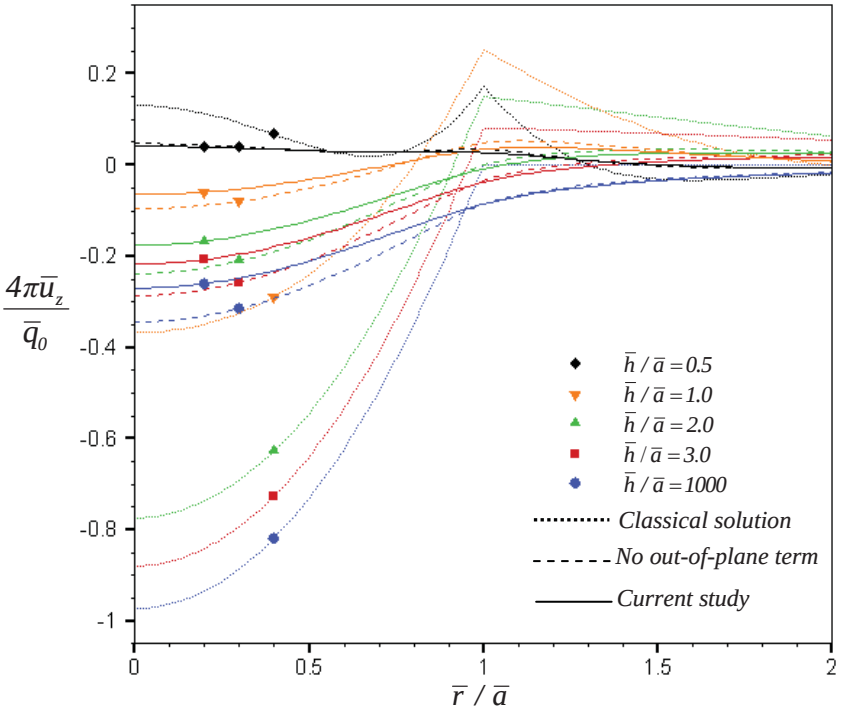

(b)

Figure 4.16 Normalized displacement profiles of an elastic layer under a linearly distrubuted tangential load: (a) radial displacement and (b) vertical displacement

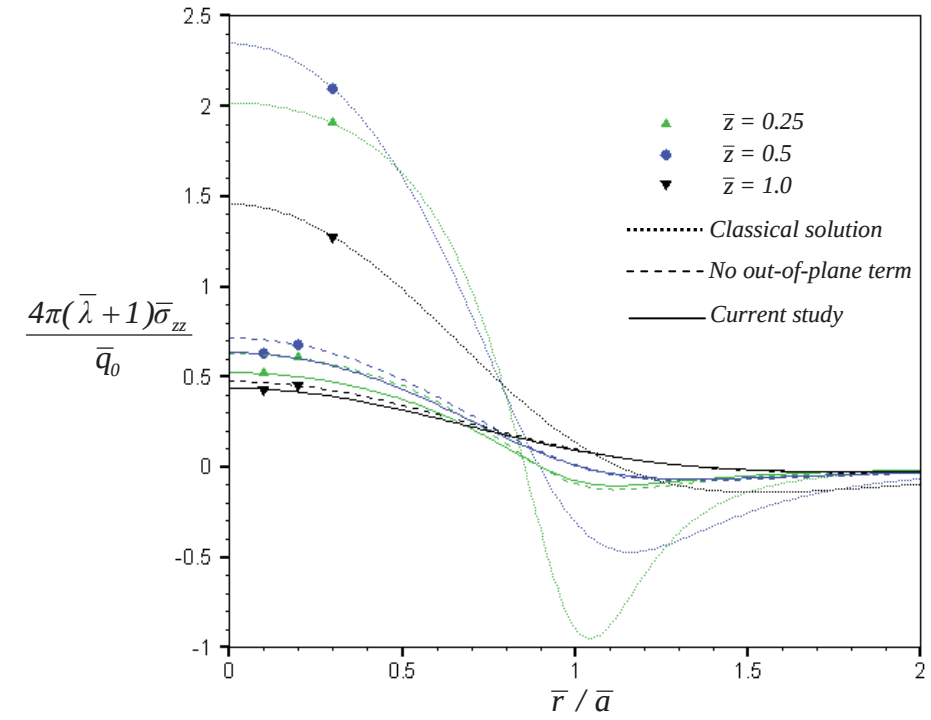

(a)

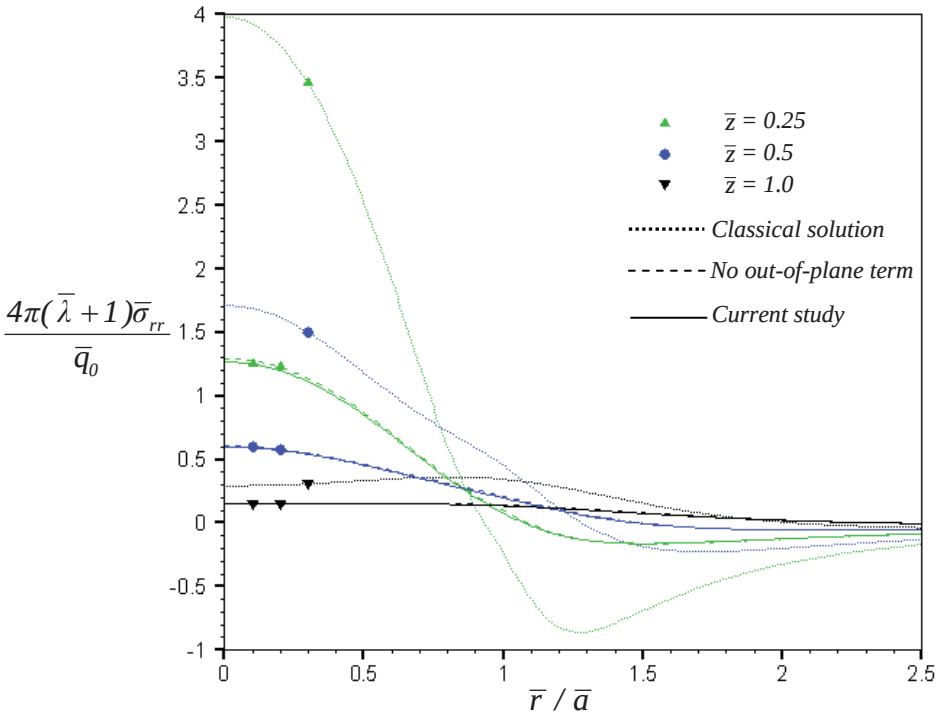

(b)

Figure 4.17 Normalized stress profiles of an elastic layer under a linearly distrubuted tangential load: (a) vertical stress and (b) radial stress

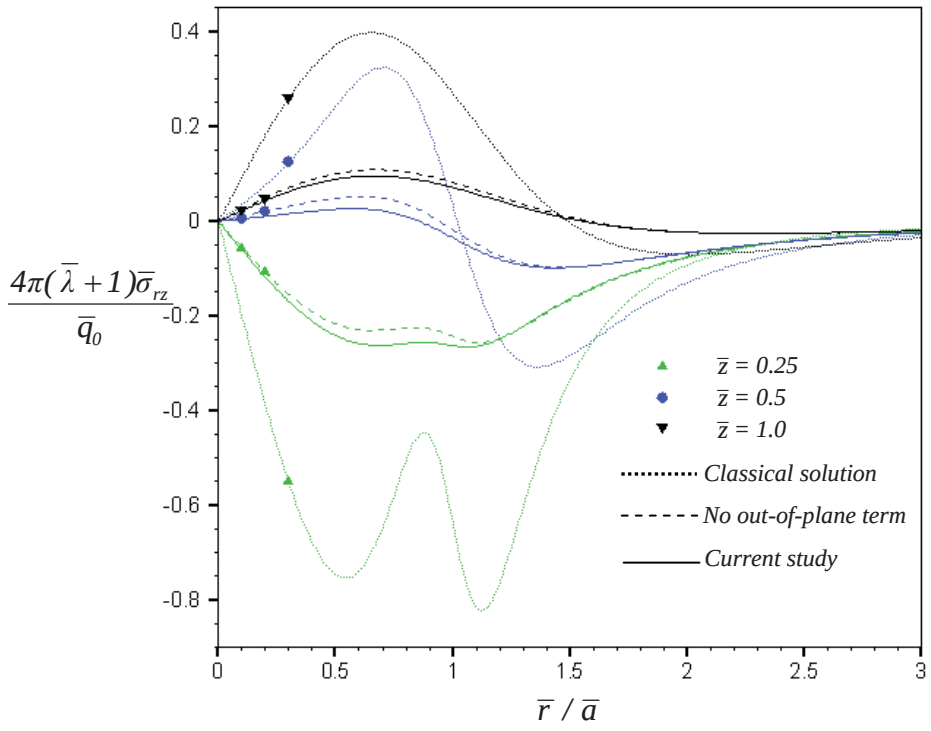

(a)

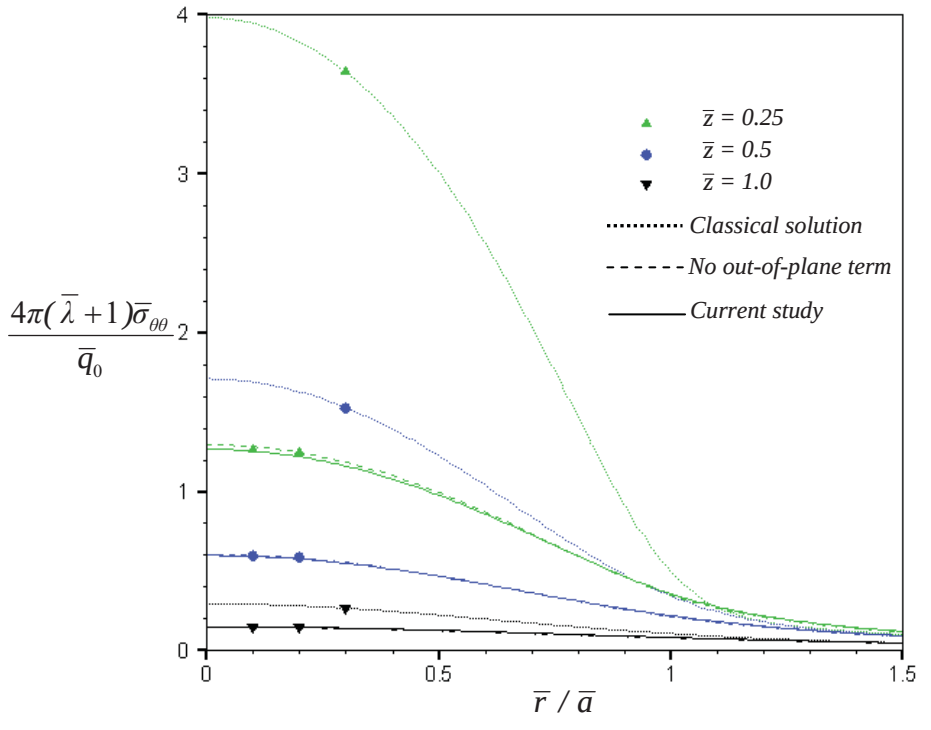

(b)

Figure 4.18 Normalized stress profiles of an elastic layer under a linearly distrubuted tangential load: (a) shear stress and (b) hoop stress

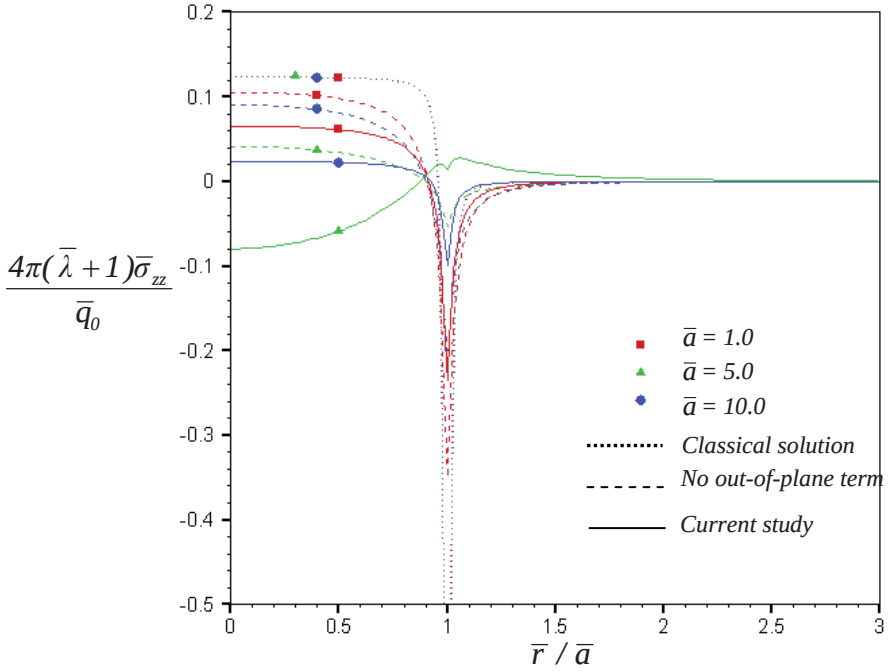

(a)

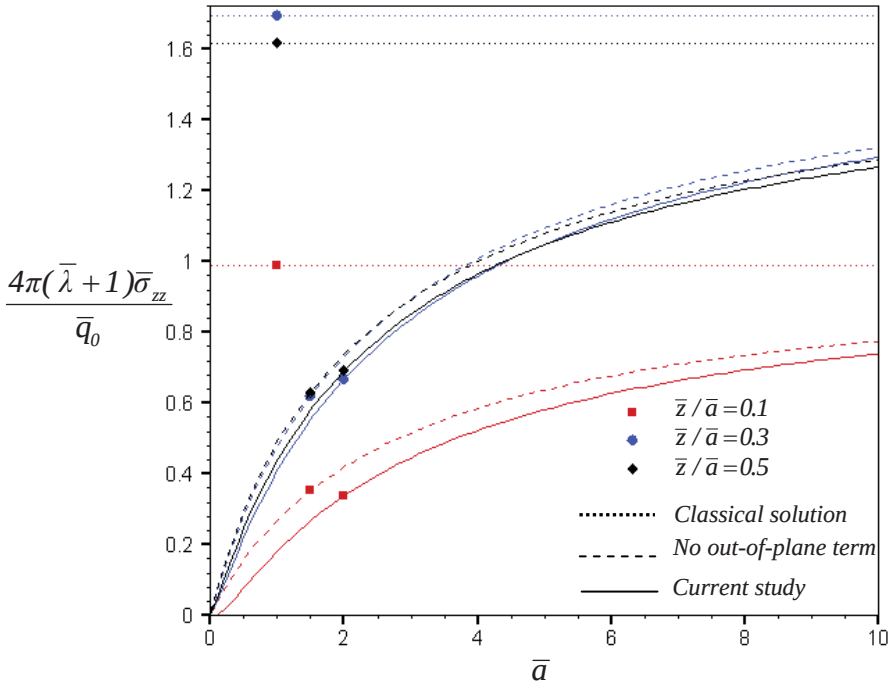

(b)

Figure 4.19 Normalized vertical stress of an elastic layer under a linearly distrubuted tangential load for $\bar{h}/\bar{a}=3$: (a) profile along radial direction and (b) at $\bar{r}/\bar{a}=0.5$

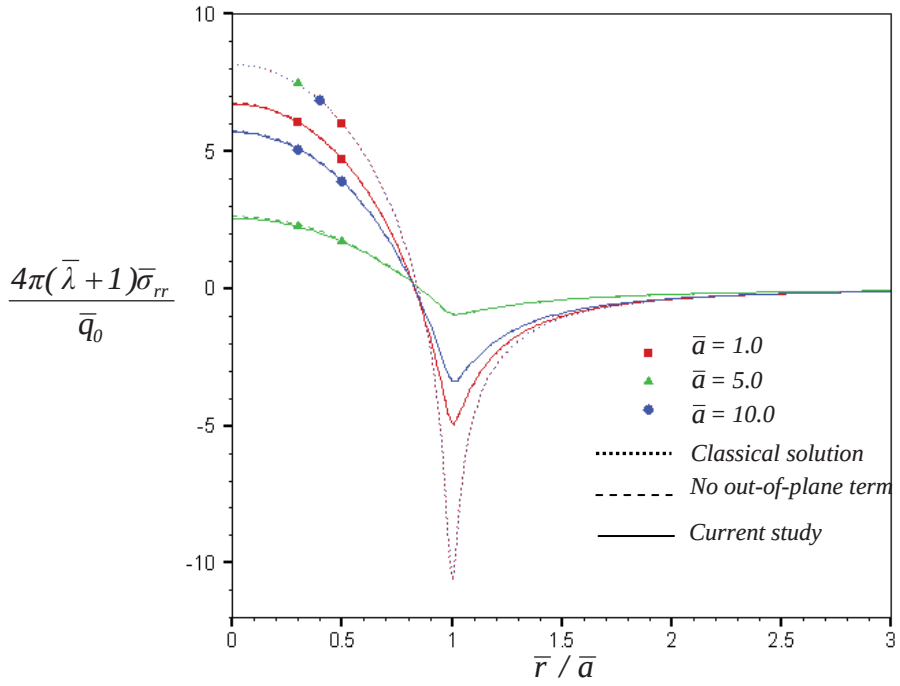

(a)

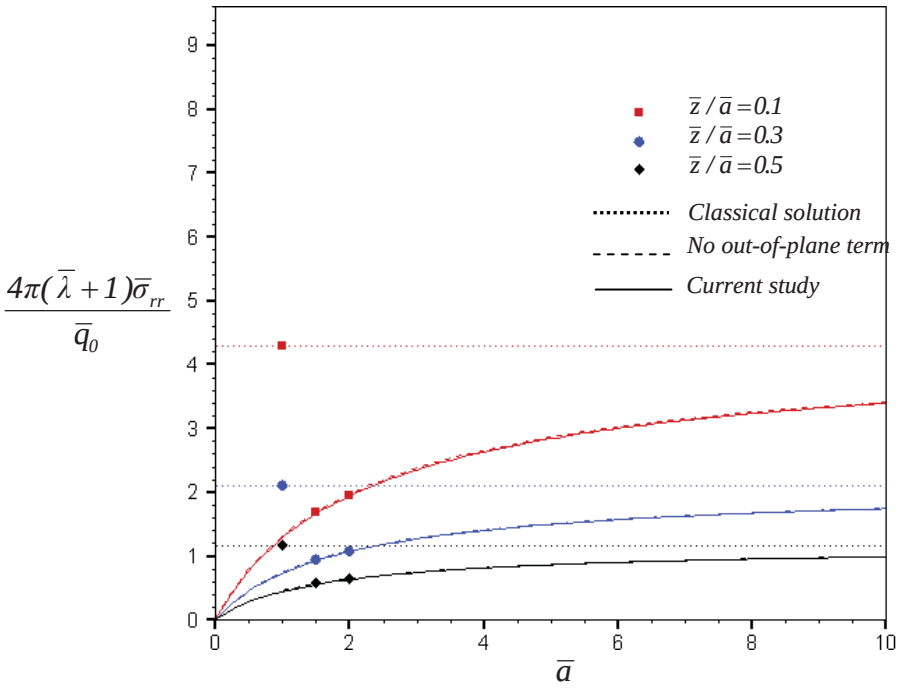

(b)

Figure 4.20 Normalized radial stress of an elastic layer under a linearly distrubuted tangential load for $\bar{h}/\bar{a}=3$: (a) profile along radial direction and (b) at $\bar{r}/\bar{a}=0.5$

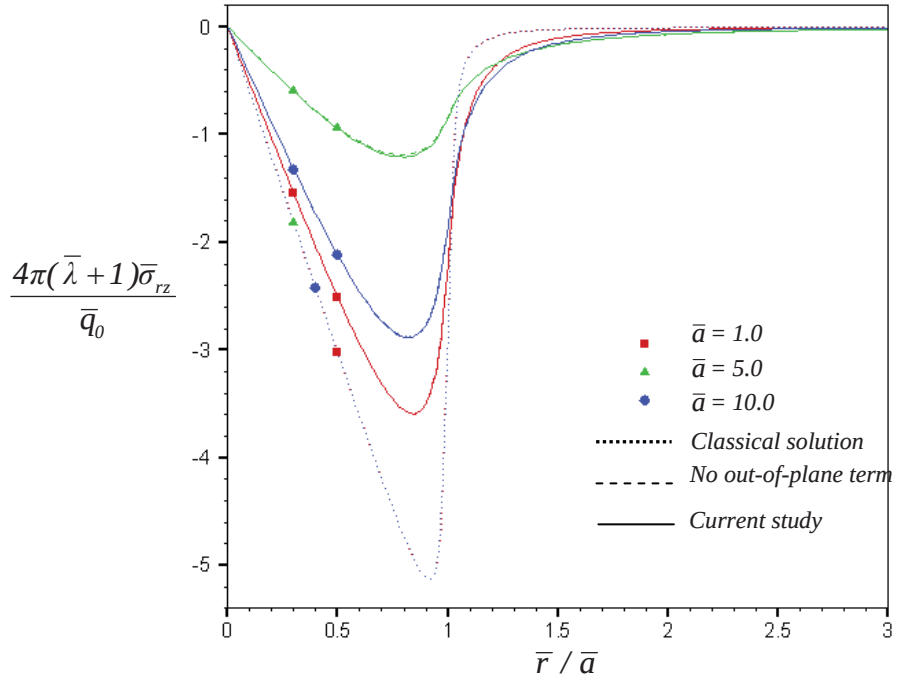

(a)

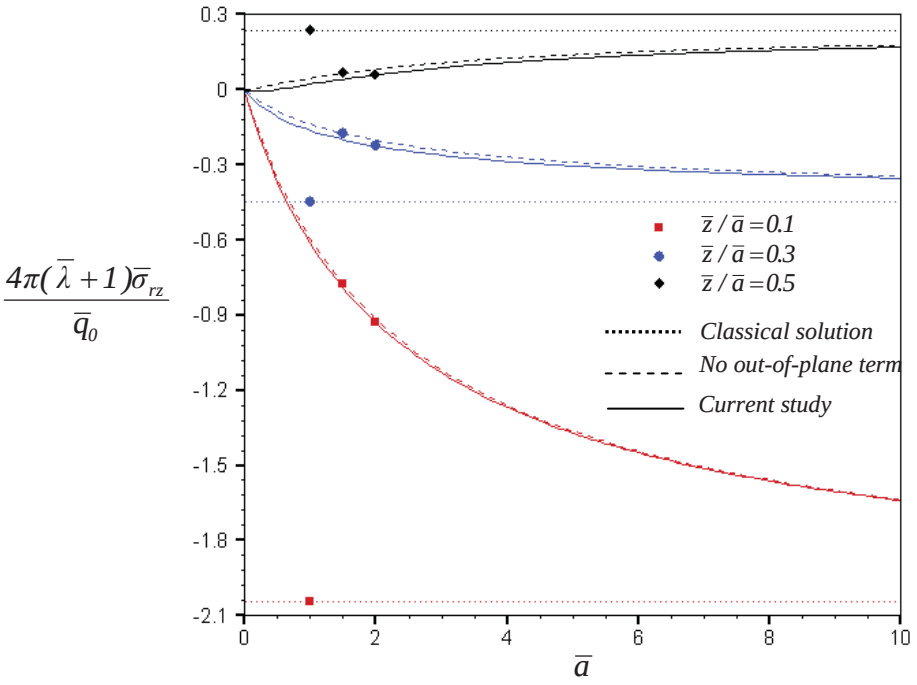

(b)

Figure 4.21 Normalized shear stress of an elastic layer under a linearly distrubuted tangential load for $\bar{h}/\bar{a}=3$: (a) profile along radial direction and (b) at $\bar{r}/\bar{a}=0.5$

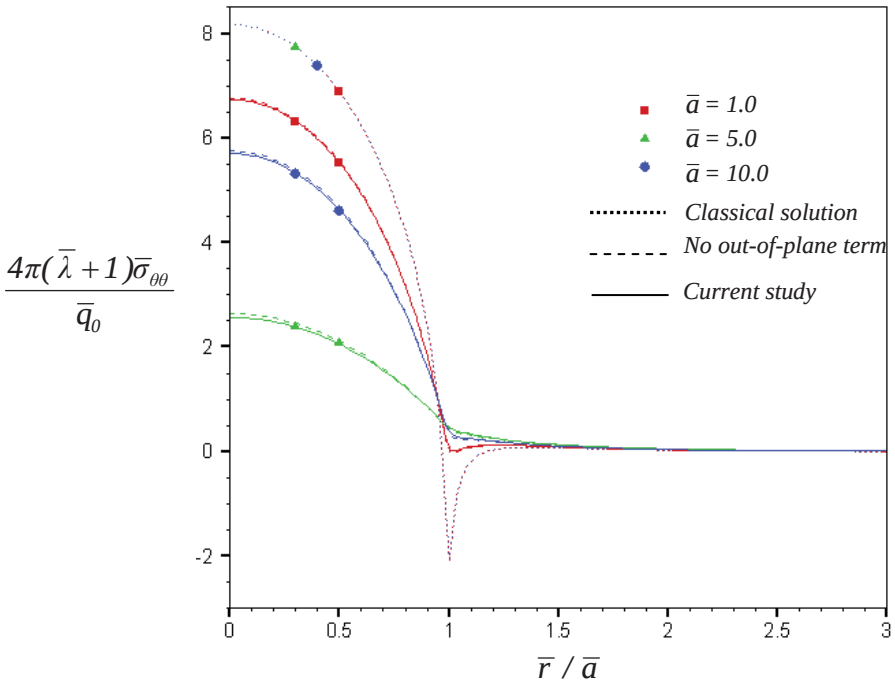

(a)

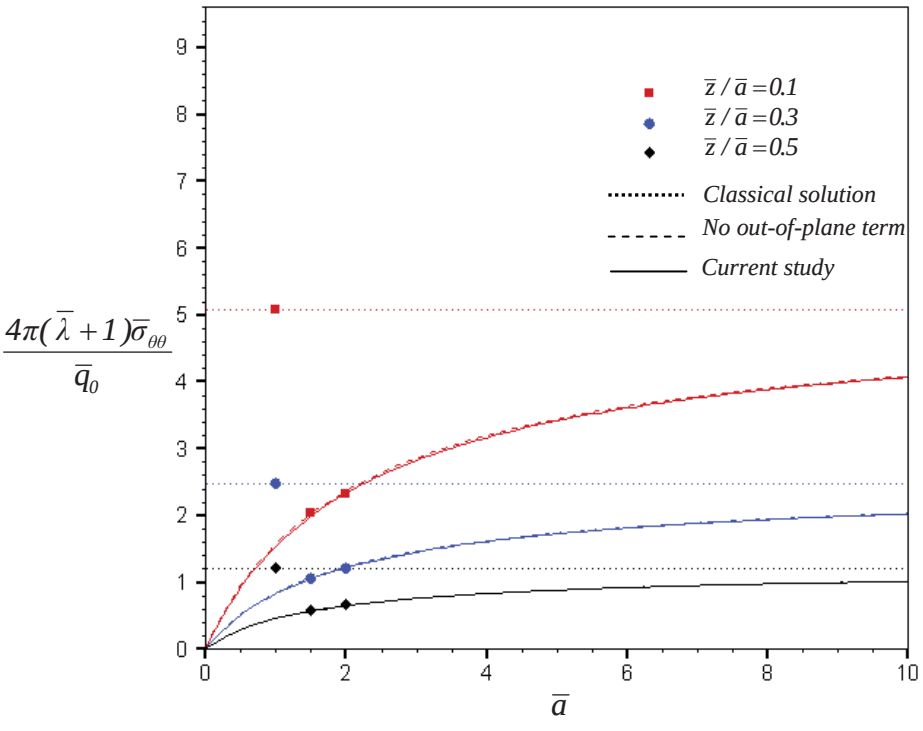

(b)

Figure 4.22 Normalized hoop stress of an elastic layer under a linearly distrubuted tangential load for $\bar{h} / \bar{a} = 3$: (a) profile along radial direction and (b) at $\bar{r} / \bar{a} = 0.5$

4.3 Fundamental Solutions

Since the formulation has been established for arbitrary axisymmetric surface loading, general results can be further specialized to construct certain useful fundamental solutions. For instance, solutions associated with a layer subjected to a normal concentrated load at the origin, a normal ring load at any radius a and a tangential ring load at any radius a can readily be obtained. These fundamental solutions constitute the basis for solving other related boundary value problems such as nano-indentation problems.

4.3.1 Layer under Normal Concentrated Load

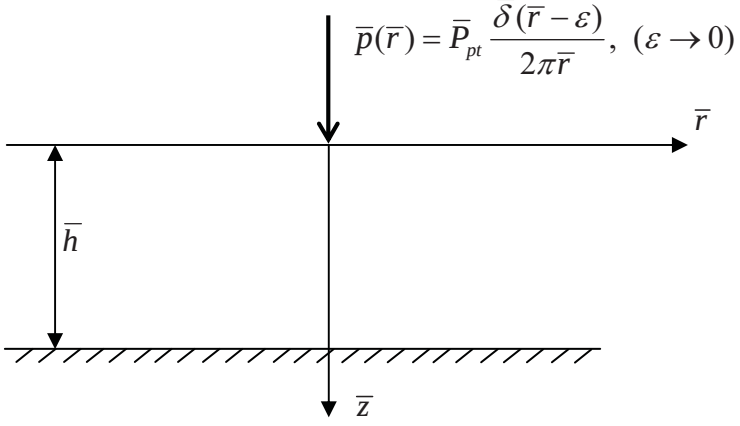

Figure 4.23 Three-dimensional, infinite, rigid-based, elastic layer subjected to a normal concentrated load

Consider a three-dimensional, infinite, rigid-based, elastic layer subjected to a normal concentrated load P_{pt} as shown in figure 4.23. The concentrated load P_{pt} is normalized such that $\bar{P}_{pt} = P_{pt} / \mu\Lambda^2$. Profiles of the normalized radial displacement $2\pi\bar{h}\bar{E}\bar{u}_r / \bar{P}_{pt}$ and the normalized vertical displacement $2\pi\bar{h}\bar{E}\bar{u}_r / \bar{P}_{pt}$ at the surface obtained by three different models are reported for four different layer thicknesses ($\bar{h} = 0.5, \bar{h} = 1.0$, $\bar{h} = 2.0$, and $\bar{h} = 3.0$) in Figure 4.24(a) and 4.24(b), respectively. It is found that the normalized radial displacement is singular at $\bar{r} = 0$ except the solution obtained from a model accounting for the out-of-plane contribution of residual surface

stress. On the other hand, results of the normalized vertical displacement tend to be infinite under the concentrated load for all cases and reduce rapidly when $\bar{r}$ increases. In addition, the similar behavior is observed for all layer thicknesses examined and the magnitude of the displacement is higher as the layer thickness increases.

In order to clearly demonstrate the influence of surface energy effects on the stress field, the layer thickness is chosen to be sufficiently large (i.e., $\bar{h}=10$). Numerical results of all normalized non-zero stress components are reported along the radial direction for various depths in Figures 4.25-4.26. Clearly, the normalized vertical stress $4\pi\bar{h}^2(\bar{\lambda}+1)\bar{\sigma}_{zz}/\bar{P}_{pt}$ reaches its peak at $\bar{r}=0$ and then decrease monotonically to zero as $\bar{r}$ increases. The normalized radial stress $4\pi\bar{h}^2(\bar{\lambda}+1)\bar{\sigma}_{rr}/\bar{P}_{pt}$ decreases from a positive value to a negative value for small $\bar{r}$ and, after it attains its maximum negative value, it magnitude gradually reduces to zero for the region far away from the concentrated load. Due to the symmetry, the normalized shear stress vanishes at $\bar{r}=0$ and it rapidly increases to reach its peak and then gradually decreases to zero for a large $\bar{r}$. It is obvious that presence of surface energy effects generally reduce the magnitude of all stress components in comparison with the classical solution except the normalized hoop stress whose values predicted by the model accounting for surface energy effects but without the out-of-plane contribution of the residual surface stress are much larger than those obtained from the classical model.

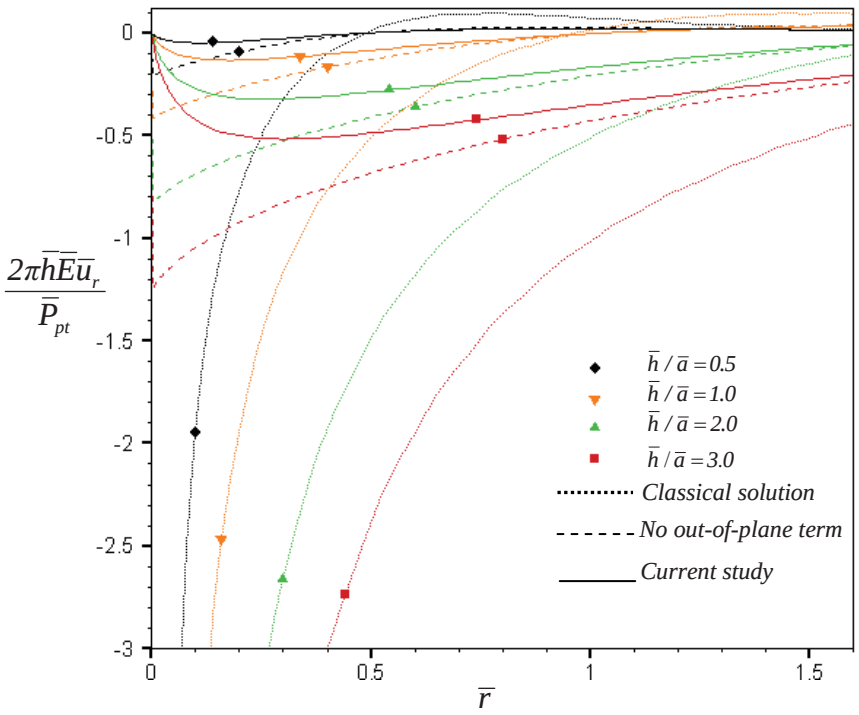

(a)

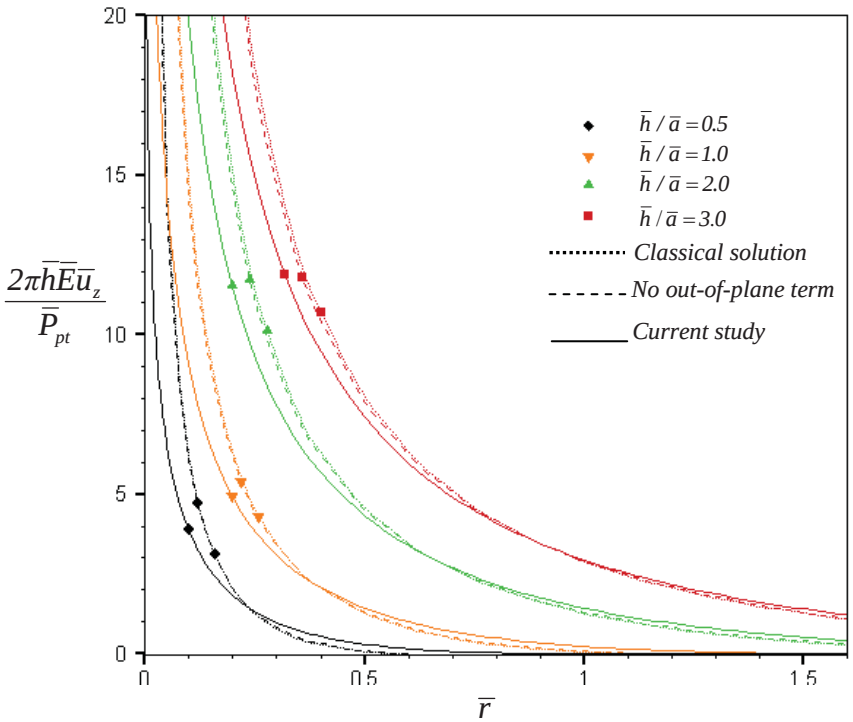

(b)

Figure 4.24 Normalized displacement profiles of an elastic layer under a normal concentrated load: (a) radial displacement and (b) vertical displacement

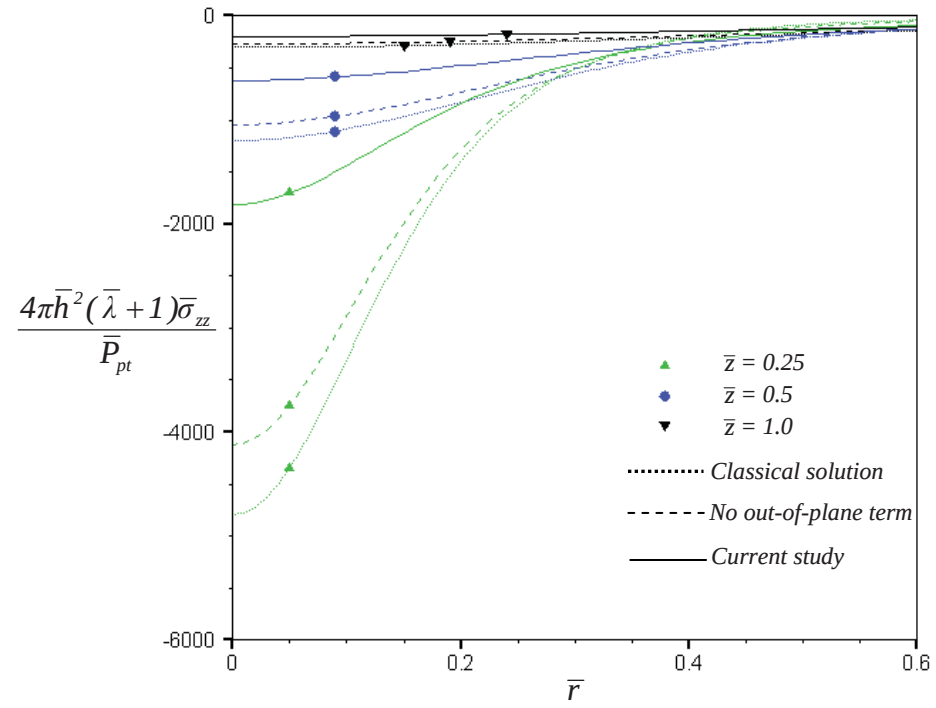

(a)

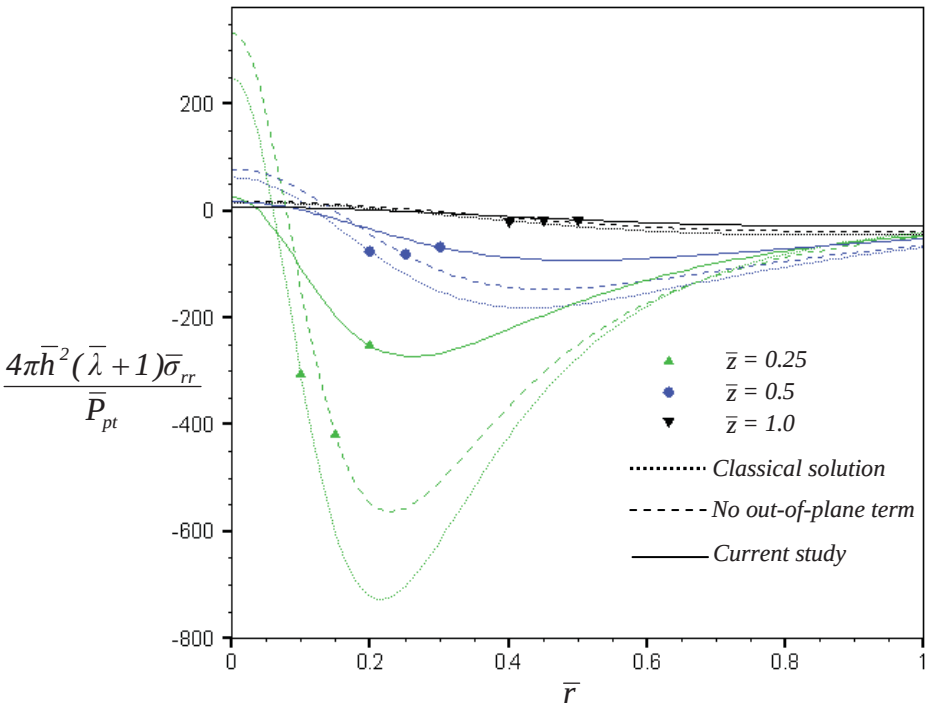

(b)

Figure 4.25 Normalized stress profiles of an elastic layer under a normal concentrated load: (a) vertical stress and (b) radial stress

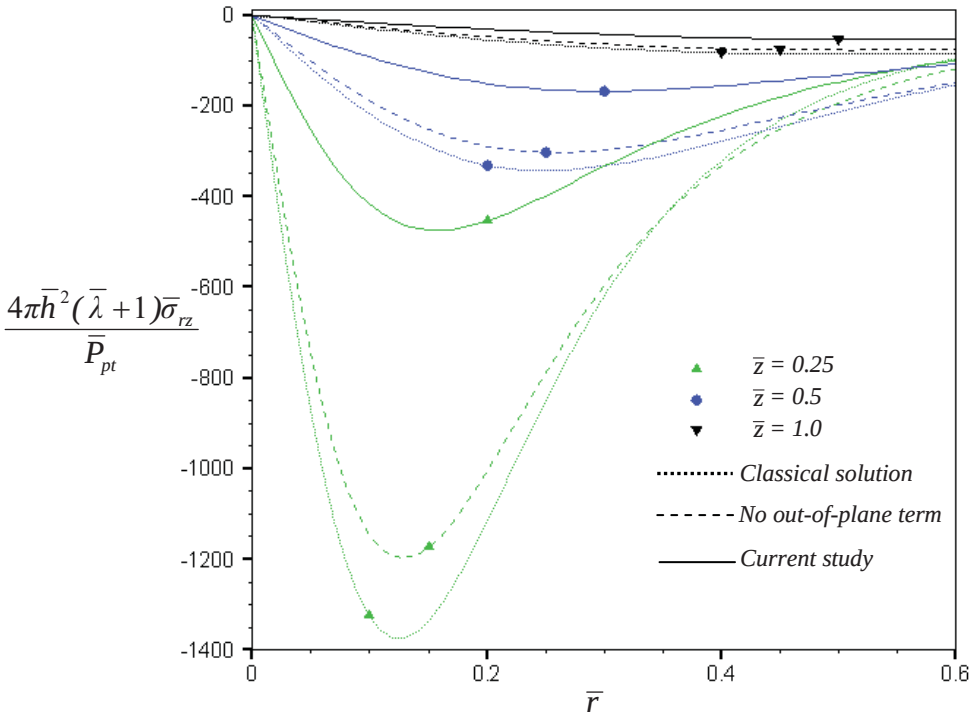

(a)

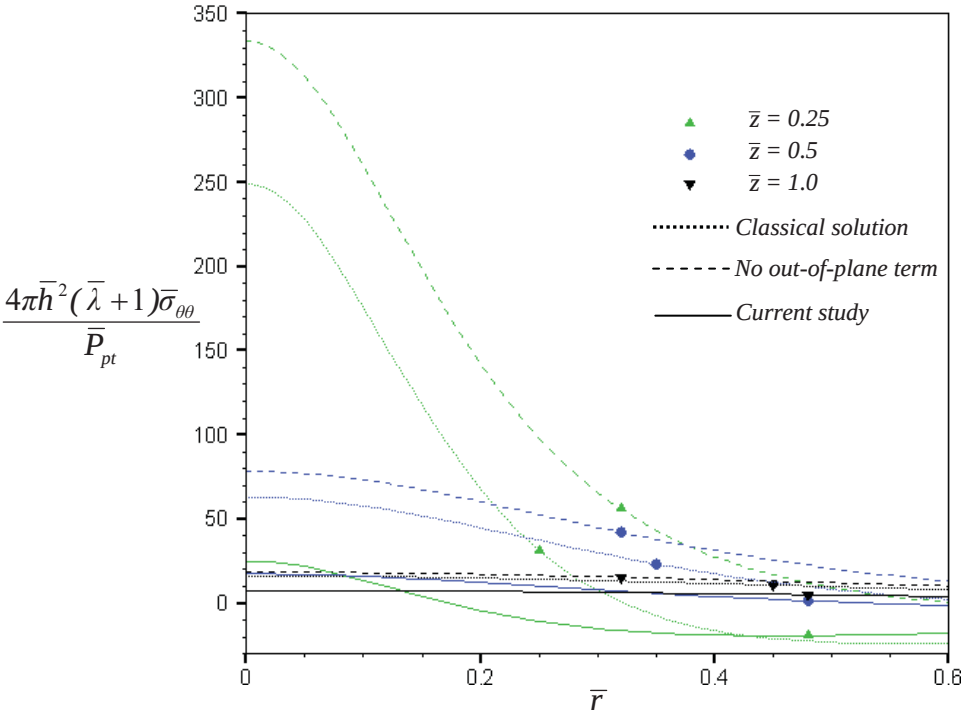

(b)

Figure 4.26 Normalized stress profiles of an elastic layer under a normal concentrated load: (a) shear stress and (b) hoop stress

4.3.2 Layer under Normal Ring Load

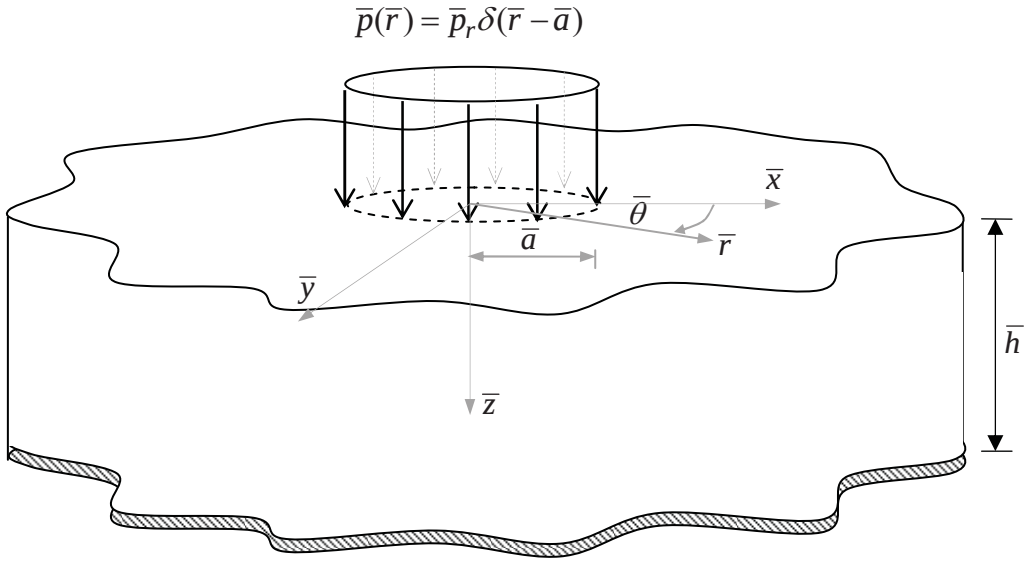

Figure 4.27 Three-dimensional, infinite, rigid-based, elastic layer subjected to a normal ring load

Consider a three-dimensional, infinite, rigid-based, elastic layer subjected to a normal ring load p_r at the radius a as shown in figure 4.27. The ring load and the radius a are normalized such that $\bar{p}_r = p_r / \mu\Lambda$ and $\bar{a} = a/\Lambda$. Results for the normalized radial displacement $4\pi\bar{h}\bar{u}_r / \bar{p}_r$ and the normalized vertical displacement $4\pi\bar{h}\bar{u}_z / \bar{p}_r$ at the surface are plotted along the radial direction as shown in Figure 4.28 for four different thicknesses ($\bar{h} = 0.5, \bar{h} = 1.0, \bar{h} = 2.0,$ and $\bar{h} = 3.0$) and $\bar{a} = 1$. It is apparent from obtained results that the radial displacement for the classical case exhibit rapid variation at location of the applied ring load while those obtained from the other two models are finite and smooth and significantly different from the classical solution. In the contrary, the vertical displacements predicted by the classical model and a model accounting for the surface energy effect but without the out-of-plane term are slightly different and singular at the location of applied load whereas that obtained from a model incorporating the out-of-plane term is finite and significantly different from the other two solutions.

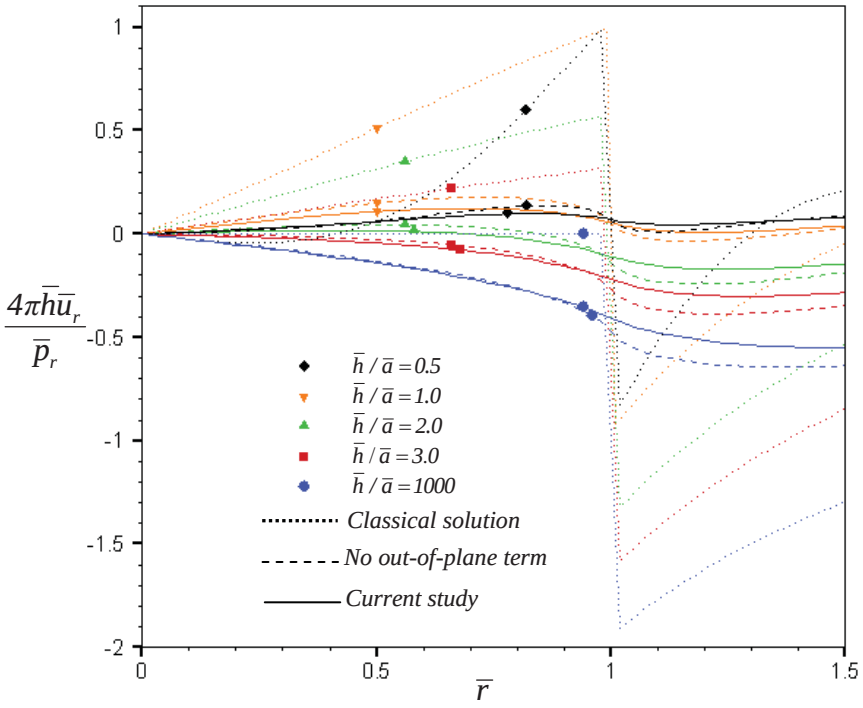

(a)

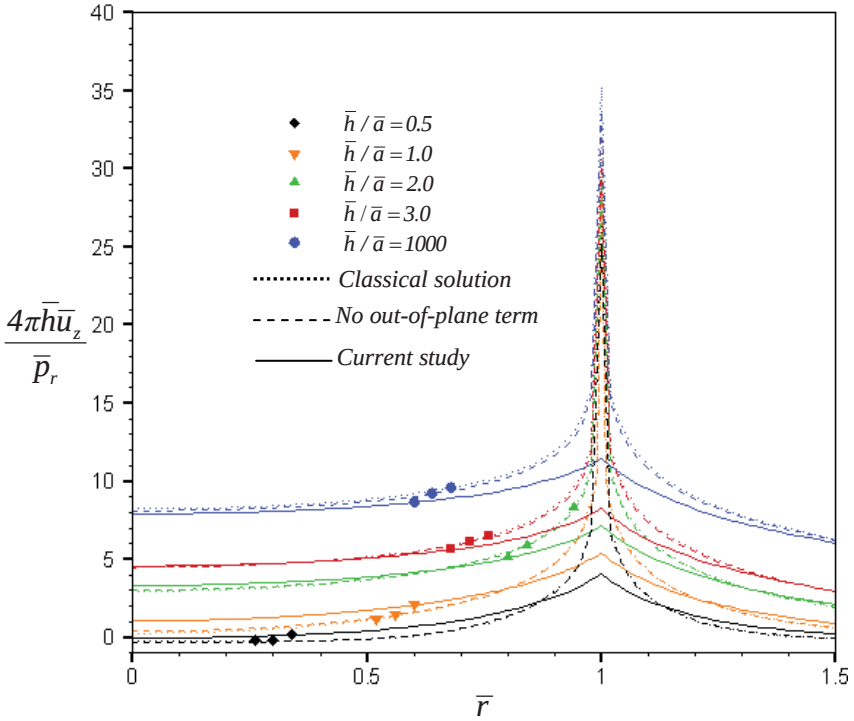

(b)

Figure 4.28 Normalized displacement profiles of an elastic layer under a normal ring load: (a) radial displacement and (b) vertical displacement

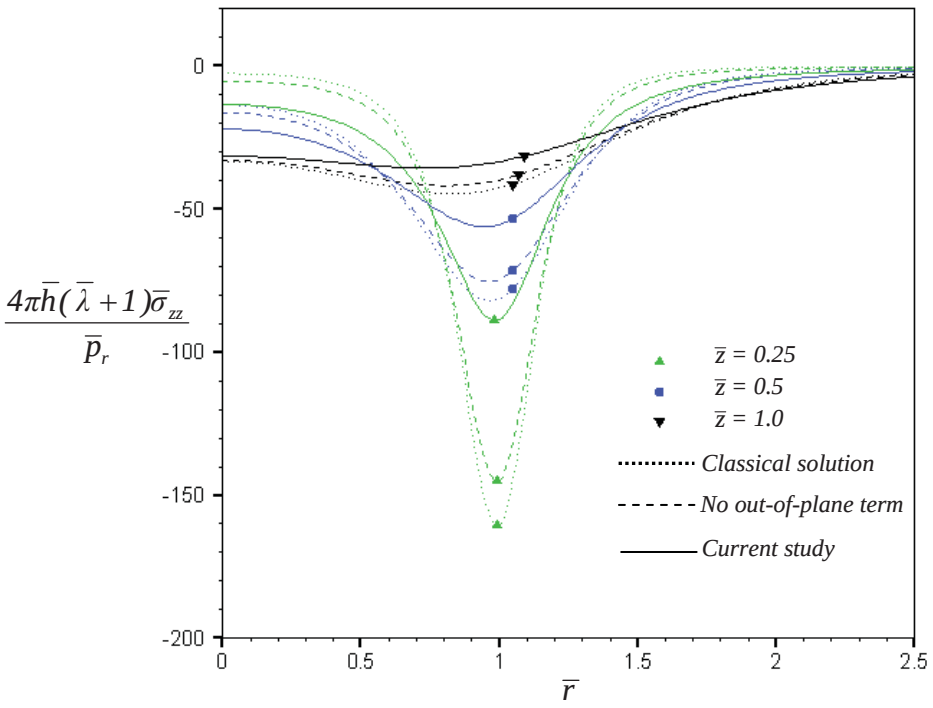

(a)

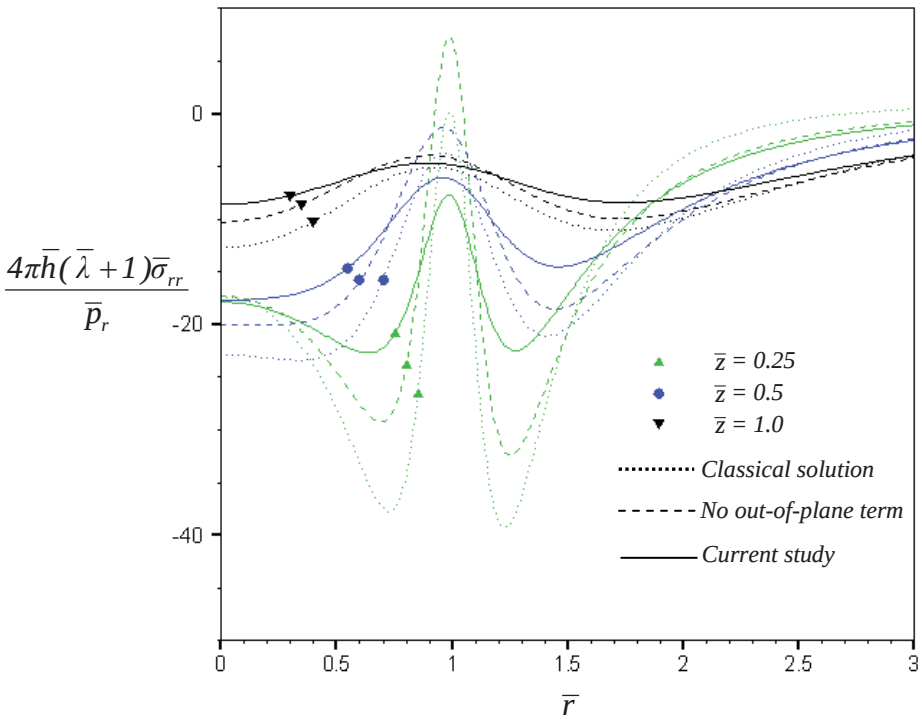

(b)

Figure 4.29 Normalized stress profiles of an elastic layer under a normal ring load: (a) vertical stress and (b) radial stress

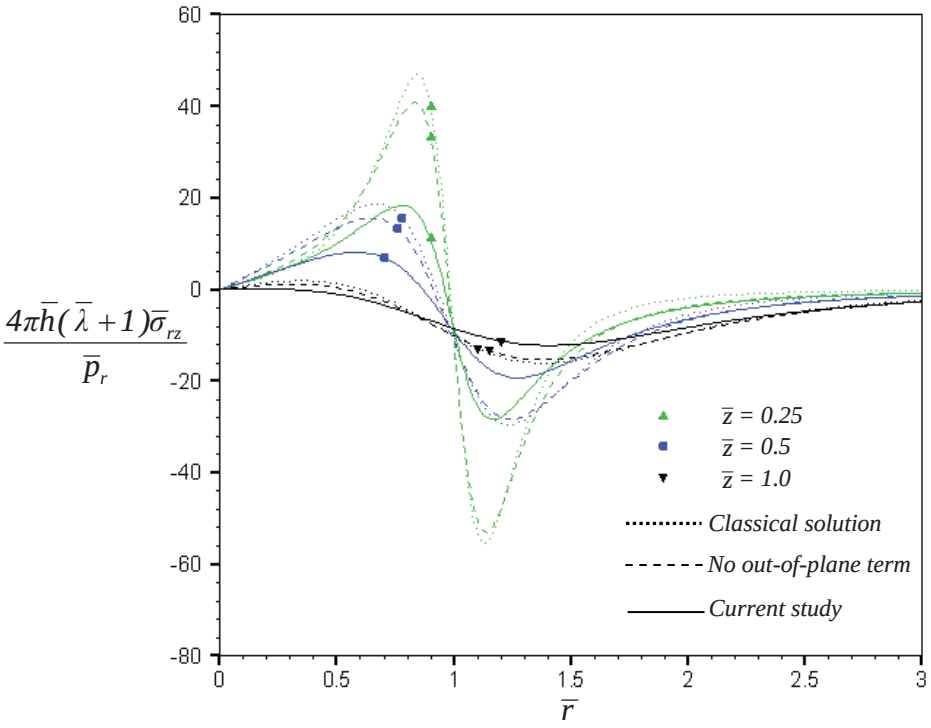

(a)

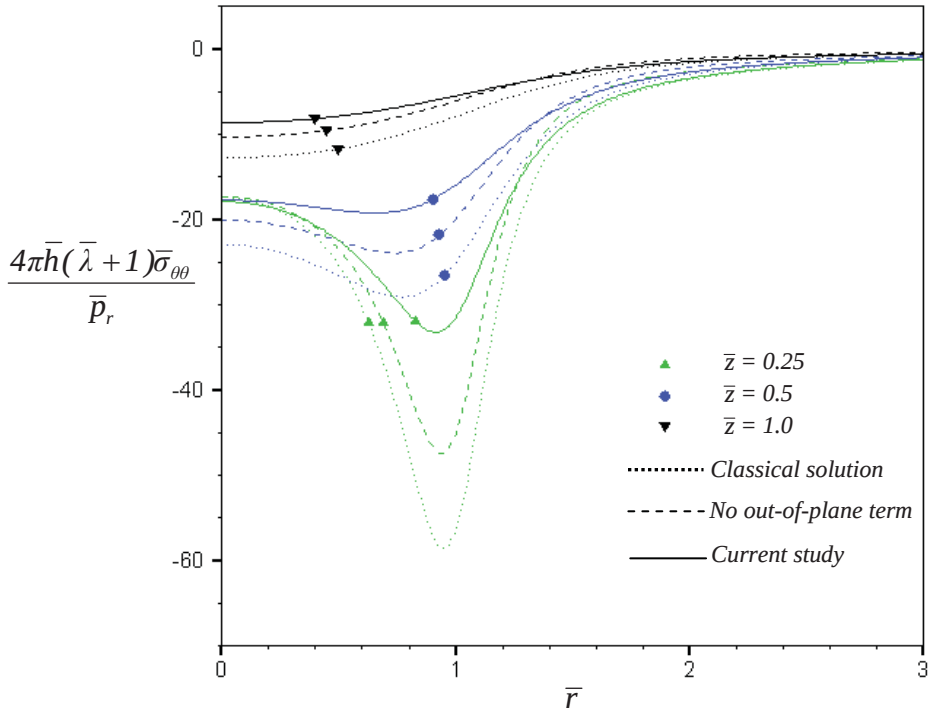

(b)

Figure 4.30 Normalized stress profiles of an elastic layer under a normal ring load: (a) shear stress and (b) hoop stress

Results for stress within the bulk obtained from all three models are also reported for various depths and $\bar{h}=10$ in Figures 4.29-4.30. Similar to the previous observation, the influence of the surface stresses on the stress field within the bulk is more significant when the location where the responses are determined is relatively close to the surface.

4.3.3 Layer under Tangential Ring Load

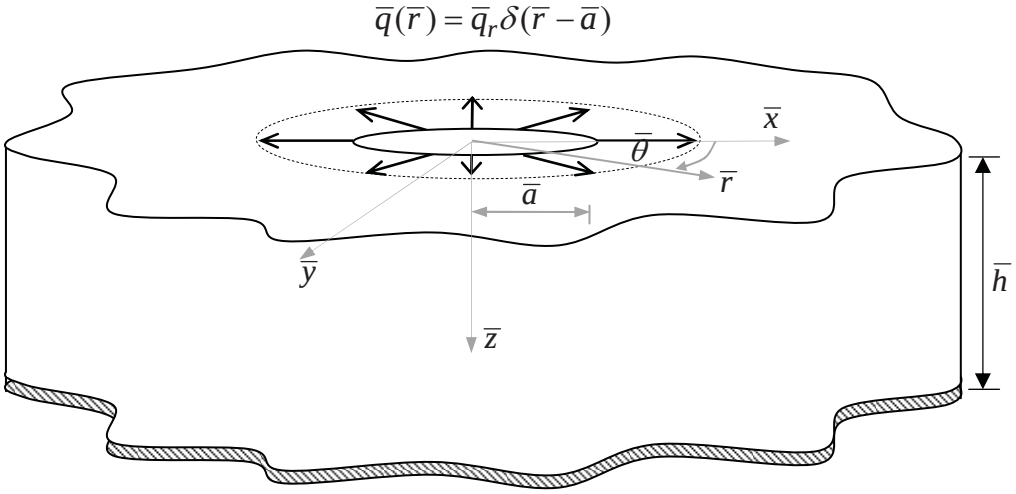

Figure 4.31 Three-dimensional, infinite, rigid-based, elastic layer subjected to a tangential ring load

Consider a three-dimensional, infinite, rigid-based, elastic layer subjected to a unit tangential ring load q_r at the radius a as shown in figure 4.31. The ring load and the radius are normalized such that $\bar{q}_r = q_r / \mu\Lambda$ and $\bar{a}=a/\Lambda$. Results for the normalized radial displacement $4\pi\bar{h}\bar{u}_r / \bar{q}_r$ and the normalized vertical displacement $4\pi\bar{h}\bar{u}_z / \bar{q}_r$ at the surface are plotted along the radial direction as shown in Figures 4.32(a) and 4.32(b) for four different thicknesses ($\bar{h}=0.5, \bar{h}=1.0, \bar{h}=2.0$, and $\bar{h}=3.0$) and $\bar{a}=1$. For this particular loading condition, both the radial and vertical displacements obtained from the classical model are singular at the location of the applied ring load whereas those obtained from the two models accounting for the surface energy effects are finite everywhere. While results obtained from the two

models exhibit huge discrepancy from the classical solution, the contribution of out-of-plane term is insignificant especially for the radial displacement.

Figures 4.33-4.34 demonstrate profiles of normalized stress components for a layer subjected to a tangential ring load for the layer thickness $\bar{h}=10$ and various depths. It is obviously seen that the presence of the surface energy effects reduces the magnitude of the stresses especially in the region closed to the surface. Moreover, for the normalized vertical stress and normalized shear stress, such behavior is more evident when the out-of-plane contribution of the residual surface stress is taken into account.

4.3.4 Applications of Fundamental Solutions

Results obtained above for three special loading conditions can be employed to construct Green functions useful for various boundary value problems. To demonstrate their vast applications, let us consider a three-dimensional, infinite, rigid-based, elastic layer subjected to any axisymmetric normal traction $p(r)$ and tangential traction $q(r)$. Once solutions of all field quantities due to both unit normal and unit tangential ring loads are determined, they can be utilized along with a method of superposition to obtain integral relations for both the displacement and stress on the surface and within the bulk due to the tractions $p(r)$ and $q(r)$. For instance, the radial and tangential displacements at any distance r^* on the surface are given by

$$u_r(r^*)=\int_0^\infty U_r^N(r^*,r)p(r)dr+\int_0^\infty U_r^T(r^*,r)q(r)dr \tag{4.1}$$

$$u_z(r^*)=\int_0^\infty U_z^N(r^*,r)p(r)dr+\int_0^\infty U_z^T(r^*,r)q(r)dr \tag{4.2}$$

where $U_r^N(r^*,r)$ and $U_z^N(r^*,r)$ are radial and tangential displacements at any distance r^* on the surface due to a unit normal ring load applied to the layer at the radius r and $U_r^T(r^*,r)$ and $U_z^T(r^*,r)$ are radial and tangential displacements at any distance r^* on the surface due to a unit tangential ring load applied to the layer at the radius r. Other

field quantities at any point (r^*, z^*) within the bulk, denoted generically by $R(r^*,z^*)$, can also be obtained in a similar fashion as

$$R(r^*,z^*)=\int_0^\infty R^N(r^*,z^*,r)p(r)dr+\int_0^\infty R^T(r^*,z^*,r)q(r)dr \tag{4.3}$$

where, again, $R^N(r^*,z^*,r)$ and $R^T(r^*,z^*,r)$ are responses at any point (r^*, z^*) within the bulk due to a unit normal ring load and unit tangential ring load applied to the layer at the radius r, respectively. Clearly, for a problem where the surface tractions $p(r)$ and $q(r)$ are fully prescribed, the integral relations (4.1)-(4.3) can be directly employed to determine all field quantities.

For nano-indentation problems, the tractions $p(r)$ and $q(r)$ under the indentor are unknown a priori and they must be determined before the integral relation (4.3) can be used. For a special case of axisymmetric, rigid, frictionless nano-indentation problems, the tangential traction $q(r)$ vanishes and vertical displacement under the indentor is fully prescribed via its known profile v^p and the prescribed indentation depth d. The integral relation (4.2) for any r^* under the indentor becomes

$$u_z(r^*)=\int_0^a U_z^N(r^*,r)p(r)dr=d+v^p(r^*) \quad , \quad r^*\le a \tag{4.4}$$

where a denotes the contact radius. The integral equation (4.4) can be solved to obtain the unknown contact pressure $p(r)$. Once $p(r)$ is determined, all other field quantities can readily be obtained from the integral relation (4.3).

For axisymmetric, rigid, fully bonded nano-indentation problems, the radial displacement under the indentor identically vanishes and the vertical displacement under the indentor is fully prescribed via its known profile v^p and the prescribed indentation depth d. The integral relations (4.1) and (4.2) for any r^* under the indentor becomes

$$u_r(r^*)=\int_0^a U_r^N(r^*,r)p(r)dr+\int_0^a U_r^T(r^*,r)q(r)dr=0 \quad , \quad r^*\le a \tag{4.5}$$

$$u_z(r^*) = \int_0^a U_z^N(r^*, r)p(r)dr + \int_0^a U_z^T(r^*, r)q(r)dr = d + v^p(r^*) \quad , \quad r^* \le a \tag{4.6}$$

The two integral equations (4.5)-(4.6) are sufficient for solving the unknown tractions $p(r)$ and $q(r)$. Once those tractions are obtained, all other field quantities can be computed from the integral relation (4.3).

For axisymmetric, rigid, rough nano-indentation problems, the tangential traction $q(r)$ can be related to the normal traction $p(r)$ via an appropriate friction model and, again, the vertical displacement under the indentor is fully prescribed via its known profile v^p and the prescribed indentation depth d. The integral relation (4.2) for any r^* under the indentor becomes

$$u_z(r^*) = \int_0^a U_z^N(r^*, r)p(r)dr + \int_0^a U_z^T(r^*, r)f(p(r))dr = d + v^p(r^*) \quad , \quad r^* \le a \tag{4.7}$$

where a function f denotes the relation between p and q. The integral equation (4.7) can be employed to solve for the unknown normal traction $p(r)$. Once $p(r)$ is determined, the tangential traction can readily be obtained and all other field quantities are computed from the integral relation (4.3).

By following the same strategy, solutions of all field quantities due to a unit normal concentrated load applied to the surface of a layer can be utilized as Green functions to establish integral relations for field quantities due to arbitrary normal traction on the surface. In addition, the integral relation for the vertical displacement on the surface can be employed to form the integral equation governed the unknown pressure under the rigid, frictionless indentor of arbitrary profiles.

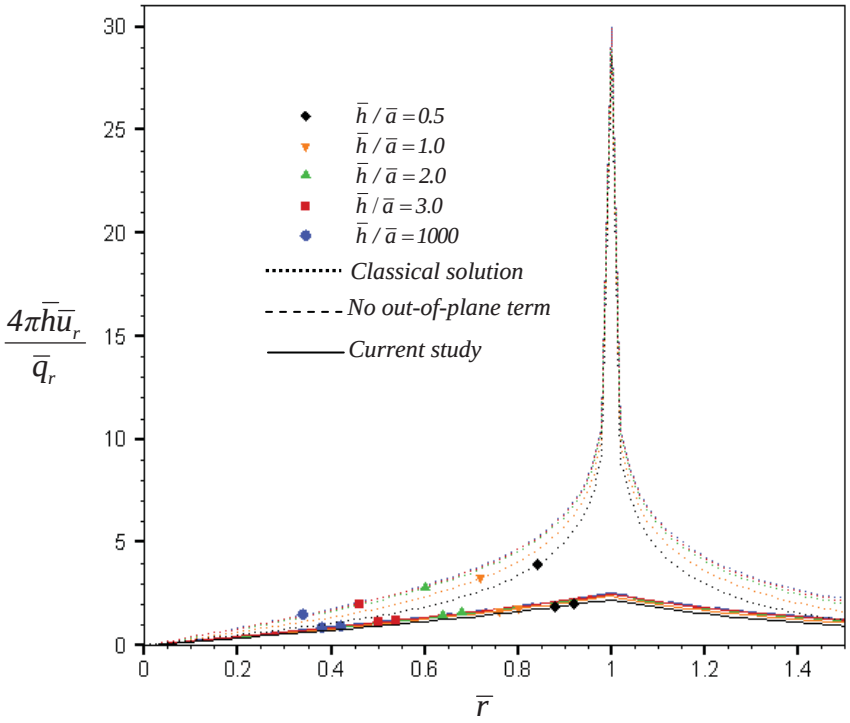

(a)

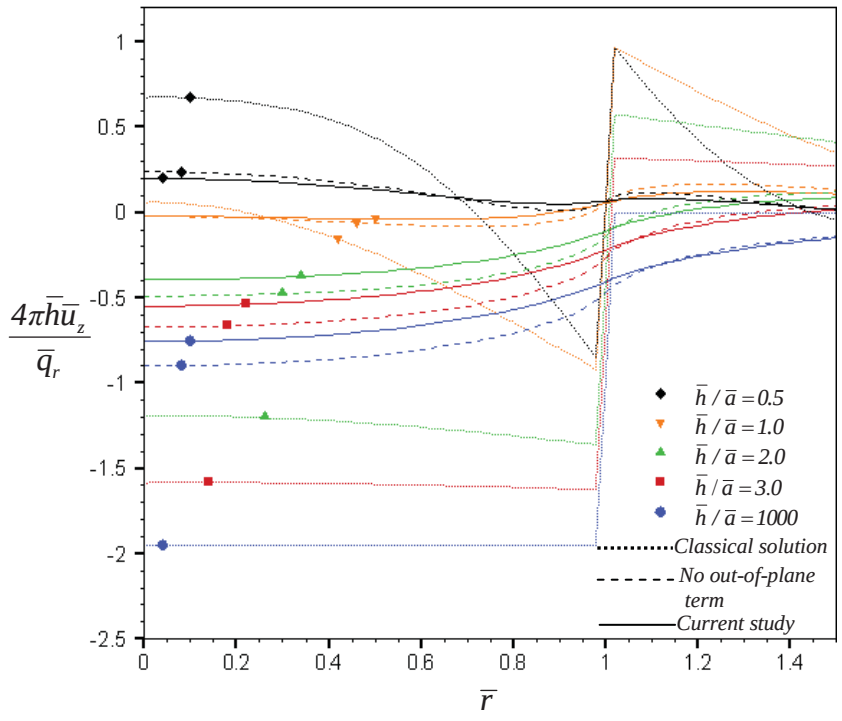

(b)

Figure 4.32 Normalized displacement profiles of an elastic layer under tangential ring load: (a) radial displacement and (b) vertical displacement

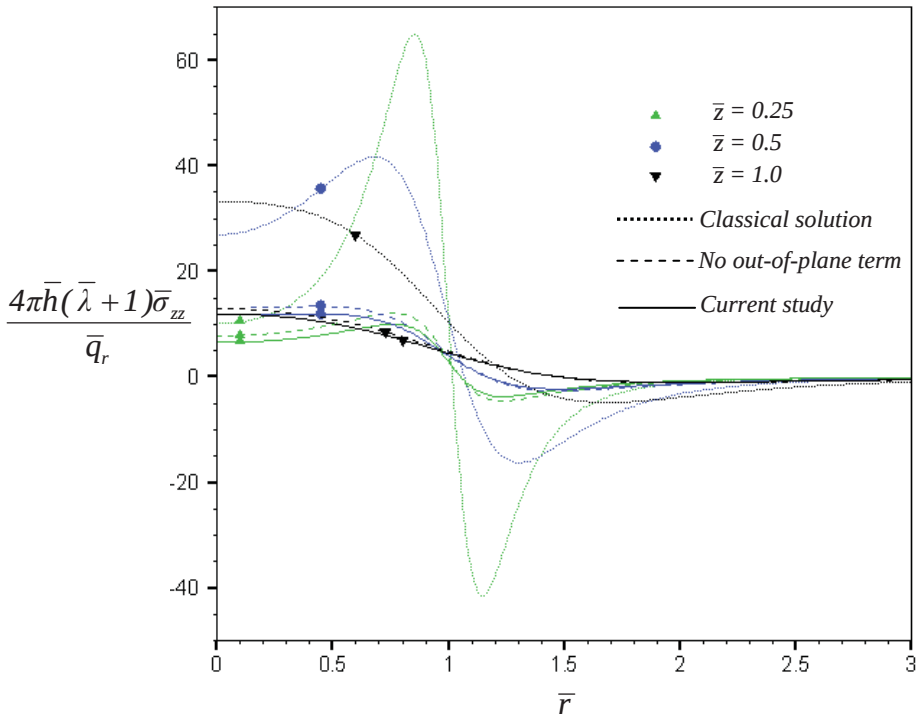

(a)

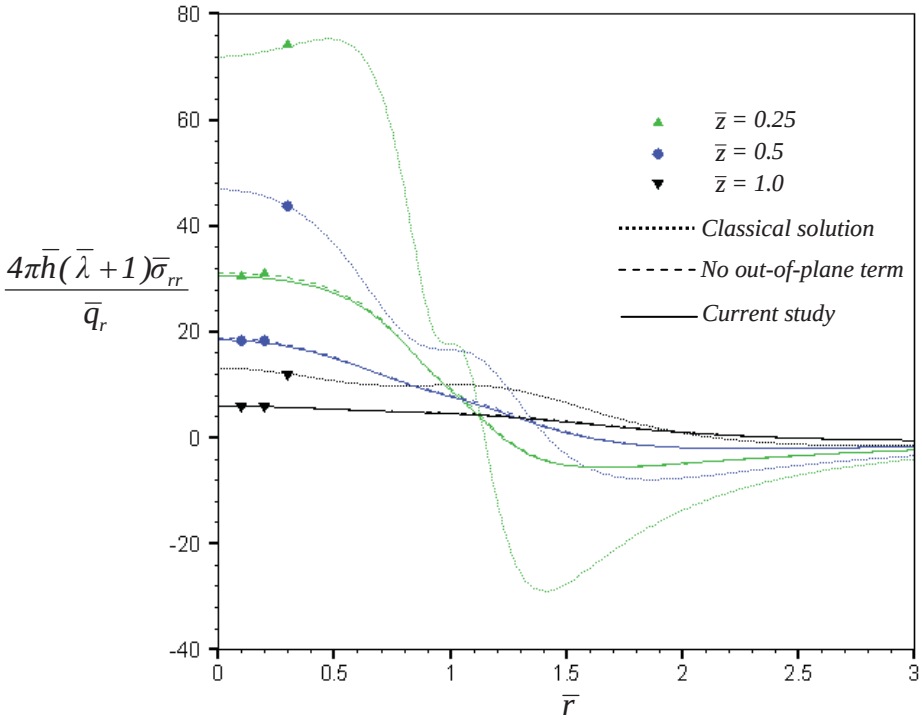

(b)

Figure 4.33 Normalized stress profiles of an elastic layer under tangential ring load: (a) vertical stress and (b) radial stress

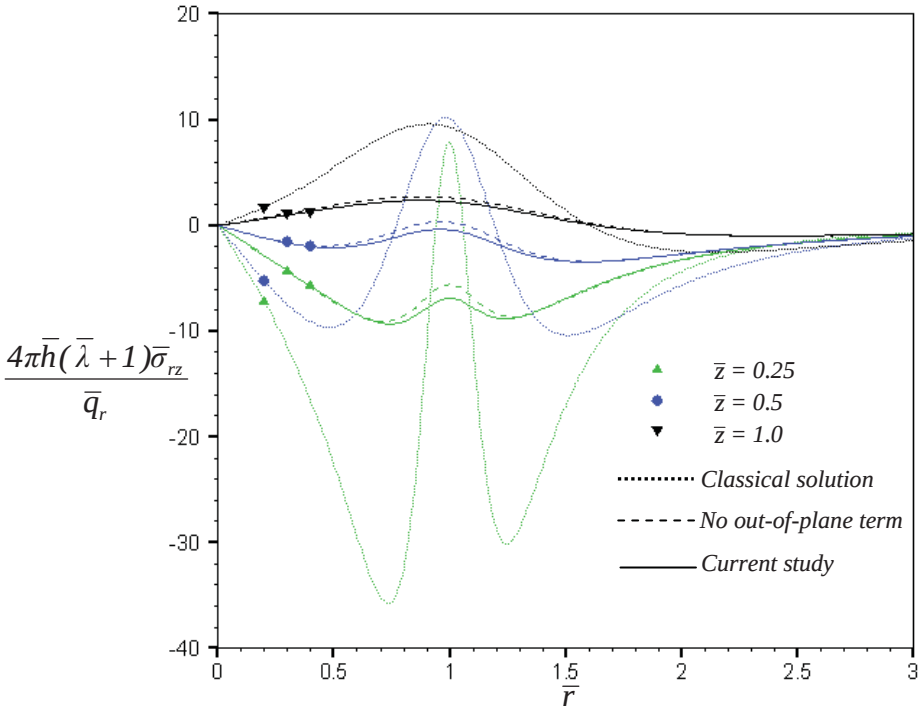

(a)

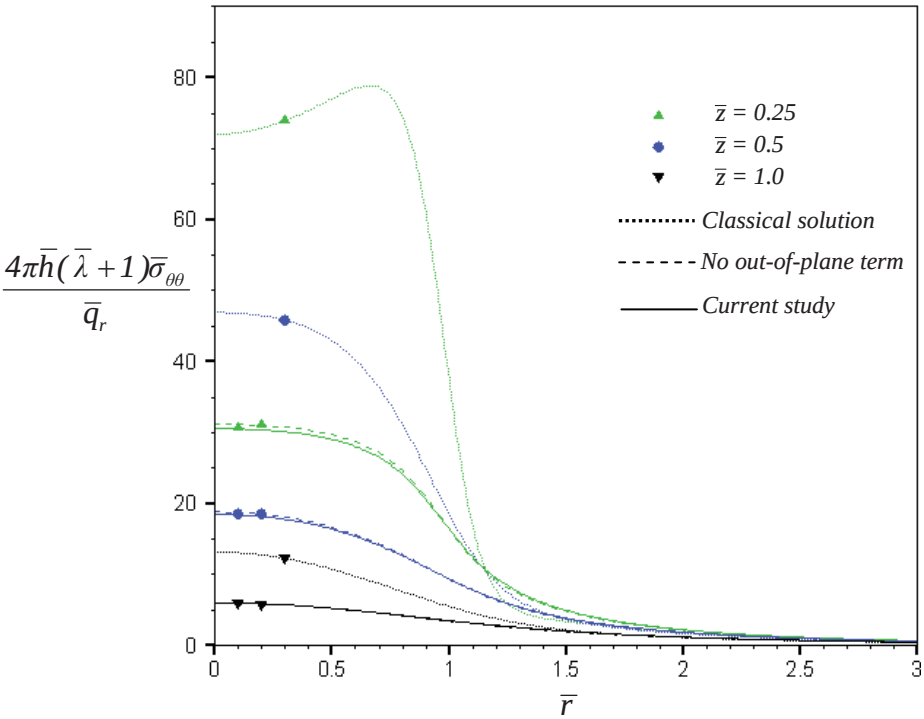

(b)

Figure 4.34 Normalized stress profiles of an elastic layer under tangential ring load: (a) shear stress and (b) hoop stress

CHAPTER V

CONCLUSIONS

SUMMARY

A complete analytical solution of a three-dimensional, infinite elastic layer under the action of axisymmetric normal and tangential surface loadings and with consideration of the surface energy effect has been derived. A novel feature of the present study is the use of a complete version of Gurtin-Murdoch constitutive relation to model the free surface of the layer. In solution procedure, Love's strain potential technique along with Hankel integral transform are applied to obtain the general solution for the bulk whereas the surface equations and conditions at the rigid base supply sufficient boundary conditions to determine all arbitrary constants. The displacement and stress fields within the bulk have been obtained via a selected efficient numerical quadrature. Once the obtained general solutions were verified by comparing with available benchmark solutions, extensive parametric study has been carried out to gain insight into the nano-scale influence and investigate the size dependency. Moreover, the three fundamental solutions corresponding to normal concentrated load, normal ring load, and tangential ring load which constitute the basis for solving nano-indentations problems have been constructed.

Results from extensive parametric studies have confirmed the significance of surface energy effects and the necessity to properly treat such influence in the continuum-based model. In the region close to the surface, the presence of the surface stresses exhibits very strong influence on both the displacement and stress fields. Magnitudes of field quantities obtained from models accounting for the surface energy effects are generally less than those obtained from the classical model. The presence of the surface energy renders the layer much stiffer than that of the classical case. This is due to that not the entire loadings that transfer directly into the bulk but part of them is carried by the surface through the equilibrium of the surface and the membrane-like action. Such influences also depend on the length scale of the

problem; the influence of surface stresses becomes significant when the length scale is comparable to the intrinsic length of the surface. Moreover, it is worth pointing out that such behavior of the out-of-plane responses due to the normal traction are more apparent in the model which integrates the out-of-plane contribution of the residual surface tension into the analysis. This additionally confirms the necessity to treat such crucial contribution in the modeling of soft elastic solids and nano-scale problems.

In addition, the surface radial and vertical displacements of a layer under either a normal ring load or a tangential ring load predicted by a model employed in the present study (i.e., a complete Gurtin-Murdoch surface elasticity model including the out-of-plane contribution of the residual surface tension) are finite everywhere. If the out-of-plane term is neglected, the predicted vertical displacement due to the normal ring load is still singular at the location where the load is applied. For the case of a normal concentrated load acting to the origin, the vertical displacement obtained from both classical model and model incorporating the surface stress effects is singular at the applied load location whereas only the radial displacement obtained from a model accounting for the out-of-plane term is finite.

SUGGESTIONS FOR FUTURE WORK

Due to the three fundamental solutions derived in the present study, frictionless indentation problems with arbitrary indentor profiles, axisymmetric frictionless indentation problems, axisymmetric indentation problems with the presence of friction, and axisymmetric, fully-bonded indentation problems can now be fully investigated. In addition, the formulation can further be generalized to treat following two cases: multiple layers under axisymmetric surface loading and a single layer under non-axisymmetric surface loading.

REFERENCES

Ahlvin, R.G. and Ulery, H. H., 1962. Tabulated values for determining the complete pattern of stresses, strains, and deflections beneath a uniform load on a homogeneous half space. Highway Research Board, Bulletin 342, 1-13

Barber, J. R., 1992. Elasticity. The Netherlands: Kluwer Academic Publisher.

Booker, R., and Boysen, E. 2005. Nanotechnology for dummies. New Jercy: Wiley.

Bumister, D.M., 1943. The theory of stresses and displacements in layered systems and applications to the design of airport runways. Proc.Highway Res.Board 23: 127-148.

Bumister, D.M., 1945. The general theory of stresses and displacements in layered soil systems. Applied Physics 16: 89-96, 126-127, 296-302.

Cammarata, R. C. 1994. Surface and interface stress effects in thin films. Progress in Surface Science 46: 1-38.

Cammarata, R. C. 1997. Surface and interface stress effects on interfacial and nanostructured materials. Materials Science and Engineering A 237: 180-184.

Dingreville, R., Qu, J., and Cherkaoui, M. 2005. Surface free energy and its effect on the elastic behavior of nano-sized particles, wires and films. Journal of the Mechanics and Physics of Solids 53: 1827-1854.

Fischer, F. D., Waitz, T., Vollath, D., and Simha, N. K. 2008. On the role of surface energy and surface stress in phase-transforming nanoparticles. Progress in Materials Science 53: 481-527.

Gibbs, J. W. 1906. The scientific papers of J. Willard Gibbs. Vol. 1. London: Longmans Green.

Gurtin, M.E. and Murdoch, A.I. 1975. A continuum theory of elastic material surfaces. Archive for Rational Mechanics and Analysis, 57: 291-323.

Gurtin, M.E. and Murdoch, A.I. 1978. Surface stress in solid. International Journal of Solids and Structures, 14: 431-440.

Gurtin, M.E., Weissmüller, J., and Larché, F. 1988. A general theory of curved deformable interfaces in solids at equilibrium. Philosophical Magazine A, 78: 1093-1109.

He, L.H., Lim, C.W., and Wu, B.S. 2004. A continuum model for size-dependent deformation of elastic films of nano-scale thickness. International Journal of Solids and Structures, 41: 847-857.

He, L. H., and Lim, C. W. 2006. Surface green function for a soft elastic half-space: Influence of surface stress. International Journal of Solids and Structures 43: 132–143.

Huang, G. Y., and Yu, S. W., 2007 Effect of surface elasticity on the interaction between steps. Journal of Applied Mechanics 74: 821.

Huang, D. W. 2008. Size-dependent response of ultra-thin films with surface effects. Internarional Journal of Solids and Structures, 45: 568-579

Intarit, P., Senjuntichai, T., and Rajapakse, R.K.N.D. 2010. Dislocations and internal loading in a semi-infinite elastic medium with surface stresses. Engineering Fracture Mechanics, 77: 3592-3603.

Intarit, P., Senjuntichai, T., Rungamornrat, J. and Rajapakse, R.K.N.D. 2011. Surface Elasticity and Residual Stress Effect on the Elastic Field of a Nanoscale Elastic Layer. Interaction and Multiscale Mechanics, An Int't Journal, 4: 85-105.

Mao, S. X., Zhao, M., and Wang, Z. L. 2003. Nanoscale mechanical behavior of individual semiconducting nanobelts. Applied Physics Letters 83: 993-995.

Miller, R.E., and Shenoy, V.B. 2000. Size-dependent elastic properties of nanosized structural elements. Nanotechnology, 11: 139-147.

Pinyochotiwong, Y., Rungamornrat, J., and Senjuntichai, T. 2010. Rigid frictionless indentation on half-space with surface stresses. Master's thesis, Faculty of engineering (Civil engineering). Chulalongkorn University.

Poncharal, P., Wang, Z. L., Ugarte, D., and de Heer, W. A. 1999. Electrostatic deflections and electromechanical resonances of carbon nanotubes. Science 283: 1513-1516.

Poulos, H.G. 1974. Elastic solutions for soil and rock mechanics. The United States of America: John Wiley.

Povstenko, Y.Z. 1993. Theoretical investigation of phenomena caused by heterogeneous surface tension in solids, J. Mech. Phys. Solids, 41: 1499-1514.

Sander, D. 2003. Surface stress: Implications and measurements. Current Opinion in Solid State and Materials Science 7: 51-57.

Selvadurai, A.P.S. 2000. Partial differential equations in mechanics 2. Germany: Springer.

Sharma, P., and Wheeler, L. T. 2007. Size-dependent elastic state of ellipsoidal nano-inclusions incorporating surface/interface tension. Journal of Applied Mechanics - Transactions of the ASME 74: 447-454.

Sharma, P., Ganti, S., and Bhate, N. 2003. Effect of surfaces on the size-dependent elastic state of nano-inhomogeneities. Applied Physics Letters 82: 535-537.

Sheddon, I.N. 1951. Fourier transform. New York: McGraw-Hill.

Shenoy, V. B. 2002. Size-dependent rigidities of nanosized torsional elements. International Journal of Solids and Structures 39: 4039–4052.

Shenoy, V. B. 2005. Atomistic calculations of elastic properties of metallic fcc crystal surfaces. Physical Review B 71: 094104.

Tian, L., and Rajapakse, R. K. N. D. 2007a. Analytical solution for size-dependent elastic field of a nanoscale circular inhomogeneity. Journal of Applied Mechanics - Transactions of the ASME 74: 568-574.

Tian, L., and Rajapakse, R. K. N. D. 2007b. Elastic field of an isotropic matrix with a nanoscale elliptical inhomogeneity. International Journal of Solids and Structures 44: 7988-8005.

Timoshenko, S. and Goodier, J. N. 1951. Theory of Elasticity. New York: McGraw-Hill.

Wang, G. F., and Feng, X. Q., 2007 Effect of surface stresses on a contact problem at nanoscale. Journal of Applied Physics 101: 013510.

Wang, W., Zeng, X., and Ding, J. 2010. Finite element modeling of two-dimensional nanoscale structures with surface effects. World Academy of Science, Engineering and Technology 72: 867-872.

Wong, E. W., Sheehan, P. E., and Lieber, C. M. 1997. Nanobeam mechanics: Elasticity, strength, and toughness of nanorods and nanotubes. Science 277: 1971-1975.

Yakobson, B. I. 2003. Nanomechanics. In W. A. Goddard; D. W. Brenner; S. E. Lyshevski; and G. J. Iafrate (eds.), Handbook of nanoscience, engineering, and technology, chapter 17. Florida: CRC Press.

Zhao, X.J. 2009. Surface loading and rigid indentation of an elastic layer with surface energy effects. Master's thesis, Faculty of graduate studies (mechanical engineering). The University of British Columbia (Vancouver).

Zhao, X.J., Rajapakse, R.K.N.D. 2009. Analytical solutions for a surface-loaded isotropic elastic layer with surface energy effects. International Journal of Engineering Science, 47: 1433-1444.

BIOGRAPHY

The author, Miss Porjan Tuttipongsawat, was born on 14 July 1986. She started her class for Bachelor's Degree in Industrial Engineering at Faculty of Engineering, Chulalongkorn University in 2005. Due to her interest in structure, after graduation she decided to study for a second bachelor's degree in Civil engineering for two year. Moreover, she continued her Master's degree in Structural Civil Engineering at Chulalongkorn University in the same year under the supervision of Assistant Professor Dr. Jaroon Rungamornrat and Professor Dr. Teerapong Senjuntichai. During this period, she obtained more advanced knowledge of structural engineering and decided to do her research on solid mechanics.